Fuel 428 (2027) 140372

Contents lists available at ScienceDirect

Fuel

journal homepage: www.elsevier.com/locate/fuel

Full Length Article

LNG/H_2-rich syngas centric quad-generation plant with hydrogen-ready self-sustaining feeder; economic evaluation, Cuckoo search, and MLP neural networks

Yonghui Li [a], Ali Basem [b], Hyder H. Abed Balla [c,*], Mohamed Arbi Khlifi [d,*], Haibo Zhang [a,*], Saleh Alhumaid [e], Nasser Alsharif [f], Sherzod Abdullaev [g], Yasser Fouad [h,*], Ibrahim Mahariq [i,j,k,**]

[a] School of Digital Economy and Management, Sichuan University of Technology and Business, Meishan, Sichuan 620000, China
[b] Advanced Technical College, University of Warith Al-Anbiyaa, Karbala, Iraq
[c] Aeronautical Technical Department, Najaf Technical Institute, Al Furat Al Awsat Technical University, Najaf, Kufa, Iraq
[d] Department of Electrical Engineering, Faculty of Engineering, Islamic University of Madinah, Madinah 42351, Saudi Arabia
[e] Department of Mechanical Engineering, University of Hail, Hail 81481, Saudi Arabia
[f] Department of Sciences and Technology, Ranyah University Collage, Taif University, Taif 21944, Saudi Arabia
[g] School of Exact Sciences, National Pedagogical University of Uzbekistan, Tashkent, Uzbekistan
[h] Department of Applied Mechanical Engineering, College of Applied Engineering, Muzahimiyah Branch, King Saud University, Saudi Arabia
[i] Department of Electrical and Electronic Engineering, Faculty of Engineering and Architecture, Istanbul Gelisim University, Avcılar- Istanbul 34310 Istanbul, Turkey
[j] Department of Medical Research, China Medical University Hospital, China Medical University, Taichung, Taiwan
[k] University College, Korea University, Seoul 02481, South Korea

ARTICLE INFO

Keywords:
Hydrogen-rich syngas
Liquefied natural gas
Low-carbon hydrogen generation
Steam methane reforming
Exergo-enviro-economic analysis
Machine learning-based optimization

ABSTRACT

The rising global demand for sustainable energy, coupled with the urgent need for low-carbon hydrogen production, presents a significant challenge for modern energy systems. Existing multi-generation frameworks often suffer from inefficient thermal resource utilization and high computational costs during optimization. To address these gaps, this study proposes a novel, thermodynamically integrated liquefied natural gas (LNG)-based quad-generation system that synergistically combines LNG cold energy recovery with steam methane reforming, gas turbine power, steam Rankine and Kalina cycles, and a proton exchange membrane electrolyzer. To ensure high-efficiency performance, a surrogate-aided optimization plan, utilizing a Multi-Layer Perceptron model tuned with Cuckoo Search algorithm, is developed to navigate the complex decision space. Simulation results demonstrate that the optimized system achieves a remarkable exergy efficiency of 56.50% and a primary energy saving ratio of 34.43%, while maintaining competitive specific CO_2 emissions of 0.297 kg_{CO2}/kWh. Economically, the optimal configuration yields a total unit cost of product of 10.84 $/GJ and an annual profit of 31.01 M $, with a dynamic payback period (DPP) of 3.34 years. Comprehensive sensitivity and uncertainty analyses revealed that LNG flow rate and gas turbine outlet pressure are the primary drivers of overall system performance. These findings indicate that the proposed framework offers a robust, technically feasible, and economically viable solution for industrial-scale quad-generation, providing a scalable pathway for enhancing resource efficiency and promoting sustainable hydrogen production in future energy infrastructures.

* Corresponding authors at: Aeronautical Technical Department, Najaf Technical Institute, Al Furat Al Awsat Technical University, Najaf, Kufa, Iraq (H.H. Abed Balla), Department of Electrical Engineering, Faculty of Engineering, Islamic University of Madinah, Madinah 42351, Saudi Arabia (M.A. Khlifi), School of Digital Economy and Management, Sichuan University of Technology and Business, Meishan, Sichuan 620000, China (H. Zhang), Department of Applied Mechanical Engineering, College of Applied Engineering, Muzahimiyah Branch, King Saud University, P.O. Box 800, Riyadh 11421, Saudi Arabia (Y. Fouad).
** Corresponding author at: Department of Medical Research, China Medical University Hospital, China Medical University, Taichung, Taiwan.
E-mail addresses: hyderballa@atu.edu.iq (H.H. Abed Balla), SCI868@126.com (M.A. Khlifi), medarbi@iu.edu.sa (H. Zhang), yfouad@ksu.edu.sa (Y. Fouad), ibmahariq@gmail.com (I. Mahariq).

https://doi.org/10.1016/j.fuel.2026.140372
Received 6 April 2026; Received in revised form 10 June 2026; Accepted 13 June 2026
Available online 24 June 2026

Nomenclature

$\dot{C}_F$	LNG fuel cost rate
CO	Carbon monoxide
CO_2	Carbon dioxide
$\dot{Ex}_{CH}$	Chemical exergy
$\dot{Ex}_D$	Destroyed exergy
$\dot{Ex}_F$	Fuel exergy
$\dot{Ex}_P$	Product exergy
$\dot{Ex}_{PH}$	Physical exergy
$\dot{E}_{D,i}$	Component i-th destroyed exergy
h	Enthalpy
H_2	Hydrogen
$\dot{m}$	Mass flow rate
$\dot{m}_{CO_2}$	Total CO_2 emission rate
n	System lifetime
P_{ele}	Electrical power price
$P_{heating}$	Heating price
$P_{cooling}$	Cooling price
P_{H2}	Hydrogen price
$\dot{Q}$	Transferred heat rate
q	Interest rate
$\dot{Q}_{heating}$	Heating energy
$\dot{Q}_{cooling}$	Cooling energy
$\dot{Q}_{H2}$	Hydrogen energy
$\dot{Q}_F$	Fuel energy
R	Gas factor
R^2	Coefficient of determination
s	Entropy
t_y	Annual working hours of the system
$\dot{W}$	Generated net power rate (rate of work)
$\dot{W}_{net}^{MG}$	Power output of the system
Z_i	Equipment cost
$\dot{Z}_i^{CI}$	Capital investment cost for i-th component
$\dot{Z}_i^{OM}$	Operation and maintenance cost for i-th component
β_i	Component i-th exergy destruction rate
ψ_i	Component i-th exergy efficiency
$\eta_{MG, ELE}$	Electrical efficiency of the system
η_{MG}	Energy efficiency of the system
ψ_{MG}	Exergy efficiency of the system
ω_{CO_2}	Specific CO_2 emission

Abbreviation

AI	Annual Income
AS	Annual Saving
CAPEX	Capital Expenditure
CCHP	Combined Cooling, Heating, and Power system
CRF	Capital Recovery Factor
DPP	Dynamic Payback Period
EII	Exergo-environmental Impact Improvement
FC	Fixed Cost
FCI	Fixed Capital Investment
GWP	Global Warming Potential
IRR	Internal Return Rate
LCOE	Levelized Cost of Energy
LCA	Life cycle assessment
LNG	Liquefied Natural Gas
MAPE	Mean Absolute Percentage Error
MAE	Mean Absolute Error
MG	Multi-Generation
MLP	Multi-Layer Perceptron
OPEX	Operating Expenses
PESR	Primary Energy Saving Ratio
PEME	Proton Exchange Membrane Electrolyzer
RMSE	Root Mean Square Error
SI	Sustainability Index
SMR	Steam Methane Reforming
TAC	Total Annual Cost
TCR	Total Cost Rate
TCI	Total Capital Investment
TUCP	Total Unit Cost of Product
4E	Energy, Exergy, Economic, and Environmental

1. Introduction

1.1. Background and motivation

Multi-generation (MG) systems improve overall fuel utilization by producing multiple outputs such as electricity, heating, cooling, and chemical energy carriers, from a single energy source. Compared to conventional single-output plants, MG systems reduce exergy destruction and improve resource utilization [1,2]. In the last decades, liquefied natural gas (LNG) is increasingly deployed as a transitional fuel due to lower carbon intensity compared to coal and oil as well as multifaceted and high-loading energy fuel source [3,4]. In the light of global increase of LNG trade volume [5], there is an urgent requirement to minimize the use of fuel, and reduce the emission of greenhouse gases along the LNG supply chain [6,7]. During regasification of LNG at a temperature of −162 °C, it is converted from its ultra-cold liquid state back into natural gas giving off significant cold energy [8]. Efficient recovery of this cold energy can significantly enhance system-level performance. That is, it can be ideally used in producing chilled water and supporting cooling processes in MG plants [9]. On the other hand, the generated natural gas through various technologies can be used in different units of MG plants to generate electricity and useful heating [10,11].

In addition, hydrogen (H_2) is emerging as an energy carrier. However, hydrogen produced from natural gas via steam methane reforming (SMR) is categorized as fossil-based or transitional low-carbon hydrogen depending on system efficiency and emissions. The steam reforming of natural gas is a common industrial process of converting natural gas into syngas, which principally comprises H_2 and carbon monoxide (CO). During this reaction, the high temperature steam, usually between 700 and 1100 °C, reacts with natural gas under the influences of a nickel-based catalyst. The main reaction is the methane steam reforming, which converts methane and steam into hydrogen and carbon monoxide, while a water–gas shift reaction, adds even more hydrogen to what is already produced. Integrating an SMR into MG energy systems enables more efficient utilization of fuel by simultaneously producing multiple energy products. For instance, when an SMR is integrated with fuel cells [12] or gas turbines [13], the thermal and chemical energy produced throughout the reforming procedure could be effectively used for power generation. Similarly, coupling SMR with organic Rankine cycles [14] or absorption cooling systems [15] enables additional recovery of waste heat for electricity and cooling production, respectively. In systems that utilize SMR in conjunction with fuel cells, the hydrogen-rich syngas produced is well-suited for direct use in the fuel cell, enabling the simultaneous production of electricity and heat, leading to improved overall exergy efficiency [16]. Moreover, the high-grade heat from an SMR unit can be utilized to drive organic Rankine cycles for electricity generation or absorption chillers for cooling production, which can enable a highly coupled MG system [17]. The integration of an SMR into

Table 1
Comparison of recent steam–reforming–based MG systems with the present study.

Study	Energy Source	Configuration	Optimization Method	Performance Indicators	Key Features	Limitations
Yan et al. [20]	Natural gas	SE–SMR + Ca–looping carbon capture + H_2 gas turbine + absorption chiller	Parametric analysis	Energy efficiency, exergy efficiency, carbon capture rate	Low–carbon CCHP system with CO_2 capture	No LNG cold energy recovery; limited optimization
Hu et al. [21]	Methanol	Methanol steam reformer supplying SOFC	Experimental + simulation	Methanol conversion, reformer performance	Detailed reformer design and experimental validation	Reactor–level study; no MG integration
Su et al. [22]	Methanol	MSR + scramjet cooling cycle + ammonia synthesis + desalination	Parametric study	Energy, exergy, environmental, economic indicators	Complex multi–product generation system	No LNG integration; no advanced optimization
Chen et al. [23]	Methanol	MSR + HT–PEM fuel cell	Numerical simulation	Output power, system efficiency	Thermal self–sustained reformer–fuel cell integration	Limited to electricity generation
Abed et al. [24]	Natural gas / methanol	Gas turbine + MSR + CO_2 recondensation + desalination + absorption chiller	Energy/exergy/exergo-economic analysis	Energy efficiency, exergy efficiency, cost, emissions	Multi–product system including hydrogen and freshwater	No machine–learning optimization
Dai & Yin [25]	Natural gas	Gas turbine + SMR thermochemical recuperator + cooling + desalination	MOPSO–LINMAP	Energy efficiency, economic indicators	Multi–objective optimization of MG system	No LNG cold energy recovery
Soltanimehr et al. [26]	Natural gas	Pre–reformer + tri–reformer reactor for syngas production	Multi–objective optimization (CHEMKIN + MATLAB)	CH_4 conversion, H_2 yield, CO_2 emissions	Advanced reforming reactor design	Reactor–level focus; not MG
Zhong et al. [27]	Methanol	RM–HT–PEM fuel cell + absorption refrigeration (CCHP)	NSGA–II + TOPSIS	Exergy efficiency, CO_2 emissions, cost	Fuel–cell–driven CCHP optimization	No hydrogen production output
He et al. [28]	Biogas	Biogas steam reforming + purification + MG system	Multi–objective optimization	Energy, exergy, exergo-economic performance	Renewable feedstock utilization	Small scale system; no LNG integration
Present Study	LNG (methane)	LNG regasification + SMR + gas turbine + steam Rankine cycle + Kalina cycle + hot water boiler + PEM electrolyzer	Hybrid Multi-Layer Perceptron (MLP) surrogate model + Cuckoo Search multi–objective optimization	4E analysis	Integrated LNG cold energy recovery, moderate temperature reforming strategy, and surrogate assisted multi objective optimization for quad-generation (electricity, heating, cooling, hydrogen)	Low–carbon hydrogen produced via fossil–based SMR; upstream LNG emissions not included in boundary

energy systems, besides resulting in lower net greenhouse-gas emissions through improved thermal management, also contributes to the transformation toward sustainable energy systems by facilitating hydrogen production, which serves as a major vector of low-carbon energy solutions [18,19].

1.2. Literature Review

Recent studies have explored the integration of steam reforming processes with MG energy systems to enhance fuel utilization and enable hydrogen production alongside power, heating, and cooling. However, most existing studies remain limited either in system integration scope, optimization methodology, or boundary definition.

Yan et al. [20] proposed a low–carbon CCHP (combined cooling, heating, and power) system integrating sorption–enhanced (SE) SMR with a calcium (Ca) looping carbon capture process. Their configuration included an absorption chiller and a H_2-based gas turbine, achieving high energy and exergy efficiencies, with carbon capture rates up to 96%. Although this work demonstrates the potential of integrating reforming with carbon capture for low–carbon energy production, the study focuses primarily on tri–generation (namely power, heat, cooling) rather than broader MG frameworks and does not consider LNG cold energy recovery or system–level optimization strategies.

Hu et al. [21] experimentally investigated a methanol steam reforming reactor designed to supply hydrogen for kW–scale fuel cells. Their work provides valuable insights into reformer design parameters such as steam–to–carbon ratio, heating temperature, and liquid hourly space velocity. However, the study is primarily reactor–level and experimental, focusing on methanol conversion and reformer performance rather than integrated energy systems. As a result, system–level thermodynamic integration and MG performance evaluation are not addressed.

Su et al. [22] proposed a complex MG plant integrating methanol steam reforming with a scramjet multi–cooling cycle, ammonia synthesis, and desalination. The system was analyzed using 4E (energy, exergy, economic, and environmental) indicators. While the work demonstrates a comprehensive multi–product energy system, its configuration is highly specialized and does not involve LNG cold energy recovery or natural gas–based reforming. Additionally, optimization is mainly based on parametric investigations rather than advanced machine learning or surrogate–based optimization methods.

Chen et al. [23] developed a numerical model integrating methanol steam reforming with high–temperature proton exchange membrane fuel cells (HT–PEMFC). Their work emphasizes the thermal self–sufficiency of the integrated reformer–fuel cell system and investigates operating parameters such as the steam–to–carbon ratio and reformer temperature. Although the study provides valuable insights into fuel cell integration, it focuses primarily on power generation systems rather than broader MG frameworks and does not consider waste heat recovery or hydrogen utilization beyond the fuel cell.

Abed et al. [24] investigated an MG system based on a gas turbine combined with methanol steam reforming, a CO_2 (carbon dioxide) recondensation cycle, desalination, and absorption cooling. Their exergo-economic analysis demonstrated great energy and exergy efficiencies. While the system integrates multiple outputs including hydrogen, cooling, and freshwater, the study relies mainly on

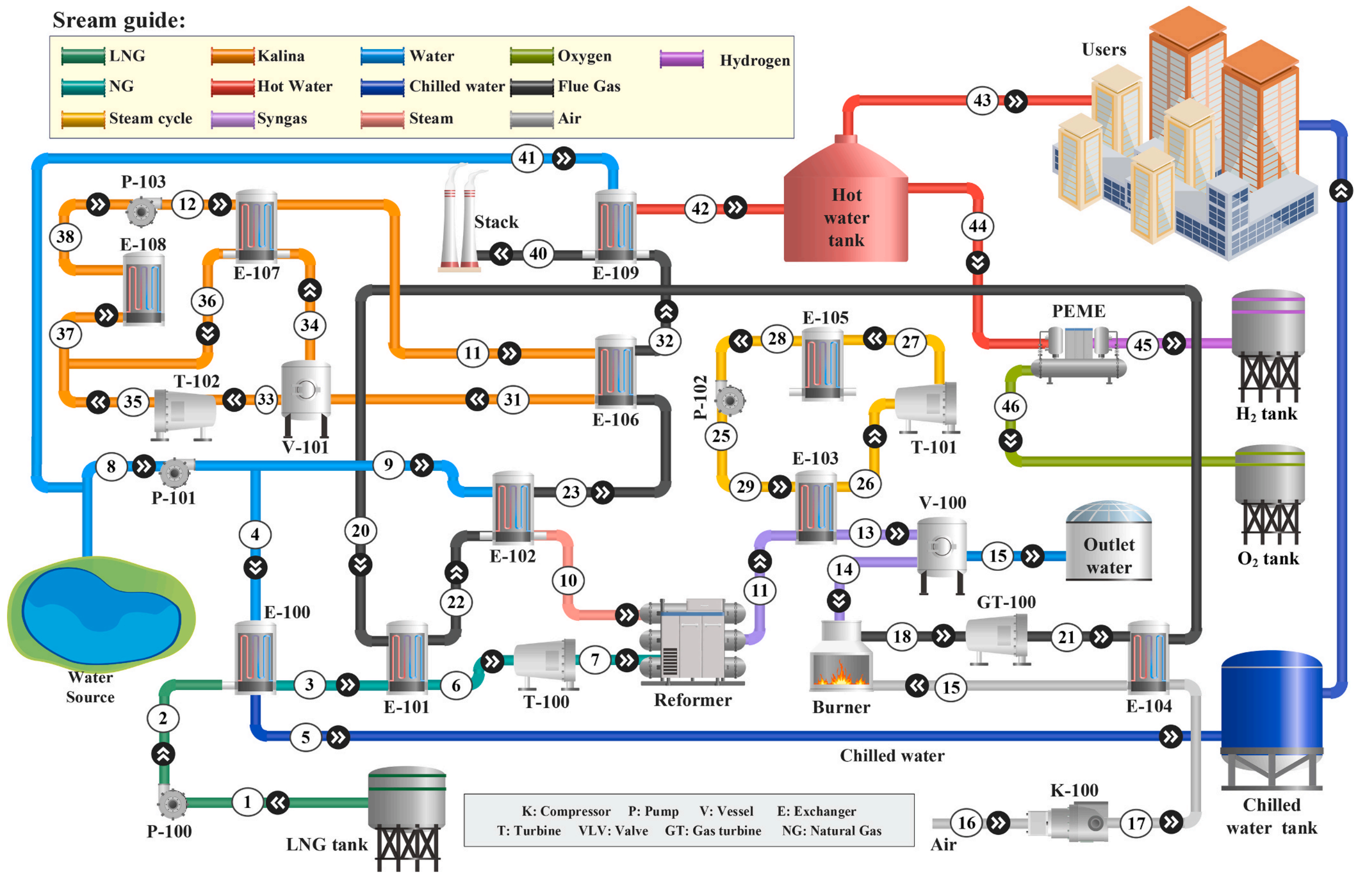

Fig. 1. Detailed process of the newly presented quad–generation energy system that can produce H_2, electricity, cold water, and hot water simultaneously.

conventional thermodynamic and exergo-economic analyses and does not incorporate advanced optimization techniques or machine learning–assisted design strategies.

Dai and Yin [25] proposed a gas–turbine–driven MG system incorporating SMR as a thermochemical recuperator, producing power, hydrogen, cooling, and freshwater. Their work includes multi–objective optimization using the MOPSO–LINMAP algorithm and demonstrates improvements in system efficiency and payback period. Despite these contributions, the system does not exploit LNG cold energy and the optimization approach relies solely on evolutionary algorithms without surrogate modeling to reduce computational cost.

Soltanimehr et al. [26] introduced a novel tri–reforming reactor configuration aimed at improving syngas production for methanol synthesis. Their work integrates CHEMKIN–based combustion modeling with MATLAB optimization to maximize methane conversion and hydrogen yield while minimizing CO_2 emissions. Although this study contributes to reforming reactor design and optimization, it remains process–level rather than system–level, and does not investigate integration with MG energy systems.

Zhong et al. [27] studied a CCHP system based on reformed methanol HT–PEM fuel cells integrated with a cycle of absorption refrigeration. An advanced optimization employing NSGA–II was implemented to simultaneously improve exergy efficiency and reduce CO_2 emissions. While the work demonstrates effective system optimization, it focuses on fuel–cell–driven CCHP systems and does not address broader MG outputs such as hydrogen production or LNG cold energy recovery.

He et al. [28] proposed a biogas–based MG system incorporating steam reforming and hydrogen purification, evaluated using energy, exergy, and exergo-economic analyses. Multi–objective optimization was applied to improve system performance. Although the use of renewable biogas represents an environmentally attractive pathway, the system scale and energy output remain relatively limited, and the study does not consider LNG–based systems or advanced surrogate–assisted optimization techniques.

On the whole, the reviewed related works demonstrate significant progress in integrating steam reforming processes with energy systems for hydrogen production and MG applications. To better position the present work within existing research, Table 1 compares recent steam–reforming–based MG systems reported in the literature with the proposed configuration. The comparison underlines differences in sources of energy, configurations of system, optimizing approaches, and evaluation metrics.

1.3. Research gaps, novelty, and contributions

Although previous studies have demonstrated the potential of steam reforming-based MG systems for improving fuel utilization and enabling hydrogen output, several limitations persist in the existing literature. As summarized in Table 1, most investigations focus on methanol or biogas steam reforming systems, while relatively few studies examine the integration of SMR with LNG regasification processes. Furthermore, many works concentrate on reformer performance or subsystem–level integration, whereas the system–level coupling of LNG cold energy recovery with hydrogen–yielding reforming processes in quad–generation frameworks has received limited attention. In addition, the majority of optimization studies rely on conventional evolutionary algorithms such as genetic algorithms, NSGA–II, or particle swarm optimization, and the use of surrogate–assisted optimization approaches to reduce computational cost in complex thermodynamic models remains rare. Another limitation concerns the inconsistency in the definition of system boundaries and evaluation metrics in 4E analyses, which complicates the comparison of different system configurations. Moreover, many existing studies primarily aim to maximize hydrogen yield or component performance without sufficiently examining system–level trade–offs between hydrogen production, power generation, and overall efficiency.

In order to overcome these limitations, the current project suggests a thermodynamically integrated LNG–based quad–generation system that combines LNG cold energy recovery with SMR to simultaneously produce electricity, heating, cooling, and hydrogen. The proposed configuration uniquely integrates LNG regasification, SMR, a gas turbine, a steam Rankine cycle, a Kalina cycle, a hot water boiler, and a proton exchange membrane electrolyzer (PEME) to enhance overall energy utilization through effective recovery and cascading use of thermal and cold energy streams. This integrated design aims to improve system efficiency while enabling lower–carbon hydrogen production through enhanced thermodynamic coupling. In addition, a surrogate–assisted multi–objective optimization framework based on a Multi-Layer Perceptron (MLP) model coupled with the Cuckoo Search algorithm is developed to accelerate the optimization of the complex thermodynamic model. Finally, clearly defined system boundaries are adopted for the 4E analyses, enabling a transparent and comprehensive evaluation of system performance and facilitating comparison with previously reported MG configurations. Thus, the main contributions of this study are summarized as follows:

- Development of a thermodynamically integrated LNG–SMR quad–generation system that operates under moderate reformer temperatures to enhance fuel utilization and enable low–carbon hydrogen production.
- Clear and explicit definition of system boundaries for the 4E analyses, providing transparency and consistency in performance evaluation.
- Detailed parametric investigations illustrating the sensitivity of system behavior to critical design and operating variables.
- Comprehensive feature–importance analysis identifying key operational parameters influencing major performance indicators.
- Implementation of a surrogate–aided multi–objective optimization plan combining an MLP model with an algorithm of Cuckoo Search for efficiently exploring the performance trade–offs.
- Quantitative benchmarking against prior literature, demonstrating the advantages of the proposed configuration in energy utilization, exergy recovery, overall environmental and economic performance.

2. System description

Fig. 1 showcases a detailed process of a novel natural gas-centered quad–generation system that can generate H_2, electricity, cold water, and hot water simultaneously. This process integrates the SMR unit, steam Rankine cycle, gas turbine system, Kalina cycle, water boiler and electrolyzer for efficient heat recovery during the system.

- **Steam reforming process**.

The process begins with the LNG fuel entering (stream 1), which is initially pressurized by the P-100 pump. The suggested system utilizes the low-temperature properties of LNG by passing it through the E-100 to creates a chilled water. As LNG exits the E-100 exchanger, it undergoes a phase change and transitions into natural gas. This high-pressure natural gas is further heated in the E-101 heat exchanger to raise its enthalpy before expansion. The pressurized and heated gas moves through turbine T-100 for expansion to convert its thermal energy into mechanical work and electricity. After expansion, the natural gas exhaust, which still has considerable heat energy, gets into the unit of the reformer. The reforming reactions need steam, which is generated by pressurizing feedwater with the P-101 pump and transferring such pressurized water into the E-102, this required steam is generated. Within the reformer, the three endothermic reactions take place which are SMR reaction (Eq. (1)), the water–gas shift reaction (Eq. (2)), and the combined methane reforming reaction (Eq. (3)) as below:

$$CH_4 + H_2O \leftrightarrow CO + 3H_2 \quad (1)$$

$$CO + H_2O \leftrightarrow CO_2 + H_2 \quad (2)$$

$$CH_4 + 2H_2O \leftrightarrow CO_2 + 4H_2 \quad (3)$$

The combined reactions produce a hot synthesis gas, syngas, which is enriched with hydrogen as a key input for other downstream power and hydrogen production processes.

- **Steam Rankine process**.

The reformer's hot syngas (stream 11) enters the heat exchanger E-103, which is the heat source for a steam Rankine cycle subsystem. In this subsystem, steam supplied by the high-pressure P-102 pump absorbs energy from the syngas, vaporizing into depressing high pressure saturated steam. This steam undergoes expansion in the turbine T-101, converting thermal energy into additional energy in the form of electricity, thereby improving total energy efficiency of the overall system. After expansion, the steam is condensed in the E-105 condenser, and the condensed steam is returned back to P-102. The syngas leaving E-103 is in a two-phase state due to the extraction of heat and the conditions of operation, thus requiring phase separation in the V-100 separator. In V-100, water, which destroys the calorific value of the syngas is removed from the syngas and the hydrogen-rich syngas is sent directly to the gas turbine cycle for power generation.

- **Gas turbine system**.

The hydrogen-rich syngas (stream 14) enters to the gas turbine burner, where is combined with the compressed air by K-100 compressor. This compressed air is preheated in the E-104 heat exchanger for efficient combustion process. The combusted gases are expanded through the GT-100 turbine to produce valuable electric power. However, the flue gas from the turbine has valuable thermal value, that heat recovery processes is designed to capitalize on the usable thermal heat. Specifically, the flue gas passes through the E-104 heat exchanger for preheating combustion air and then is further used for adding heat to the reforming process in which is used in E-101 for preheating natural gas and E-102 for generating steam.

- **Kalina process**.

This flue gas with elevated temperatures, passes through the vapor generator E-106 of the Kalina cycle (stream 23) to vaporize the Kalina cycle working fluid. The Kalina cycle uses a mix of water and ammonia as a working fluid. The vaporization process provides vapor–liquid mixture, which is separated in V-101 and the vapor is expanded in turbine T-102 to produce more mechanical and electrical power. The hot liquid exits the separator and transfers residual heat via the economizer E-107 to the Kalina working fluid and then merge with the turbine exhaust. The combined operating fluid is compressed in E-108 at a constant pressure and is then pumped to a higher pressure with pump P-103. This high-pressure working fluid is routed through the economizer to recover heat and then returned to E-106 to complete the Kalina cycle.

- **Water boiler and electrolysis process**.

The passed flue gas through the vapor generator E-106 is directed into the hot water boiler E-109 (stream 32) to produce hot water for domestic utilization and hydrogen generation. The cooled flue gas is discharged to the atmosphere after conducting all heat recovery. The hot water for hydrogen generation goes to the PEME (stream 44) which uses it as feedwater for electrolysis process, in which the separation is occurred for producing hydrogen with suitable purity.

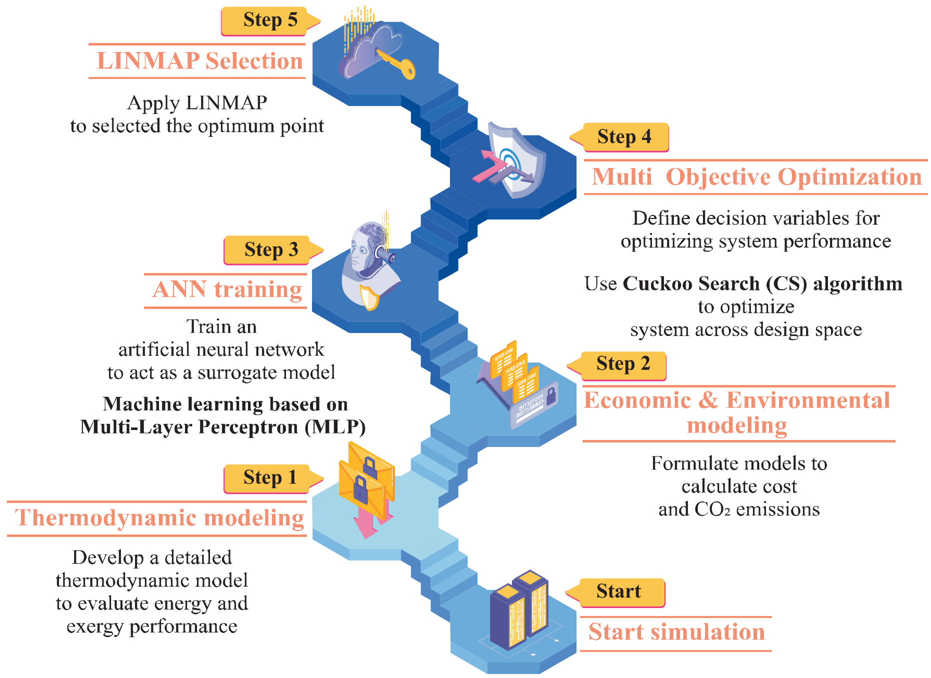

Fig. 2. The multi-stage approach of the proposed quad–generation system design.

Table 2
The design and operation data of components [29,35].

Parameter	Value
Dead state temperature (°C)	25
LNG rate (kg/s)	0.5
Air to burner (kg/s)	14
GT-100 outlet pressure (kPa)	106
Dead state pressure (kPa)	101.3
K-100 outlet pressure (kPa)	600
P-100 outlet pressure (kPa)	3000
T-102 outlet pressure (kPa)	600
T-102 inlet pressure (kPa)	3000
T-101 outlet pressure (kPa)	4
T-101 inlet pressure (kPa)	4000
PEME temperature (°C)	80
PEME pressure (kPa)	101.3
Stream 6 temperature (°C)	800
Stream 36 temperature (°C)	45
Stream 10 temperature (°C)	800
Stream 19 temperature (°C)	700
Stream 13 temperature (°C)	30
Stream 28 temperature (°C)	26
Stream 31 temperature (°C)	170
Stream 3 temperature (°C)	5
Hot water temperature (°C)	80
Chilled water temperature (°C)	6

3. Methodology and materials

This study adopts a multi-stage approach for the design [29] and evaluation of a novel quad–generation system capable of generating power, heating, cooling, and hydrogen at the same time. The overall design procedure is illustrated as a flowchart in Fig. 2. The process starts with the simulation stage, in which the specifications of system components and the required input data are defined to simulate the integrated system. Following the simulation, a comprehensive 4E assessment is performed, including energy, exergy, environmental, and economic analyses. Subsequently, a detailed parametric study is carried out to investigate the influence of key operating parameters on system performance under different conditions. Lastly, the research undertakes a multi-dimensional optimization analysis to determine the optimal operating parameters of the system that achieve an appropriate balance between technical performance, economic viability, and environmental impact [30,31].

3.1. System simulation

The simulation of the proposed quad–generation system is carried out using Aspen HYSYS, which provides a robust platform for modeling complex process interactions. To accurately represent the thermodynamic behavior of the involved subsystems under varying operational conditions, the Peng-Robinson equations of state are selected [32], which are described in the form of the relationships shown below [33,34]:

$$P = \left(RT \times [v-b]^{-1}\right) - [a/[v-(v+b)+b(v-b)]] \tag{4}$$

$$a = 0.45724 \frac{R^2 T_c^2}{p_c} \alpha \tag{5}$$

$$b = 0.07780 \frac{RT_c}{P_c} \tag{6}$$

where P and T refers to the pressure and the temperature of fluid. The parameter v is molar volume of the mixture, the constant of a and b are Peng-Robinson property package, and R is a gas factor.

The design and operation data of the components simulated in this process are listed in Table 2 and the thermophysical properties results directing the system and mass balance for key points of the current system are presented in Tables 3 and 4, correspondingly:

Additionally, the following assumptions are taken into account in developing subsystems and components:

- The composition of the LNG stream includes pure methane [7].
- Entire system operates under steady state environments [7].
- Kalina cycle operates using a mixture of ammonia and water as a working fluid [7].
- PEME accomplishes hydrogen generation [7].
- Pressure losses for pipelines and equipment are assumed negligible [36].

Table 3
Thermophysical properties results for each stream of the proposed trigeneration system.

Stream	T(°C)	P (kPa)	$\dot{m}\left(\frac{kg}{s}\right)$	Mass Enthalpy (kJ/kg)	Mass Entropy (kJ/kg. °C)
1	−161.60	101.3	0.500	−5579	4.762
2	−159.40	4000	0.500	−5567	4.799
3	5.00	4000	0.500	−4765	9.251
4	25.00	101.3	4.892	−15890	2.981
5	6.00	101.3	4.892	−15970	2.697
6	800	4000	0.500	−1942	13.690
7	607.10	600	0.500	−2798	13.800
8	25.00	101.3	2.000	−15890	2.981
9	25.04	600	2.000	−15890	2.981
10	880.00	600	2.000	−11620	11.600
11	522.30	600	2.500	−9855	12.440
12	38.61	3000	5.275	−9651	4.104
13	30.00	600	2.500	−12650	5.993
14	30.00	600	0.838	−6281	11.820
15	30.00	600	1.661	−15860	3.053
16	25.00	101.3	14.00	−0.283	5.258
17	238.60	600	14.00	220.3	5.302
18	1907.00	600	14.84	332.6	7.746
19	700.00	600	14.00	728.9	6.008
20	959.90	106	14.84	−1007	7.466
21	1315.00	106	14.84	−527	7.808
22	887.50	106	14.84	−1102	7.387
23	430.10	106	14.84	−1677	6.759
25	26.37	4000	2.507	−15880	2.998
26	251.30	4000	2.507	−13100	8.885
27	29.25	4.00	2.507	−14000	9.218
28	26.00	4.00	2.507	−15880	2.996
29	26.37	4000	2.507	−15880	2.998
30	93.95	3000	5.275	−9390	4.875
31	170.00	3000	5.275	−8324	7.487
32	104.00	106	14.84	−2056	6.038
33	170.00	3000	2.925	−4960	9.281
34	170.00	3000	2.349	−12510	5.254
35	106.3	600	2.925	−5214	9.355
36	45.00	3000	2.349	−13100	3.702
37	95.31	600	5.275	−8726	6.867
38	38.19	600	5.275	−9655	4.101
39	93.96	3000	5.275	−9389	4.876
40	55.33	106	14.84	−2110	5.884
41	25.00	101.3	3.496	−15870	−9.060
42	80.00	101.3	3.496	−15640	−8.353
43	80.00	101.3	3.461	−15640	−8.353
44	80.00	101.3	0.035	−15640	−8.353
45	80.00	101.3	0.003	789.700	2.430
46	80.00	101.3	0.031	50.490	0.155

- Heat loss for the system is assumed negligible [37].
- Changes in kinetic and potential exergy are assumed negligible [38].
- Steam reformer simulation is conducted using a Gibbs equilibrium reactor model [39].

Notably, in this study, LNG is simulated as pure methane to simplify the thermodynamic formulation and to enable direct comparison with previous conceptual LNG–based system studies that adopt the same assumption [7]. Given that methane is typically the dominant constituent (often exceeding 90% molar fraction) of commercial LNG, this approximation is considered acceptable for a system–level assessment and is not expected to alter the overall performance trends or comparative conclusions, although it may slightly shift the absolute values of some calculated parameters.

3.1.1. *PEME modeling*

Given the PEME modeling, the electrolysis reaction involves electrochemical and thermal processes simultaneously, and can be divided into two stages: the anodic half-reaction and the cathodic half-reaction, whose equations are presented as below [40]:

$$H_2O \rightarrow 2H^+ + \frac{1}{2}O_2 + 2e^+ \quad (7)$$

$$2H^+ + 2e^+ \rightarrow H_2 \quad (8)$$

The PEME is driven by a part of the electrical power from the steam turbine, the process energy demand is expressed as follows [41,42]:

$$\Delta H = \Delta G + T\Delta S \quad (9)$$

In this relation, $T\Delta S$ is the thermal energy demand and ΔG refers to the Gibbs free energy change. In addition, the flow rates of products and reactants can also be obtained according to Faraday's laws and the stoichiometry of the electrolysis reaction [41,42]:

$$\dot{N}_{H_2,out} = \frac{J}{2F}\eta_F = \dot{N}_{H_2O,reacted} \quad (10)$$

$$\dot{N}_{O_2,out} = \frac{J}{4F}\eta_F \quad (11)$$

$$\dot{N}_{H_2O,out} = \dot{N}_{H_2O,in} - \frac{J}{2F}\eta_F \quad (12)$$

where $\dot{N}_{H_2,out}$ is the molar flow rate of hydrogen produced; $\dot{N}_{H_2O,reacted}$ is the molar flow rate of reacted water; $\dot{N}_{O_2,out}$ is the molar flow rate of unreacted water; and $\dot{N}_{H_2O,in}$ is the molar flow rate of incoming water. J and F refers to the current density and Faraday factor, while η_F indicates the efficiency of Faraday. In the current project, the efficiency of Faraday is taken to be 100% because the value has been reported to exceed 99% in numerous studies [43,44]. The electricity required for PEM electrolysis is defined as follows [40]:

$$E_{ele} = J \times V \times N_{cell} \times A_{cell} \quad (13)$$

$$V = V_{act,c} + V_{act,a} + V_{ohm} + V_{con} + V_0 \quad (14)$$

where A_{cell} refers to the efficient cell area, which here the PEM electrolysis area is considered 1 m^2, while N_{cell} represent the number of cells. V_0, V_{act}, V_{ohm}, V_{con} are overpotentials from reversible, activation, ohmic and concentration aspect. If the current density of the PEME is not too high (that is, $J < 10{,}000$ A/m^2), the V_{con} is neglected [45,46].

The V_0 is calculated by the Nernst equation [40,47]:

$$V_0 = 1.229 - 8.5 \times 10^{-4}(T_{PEME} - 298) \quad (15)$$

Table 4
Results of mole fraction for important and key streams of the steam reforming and LNG regasification.

Components	11	21	16	7	26	14	31	34	33
	Mole fraction								
CH_4	0.134	0.000	0.000	1.000	0.000	0.312	0.000	0.000	0.000
CO	0.005	0.000	0.000	0.000	0.000	0.011	0.000	0.000	0.000
CO_2	0.055	0.058	0.000	0.000	0.000	0.127	0.000	0.000	0.000
H_2O	0.574	0.151	0.000	0.000	1.000	0.007	0.456	0.7538	0.2239
H_2	0.233	0.000	0.000	0.000	0.000	0.543	0.000	0.000	0.000
N_2	0.000	0.716	0.79	0.000	0.000	0.000	0.000	0.000	0.000
O_2	0.000	0.074	0.21	0.000	0.000	0.000	0.000	0.000	0.000
NH_3	0.000	0.000	0.000	0.000	0.000	0.000	0.544	0.246	0.7761

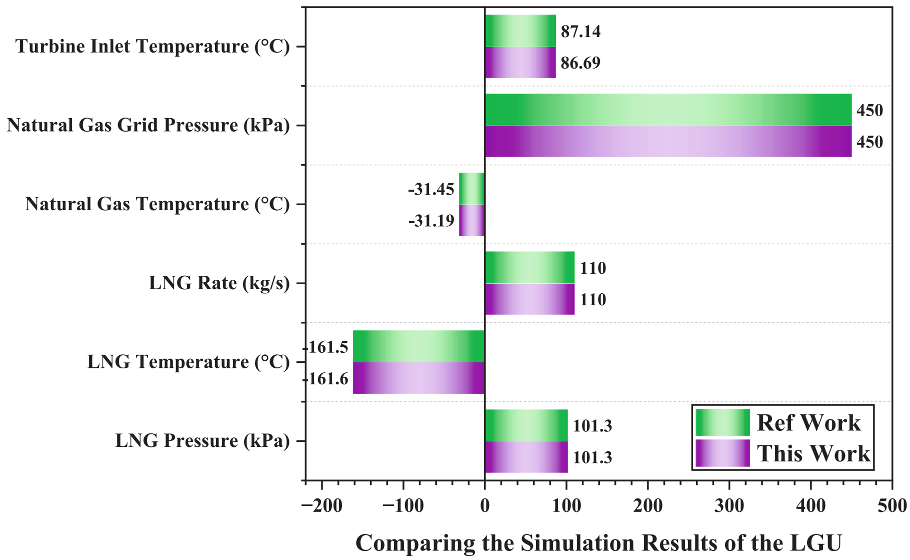

(a)

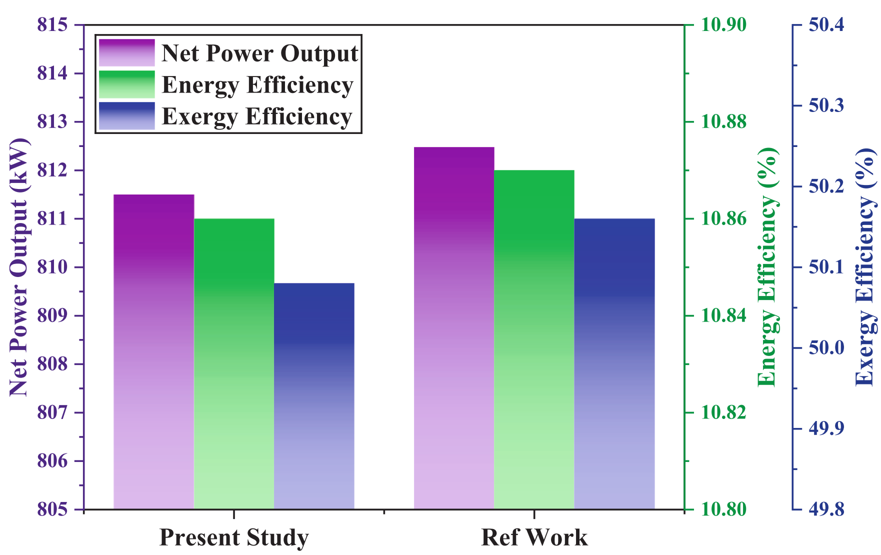

(b)

Fig. 3. Validation of the developed subsystem models against previously reported studies: **(a)** LNG regasification process, **(b)** Kalina cycle, and **(c)** PEME.

where T_{PEME} indicates the electrolyte temperature within the PEME. The V_{ohm} is expressed as [40]:

$$V_{ohm} = JR_{PEME} \quad (16)$$

where R_{PEME} refers to the total ohmic resistance and is calculated as [40]:

$$R_{PEME} = \int_0^L \frac{dx}{\sigma_{PEME}[\lambda(x)]} \quad (17)$$

where L is the membrane thickness, and $\sigma_{PEME}[\lambda(x)]$ indicates the conductivity of local ionic that is determined as follows [42]:

$$\sigma_{PEME}[\lambda(x)] = [0.5139\lambda(x) - 0.326]\exp\left[1268\left(\frac{1}{303} - \frac{1}{T_{PEME}}\right)\right] \quad (18)$$

where $\lambda(x)$ is the water content at location x whin the PEME membrane and is calculated as follows [40]:

$$\lambda(x) = \frac{\lambda_a - \lambda_c}{L} x + \lambda_c \quad (19)$$

In the above equation λ_a and λ_c refer to the water content between the anode-membrane and cathode-membrane. The overpotential of the electrode activation can be expressed as [14]:

$$V_{act,i} = \frac{RT}{F}\sinh^{-1}\left(\frac{J}{2J_{o,i}}\right) = \frac{RT}{F}\ln\left[\frac{J}{2J_{o,i}} + \sqrt{\left(\frac{J}{2J_{o,i}}\right)^2 + 1}\right], \ i = a, c \quad (20)$$

where R represent the gas factor, and $J_{o,i}$ indicates the exchange current density, which can be written as [40]:

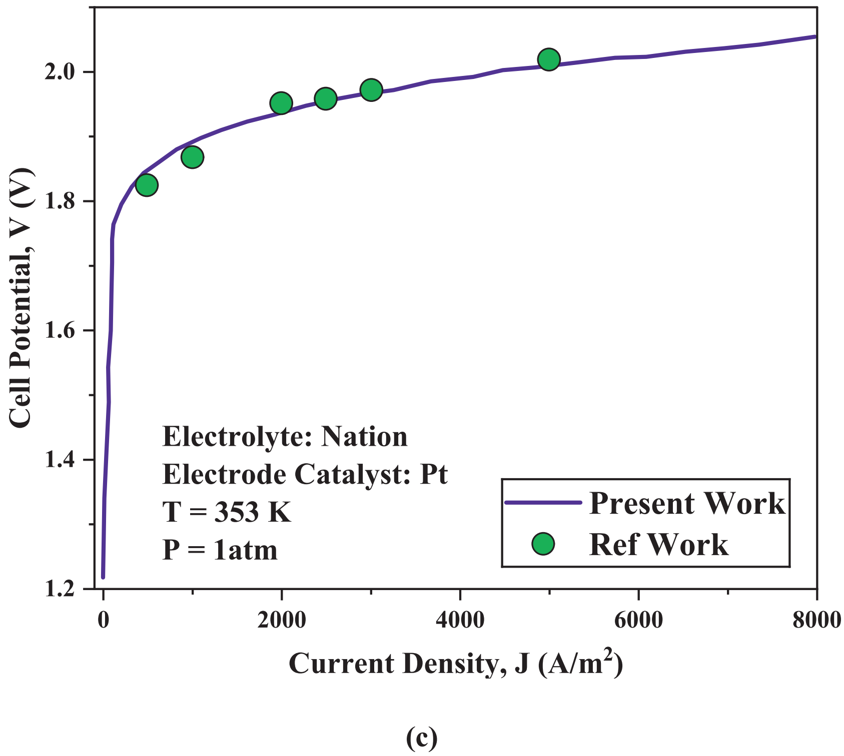

Fig. 3. (*continued*).

Table 5
SMR modeling verification considering Ref. [39].

Parameter	Ref. [39]	This System	Error (%)
Reformer temperature (°C)	900	900	0.0
Reformer duty (kJ/h)	3.861×10^8	3.88×10^8	0.49
Reformer outlet composition (kmole/h)			
CH_4	9.65	9.63	0.21
Ethane-hexane	0.0000114	0.000011	≅ 0
CO	786.46	785.65	0.1
CO_2	473.27	472.39	0.18
H_2	4224.31	4222.58	≅ 0
N_2	2.75	2.75	0.0
H_2O	3720.01	3716.65	0.1

Table 6
Steam Rankine cycle modeling verification regarding Ref. [50].

Parameter	Ref. [50]	This System	Error (%)
Water pressure from pump (kPa)	3819	3819	0
Water temperature from condenser (°C)	35	35	0
Water pressure from condenser (kPa)	6	6	0
Water temperature from evaporator (°C)	416	416	0
Water pressure from evaporator (kPa)	3819	3819	0
Water temperature from turbine (°C)	35	35.28	0.8

$$J_{o,i} = J_i^{ref} \exp\left(-\frac{E_{act,i}}{RT}\right), \quad i = a, c \tag{21}$$

where J_i^{ref} is the pre-exponential factor and $E_{act,i}$ is the activation energy of the anode or cathode.

3.2. System modeling verification

The developed thermodynamic model is validated by comparing the performance of all major subsystems with previously reported experimental or simulation data. LNG regasification results (in Fig. 3(a)), including LNG temperature, pressure, mass flow rate, and natural gas outlet conditions, closely match Ref. [7], indirectly validating the gas–turbine boundary conditions derived from the regasification process. The Kalina cycle model is validated against Ref. [48], demonstrating negligible deviations (<0.1%) in electrical power output and energy-exergy efficiencies (See Fig. 3(b)). In addition, as presented in Fig. 3(c), the PEME model accurately reproduces the experimental

Table 7
The energy and exergy balance equation for each component [56,57].

Components	Energy	Exergy
P-100	$\dot{m}_1h_1 + \dot{W} = \dot{m}_2h_2$	$\dot{E}x_1 + \dot{W} - \dot{E}x_2$
E-100	$\dot{m}_2h_2 + \dot{m}_4h_4 = \dot{m}_3h_3 + \dot{m}_5h_5$	$\dot{E}x_2 + \dot{E}x_4 - \dot{E}x_3 - \dot{E}x_5$
E-101	$\dot{m}_3h_3 + \dot{m}_{20}h_{20} = \dot{m}_6h_6 + \dot{m}_{22}h_{22}$	$\dot{E}x_3 + \dot{E}x_{20} - \dot{E}x_6 - \dot{E}x_{22}$
T-100	$\dot{m}_6h_6 = \dot{W} + \dot{m}_7h_7$	$\dot{E}x_6 - \dot{W} - \dot{E}x_7$
Reformer	$\dot{m}_7h_7 + \dot{m}_{10}h_{10} = \dot{m}_{11}h_{11}$	$\dot{E}x_7 + \dot{E}x_{10} - \dot{E}x_{11}$
E-102	$\dot{m}_9h_9 + \dot{m}_{22}h_{22} = \dot{m}_{10}h_{10} + \dot{m}_{23}h_{23}$	$\dot{E}x_9 + \dot{E}x_{22} - \dot{E}x_{10} - \dot{E}x_{23}$
P-101	$\dot{m}_8h_8 + \dot{W} = \dot{m}_9h_9$	$\dot{E}x_8 + \dot{W} - \dot{E}x_9$
K-100	$\dot{m}_{16}h_{16} + \dot{W} = \dot{m}_{17}h_{17}$	$\dot{E}x_{16} + \dot{W} - \dot{E}x_{17}$
V-100	$\dot{m}_{13}h_{13} = \dot{m}_{14}h_{14} + \dot{m}_{15}h_{15}$	$\dot{E}x_{13} - \dot{E}x_{14} - \dot{E}x_{15}$
E-103	$\dot{m}_{11}h_{11} + \dot{m}_{25}h_{25} = \dot{m}_{13}h_{13} + \dot{m}_{26}h_{26}$	$\dot{E}x_{11} + \dot{E}x_{25} - \dot{E}x_{13} - \dot{E}x_{26}$
T-101	$\dot{m}_{26}h_{26} = \dot{W} + \dot{m}_{27}h_{27}$	$\dot{E}x_{26} - \dot{W} - \dot{E}x_{27}$
E-104	$\dot{m}_{17}h_{17} + \dot{m}_{21}h_{21} = \dot{m}_{19}h_{19} + \dot{m}_{20}h_{20}$	$\dot{E}x_{17} + \dot{E}x_{21} - \dot{E}x_{19} - \dot{E}x_{20}$
Burner	$\dot{m}_{14}h_{14} + \dot{m}_{19}h_{19} = \dot{m}_{18}h_{18}$	$\dot{E}x_{14} + \dot{E}x_{19} - \dot{E}x_{18}$
GT-100	$\dot{m}_{18}h_{18} = \dot{W} + \dot{m}_{21}h_{21}$	$\dot{E}x_{18} - \dot{W} - \dot{E}x_{21}$
E-105	$\dot{m}_{27}h_{27} = \dot{Q} + \dot{m}_{28}h_{28}$	$\dot{E}x_{27} - \dot{E}x_{28}$
P-102	$\dot{m}_{28}h_{28} + \dot{W} = \dot{m}_{29}h_{29}$	$\dot{E}x_{28} + \dot{W} - \dot{E}x_{29}$
PEME	$\dot{m}_{44}h_{44} + \dot{W} = \dot{m}_{45}h_{45} + \dot{m}_{46}h_{46}$	$\dot{E}x_{44} + \dot{W} - \dot{E}x_{45} - \dot{E}x_{46}$
E-106	$\dot{m}_{30}h_{30} + \dot{m}_{23}h_{23} = \dot{m}_{32}h_{32} + \dot{m}_{31}h_{31}$	$\dot{E}x_{30} + \dot{E}x_{23} - \dot{E}x_{32} - \dot{E}x_{31}$
V-101	$\dot{m}_{31}h_{31} = \dot{m}_{33}h_{33} + \dot{m}_{34}h_{34}$	$\dot{E}x_{31} - \dot{E}x_{33} - \dot{E}x_{34}$
E-107	$\dot{m}_{34}h_{34} + \dot{m}_{12}h_{12} = \dot{m}_{36}h_{36} + \dot{m}_{39}h_{39}$	$\dot{E}x_{34} + \dot{E}x_{12} - \dot{E}x_{36} - \dot{E}x_{39}$
T-102	$\dot{m}_{33}h_{33} = \dot{W} + \dot{m}_{35}h_{35}$	$\dot{E}x_{33} - \dot{W} - \dot{E}x_{35}$
E-108	$\dot{m}_{37}h_{37} = \dot{Q} + \dot{m}_{38}h_{38}$	$\dot{E}x_{37} - \dot{E}x_{38}$
P-103	$\dot{m}_{38}h_{38} + \dot{W} = \dot{m}_{12}h_{12}$	$\dot{E}x_{38} + \dot{W} - \dot{E}x_{12}$
E-109	$\dot{m}_{32}h_{32} + \dot{m}_{41}h_{41} = \dot{m}_{40}h_{40} + \dot{m}_{42}h_{42}$	$\dot{E}x_{32} + \dot{E}x_{41} - \dot{E}x_{40} - \dot{E}x_{42}$

Table 8
Life cycle impact assessment values for utilities, focusing on GWP [68,69].

Utilities	GWP	Unit
CO_2	1.000	$kg_{CO_{2-eq}}/kg_{CO_2}$
Steam	0.183	$kg_{CO_{2-eq}}/kg_{steam}$
Cooling water	0.613	$kg_{CO_{2-eq}}/kWh$
CO	1.900	$kg_{CO_{2-eq}}/kg_{CO}$

Table 9
The capital cost functions for i-th component.

Component	Cost Function	CEPCI	Year
Turbine [77]	$4405 \times \dot{W}^{0.7}$	468.2	2005
Pump [78]	$3540 \times \dot{W}^{0.71}$	586	2011
Exchanger [79]	$130\left(\frac{A_{Hx}}{0.093}\right)^{0.78}$	468.2	2005
Reformer [80]	$13 \times 10 \times \left(\frac{A}{0.093}\right)^{0.78} + (3240 \times V^{0.4}) + (2128 \times V)$	386.5	1997
Gas turbine [81]	$479.34 \times \frac{\dot{m}_{in}}{0.92 - \frac{p_{in}}{p_{out}}} \ln \frac{p_{in}}{p_{out}} \times (1 + \exp(0.036T_{in} - 54.41))$	368	1995
Combustor [82]	$6.08 \times \dot{m}_{in} \times \frac{[1 + \exp(0.018T_8 - 26.4)]}{0.995 - \frac{p_{out}}{p_{in}}}$	368.1	1994
Compressor [83]	$7900 \times \dot{W}^{0.62}$	771.1	2021
Electrolyzer [84]	$10^3 \times \dot{W}_{PEME}$	551	2010
$CEPCI_{2023} = 797.9$			

Table 10
Boundary of design parameters for optimization approach.

Design Parameter	Unit	Upper Bound	Lower Bound
LNG flow rate	kg/s	0.5	1.2
Hydrogen production rate	kmol/h	5	20
Water flow rate (steam to reformer rate)	kg/s	1	3
GT-100 outlet pressure, P_{21}	kPa	106	206
T-102 outlet pressure, P_{35}	kPa	400	600
Air-to-burner temperature, T_{19}	°C	700	1200
Air-to-burner flow rate	kg/s	8	24

polarization behavior reported in Ref. [49] over a wide current–density range.

Plus, SMR verification results in Table 5, including reformer duty, operating temperature, and outlet composition, show excellent agreement with Ref. [39], with deviations below 0.5%, confirming the reliability of the Gibbs–equilibrium reformer model. As shown in Table 6, the steam Rankine cycle is verified against Ref. [50], with key thermodynamic state points matching reference values and maximum deviations below 0.8%. The strong agreement observed across all key subsystems confirms the robustness of the adopted thermodynamic and electrochemical models and supports the reliability of the integrated quad–generation system analysis.

It should be noted that the validation of the present integrated system relies on the independent verification of its constituent subsystems, as no experimental benchmark for the full quad-generation configuration is currently available in the literature.

Table 11
Hyperparameter search ranges and selected optimal values in terms of the MLP-surrogate method and Cuckoo Search multi–objective optimization.

MLP			
Optimized Variable	**Type**	**Search Range**	**Selected Value**
Hidden Layers	Integer	1 – 5	3
Neurons	Integer	16 – 512	300
Learning Rate	Continuous	0.0001 – 0.1	0.005
Batch Size	Integer	16 – 128	52
Dropout Rate	Continuous	0 – 0.5	0.2
L2 Regularization	Continuous	$1 \times 10^{-6} – 1 \times 10^{-2}$	1×10^{-2}
Activation Function	Categorical	ReLU / Tanh / ELU	–
Optimizer Type	Categorical	Grid Search CV	–
Cuckoo Search Parameter	**Description**	**Search Space / Range**	
Population Size (N)	Number of nests / candidate solutions	10 – 100	50
Discovery Probability (Pa)	Probability of nest replacement	0.1 – 0.5	0.3
Maximum Iterations	Optimization termination criterion	50 – 300	150
Lévy Flight Step Size (α)	Search movement coefficient	0.01 – 2.0	0.1
Lévy Exponent (β)	Distribution control parameter	1.0 – 2.0	1.6
Randomization Factor	Exploration coefficient	0.01 – 1.0	0.05
Lower Bound	Minimum search boundary	Variable dependent	–
Upper Bound	Maximum search boundary	Variable dependent	–
Fitness Function	Optimization objective	Minimize RMSE / MAE	–
Stopping Criterion	Search termination condition	Max iteration / convergence	–
Search Dimension	Number of optimized MLP variables	5 – 12	12
Elitism Strategy	Best solution retention	Enabled / Disabled	–
Constraint Handling	Boundary control method	Clipping / Reflection	–

3.3. System evaluation

3.3.1. Energy and exergy modeling

In this study, a steady-state energy-exergy evaluation of the proposed quad–generation system is implemented. The following equations and definitions form the basis for the detailed energy and exergy evaluation of the suggested system.

The general energy balance for a control volume at steady state can be written as [51,52]:

$$\dot{W} - \dot{Q} = \sum \dot{m}_{in} h_{in} - \sum \dot{m}_{out} h_{out} \tag{22}$$

in which $\dot{W}$ and $\dot{Q}$ are the generated power rate (rate of work) and transferred heat rate, respectively; $\dot{m}_{in}$ and $\dot{m}_{out}$ are the input and output mass flow rates, and h_{in} and h_{out} refer to the corresponding specific enthalpies.

In the present study, exergy analysis is fallen apart into chemical and physical units, neglecting potential and kinetic contributions, as shown by Eq. (23) [53]:

$$\dot{Ex} = \dot{Ex}_{PH} + \dot{Ex}_{CH} \tag{23}$$

The exergy balance for a component or subsystem is calculated based on Eq. (24) [54]:

$$\dot{Ex}_F = \dot{Ex}_D + \dot{Ex}_P \tag{24}$$

where the exergy destruction rate is indicated by $\dot{Ex}_D$ and the exergy

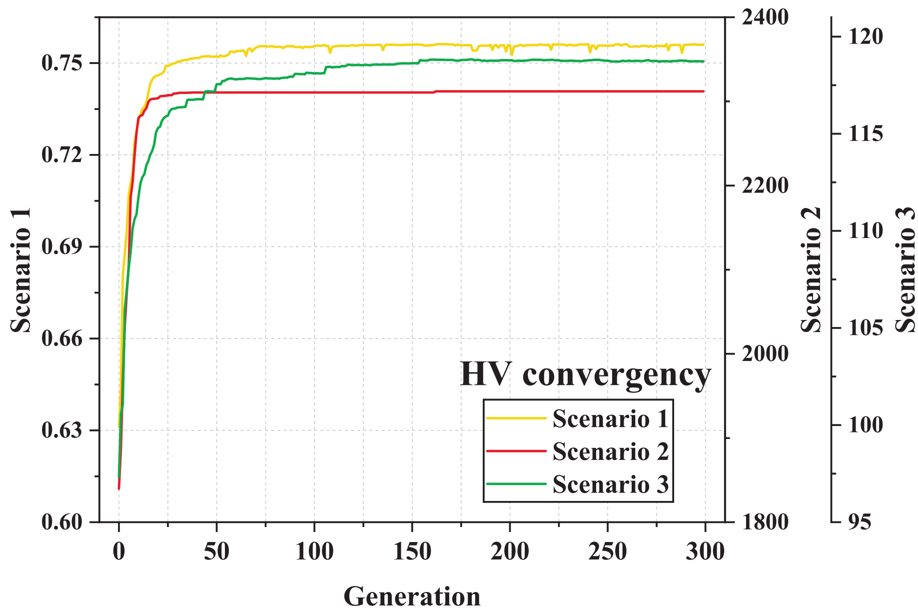

Fig. 4. Convergence of the HV metric over 300 generations for the three multi-objective optimization scenarios based on MLP-Cuckoo Search algorithm.

Table 12
Thermodynamic performance parameters and pinch-point data for the system's heat exchangers.

Component	LMTD (°C)	Heat Duty (kW)	Min. Approach (°C)	Hot Pinch Temp. (°C)	Cold Pinch Temp. (°C)
Heat Exchangers					
E-100	57.7593	401.1381	20.0000	25.0000	5.0000
E-101	421.9394	1411.2945	159.9915	959.9413	799.9498
E-102	93.9573	8534.9595	7.4996	887.5411	880.0415
E-103	59.9049	6976.5717	3.6329	30.0000	26.3671
E-104	623.4421	7120.1859	614.8585	1314.8585	700.0000
E-106	70.3904	5621.7839	10.0002	103.9528	93.9527
E-107	22.5424	1379.9095	6.3867	45.0000	38.6133
E-109	22.2089	803.0163	23.9528	103.9528	80.0000

rate of the fuel (input exergy) and that of the product (useful exergy output) are correspondingly indicated by $\dot{E}x_F$ and $\dot{E}x_P$.

The destruction ratio of exergy for the i-th component or subsystem (β_i) is defined as [55]:

$$\beta_i = \frac{\dot{E}_{D,i}}{\sum_{j=1}^{i}\dot{E}_{D,j}} \tag{25}$$

and the efficiency of exergy for the i-th component or subsystem (ψ_i) is determined by the following equation [55]:

$$\psi_i = 100 \times \frac{\dot{E}_{P,i}}{\dot{E}_{F,i}} \tag{26}$$

The energy and exergy balance equation for each component are depicted in Table 7.

The primary energy saving ratio (PESR) measures the potential reduction in the primary energy consumption of the suggested system in comparison with a reference system that provides the same products, based on the following equations [58]:

$$PESR = \frac{PE_{ref} - PE_{MG}}{PE_{ref}} \tag{27}$$

$$PE_{ref} = \frac{\dot{W}_{net}^{MG}}{\eta_{elect}^{ref}} + \frac{\dot{Q}_{heating}}{\eta_{th}^{ref}} + \frac{\dot{Q}_{cooling}}{\eta_{elect}^{ref} \times COP_{ref}} \tag{28}$$

In Eq. (28), $\dot{W}_{net}^{MG}$ is the net electrical power delivered by the MG system, $\dot{Q}_{heating}$ and $\dot{Q}_{cooling}$ are the useful heating and cooling loads, COP_{ref} depicts the performance coefficient of the reference chiller ($COP_{ref} = 3$), and η_{th}^{ref} and η_{elect}^{ref} are the reference thermal and electrical efficiencies, correspondingly equaling 80% and 33% [59].

In the SMR section, the conversion rate of methane into syngas is calculated by:

$$\chi_{CH_4} = \frac{CH_{4,i} - CH_{4,o}}{CH_{4,i}} \tag{29}$$

in which the molar flow rates of methane at the reformer input and output are respectively indicated by $CH_{4,i}$ and $CH_{4,o}$.

The energetic efficiency of the reforming section has been determined as:

$$\eta_{reforming} = \frac{\dot{W}_{net} + \dot{Q}_{cooling} + \dot{Q}_{SG}}{\dot{Q}_F + \dot{Q}_{E101} + \dot{Q}_{E102}} \tag{30}$$

where $\dot{Q}_{cooling}$ is the useful cooling duty provided by the reformer-associated heat exchanger, $\dot{Q}_{SG}$ is the heat recovered as superheated steam or syngas, $\dot{Q}_F$ is the chemical energy of the fuel supplied to the burner, and $\dot{Q}_{E101}$ and $\dot{Q}_{E102}$ are the heat duties in the associated heat exchangers E101 and E102. These terms are calculated as:

$$\dot{Q}_{cooling} = \dot{m}_3(h_3 - h_2) \tag{31}$$

$$\dot{Q}_F = \dot{m}_1 LHV_1 \tag{32}$$

$$\dot{Q}_{E101} = \dot{m}_{20}(h_{20} - h_{22}) \tag{33}$$

Similar definitions are used for $\dot{Q}_{E102}$ (not shown for brevity). Also, the energy efficiency of the gas turbine, steam Rankine cycle, and Kalina cycle are calculated as [60]:

$$\eta_{gas\ turbine} = \frac{\dot{W}_{net}}{\dot{Q}_{SG}} = \frac{\dot{W}_{GT100} - \dot{W}_{K100}}{\dot{m}_{14} LHV_{14}} \tag{34}$$

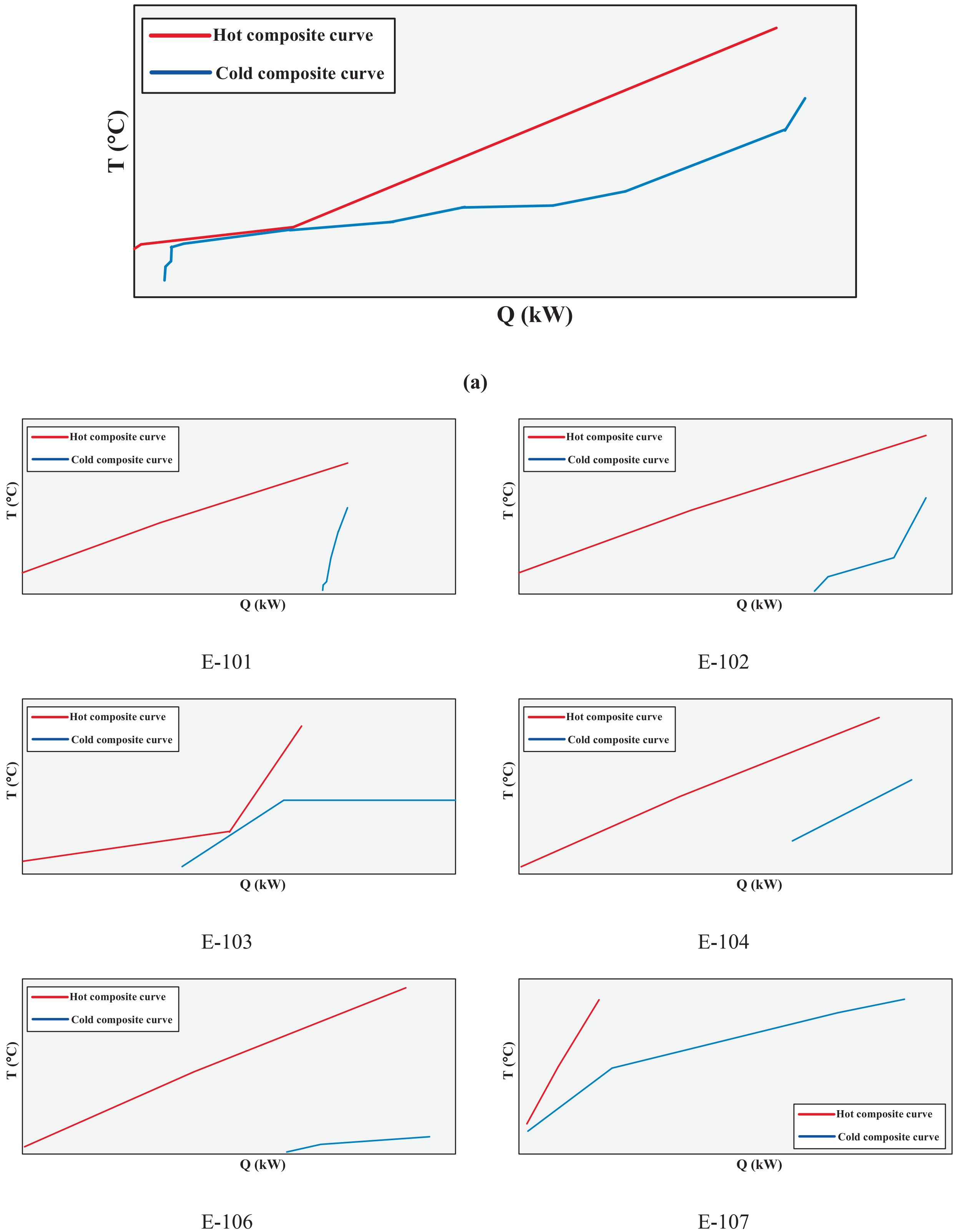

(b)

Fig. 5. T-Q composite curves for **(a)** the integrated proposed system and **(b)** individual heat exchanger units.

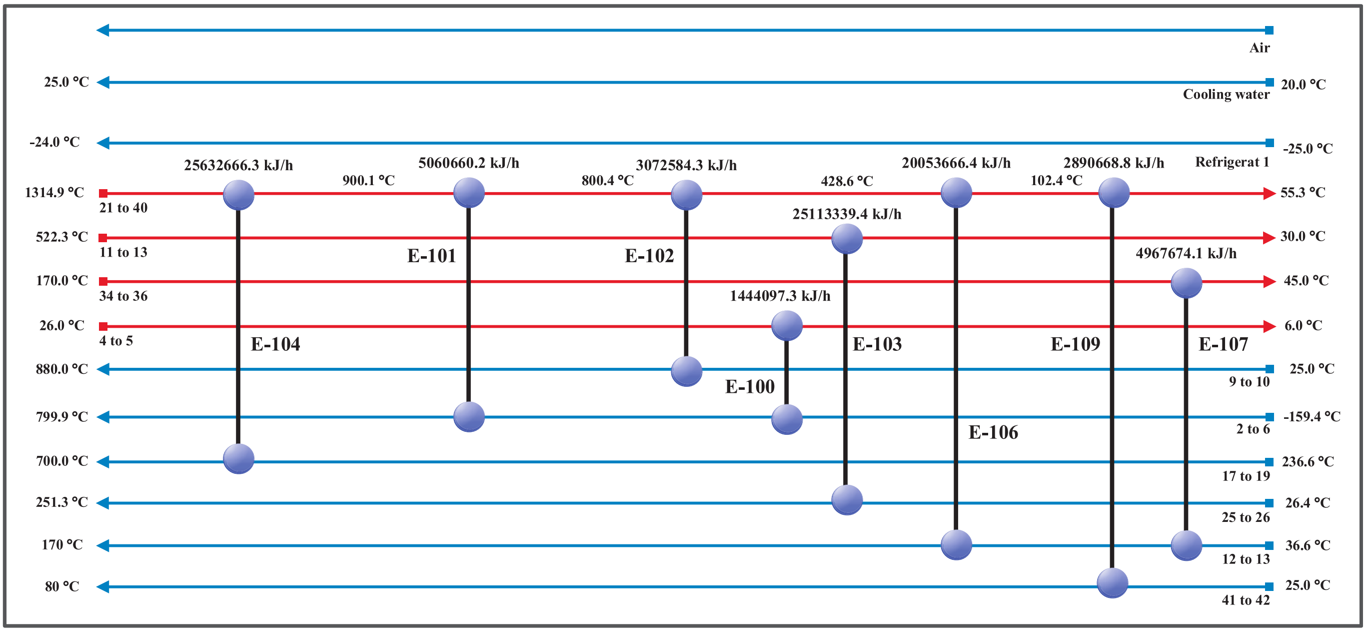

Fig. 6. Heat exchanger network grid design illustrating the stream coupling and heat recovery configuration.

Table 13
The results of exergy-related parameters.

Component	$\dot{E}x_F$	$\dot{E}x_P$	$\dot{E}x_D$	ψ_i	β_i
E-100	541	292	249	0.53	0.020
E-101	1067	750	317	0.70	0.025
T-100	445	428	17	0.96	0.001
Reformer	31,355	31,026	329	0.98	0.026
P-100	9	7	2	0.78	0.000
P-101	3	2	1	0.67	0.000
E-102	5758	3399	2359	0.59	0.190
E-106	2430	1512	918	0.62	0.074
E-103	2489	2370	119	0.95	0.010
T-101	2524	2272	252	0.90	0.020
E-105	66	43	23	0.65	0.001
P-102	14	11	3	0.78	0.000
V-100	309	309	0	0.99	0.000
K-100	3088	2904	184	0.94	0.015
E-104	5595	4180	1415	0.74	0.113
Burner	34,860	29,984	4876	0.86	0.391
GT-100	13,030	12,760	270	0.98	0.022
PEME	911	464	447	0.51	0.036
E-109	375	317	58	0.84	0.004
V-101	1950	1939	11	0.99	0.001
T-102	809	743	66	0.91	0.005
E-107	293	166	127	0.56	0.010
E-108	802	409	393	0.51	0.032
P-103	23	17	6	0.73	0.000

$$\eta_{Rankine} = \frac{\dot{W}_{net}}{\dot{Q}_{VG}} = \frac{\dot{W}_{T101} - \dot{W}_{P102}}{\dot{m}_{11}(h_{11} - h_{13})} \quad (35)$$

$$\eta_{Kalina} = \frac{\dot{W}_{net}}{\dot{Q}_{VG}} = \frac{\dot{W}_{T102} - \dot{W}_{P103}}{\dot{m}_{23}(h_{23} - h_{32})} \quad (36)$$

For evaluating the total thermodynamic performance of the newly presented system, the electrical, energy, and exergy efficiencies of the system are respectively defined as:

$$\eta_{MG,\ ELE} = \frac{\dot{W}_{net}^{MG}}{\dot{Q}_F} \quad (37)$$

$$\eta_{MG} = \frac{\dot{W}_{net}^{MG} + \dot{Q}_{cooling} + \dot{Q}_{H2} + \dot{Q}_{heating}}{\dot{Q}_F} \quad (38)$$

$$\psi_{MG} = \frac{\dot{W}_{net}^{MG} + \dot{E}x_{cooling} + \dot{E}x_{H2} + \dot{E}x_{heating}}{\dot{E}x_F} \quad (39)$$

In Eqs. (37)–(39), $\dot{W}_{net}^{MG}$ is the net electrical power output of the entire MG system, $\dot{Q}_{cooling}$ is the useful cooling load, $\dot{Q}_{heating}$ is the useful heating load delivered by the hot water stream, and $\dot{Q}_{H2}$ is the energy associated with the hydrogen product, defined as:

$$\dot{Q}_{H2} = \dot{m}_{45} LHV_{45} \quad (40)$$

$\dot{E}x_{heating}$ is the exergy of the heating product:

$$\dot{E}x_{heating} = \dot{Q}_{heating} \times \left(1 - \frac{T_0}{T_{43}}\right) = \dot{m}_{43}(h_{43} - h_{41}) \times \left(1 - \frac{T_0}{T_{43}}\right) \quad (41)$$

$\dot{E}x_{cooling}$ is the exergy of the cooling product:

$$\dot{E}x_{cooling} = \dot{Q}_{cooling} \times \left(\frac{T_0}{T_5} - 1\right) \quad (42)$$

$\dot{E}x_{H2}$ is the total exergy of the hydrogen product, including physical and chemical parts:

$$\dot{E}x_{H2} = \dot{E}x_{H2}^{PH} + \dot{E}x_{H2}^{CH} \quad (43)$$

$\dot{E}x_F$ is the total exergy of the fuel supplied to the system:

$$\dot{E}x_F = \dot{E}x_F^{PH} + \dot{E}x_F^{CH} \quad (44)$$

Here, T_0 is the ambient temperature, and T_{43} and T_5 are the temperatures at which heating and cooling are delivered, respectively. LHV_{45} is the lower heating value of hydrogen, and $\dot{m}_{45}$ is the hydrogen mass flow rate.

In addition, the net electrical power output of the system ($\dot{W}_{net}$) is calculated as the total power produced by all turbines ($\sum \dot{W}_T$) minus the total power consumed by pumps ($\sum \dot{W}_P$), compressors ($\sum \dot{W}_K$), and the electrical power demand of the PEME ($\dot{W}_{PEME}$).

$$\dot{W}_{net}^{MG} = \sum \dot{W}_T - \sum \dot{W}_P - \sum \dot{W}_K - \dot{W}_{PEME} \quad (45)$$

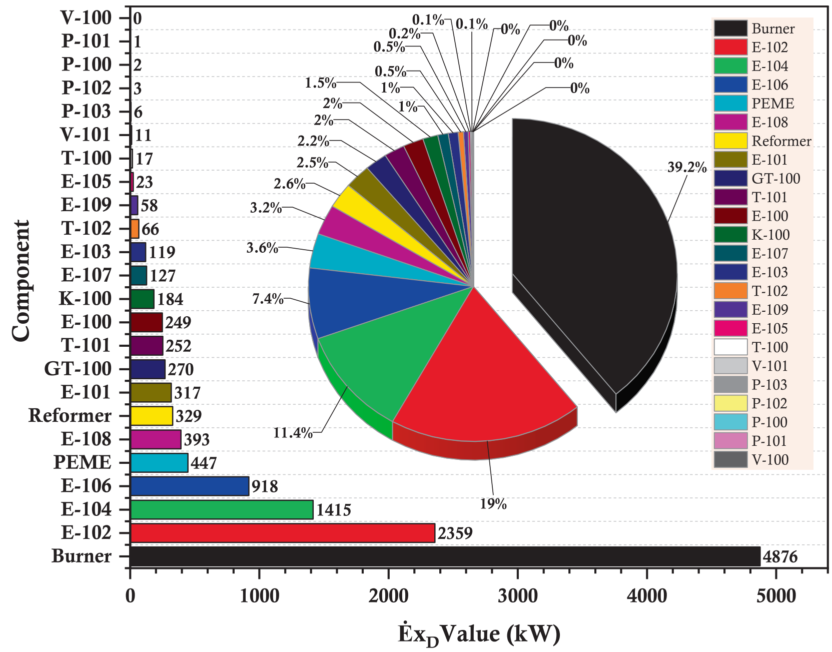

(a)

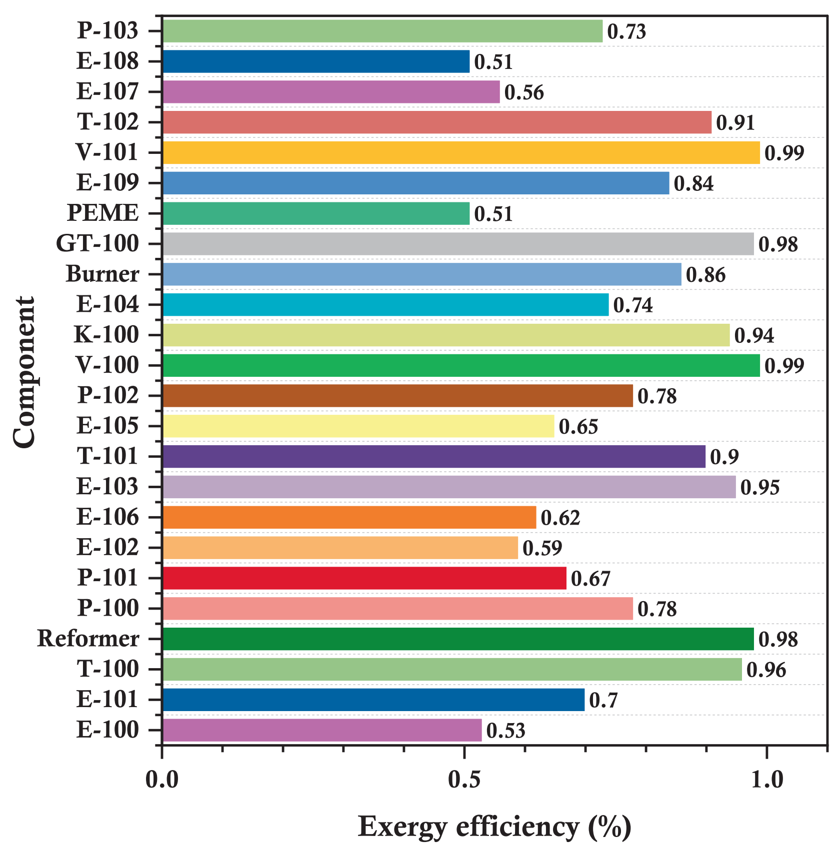

(b)

Fig. 7. **(a)** Comparison of destroyed exergy by each component, and **(b)** Comparison of exergy efficiency of each component.

Table 14
The detailed costs and associated hourly cost rates of components.

Component	Cost ($)	Cost Rate ($/h)
P-103	69,100	1.00
E-108	43,600	0.63
T-102	471,200	6.83
E-100	15,600	0.23
E-107	27,900	0.40
E-109	101,600	1.47
GT-100	3,296,411	47.80
P-100	118,400	1.72
Reformer	399,554	5.79
P-102	68,000	0.99
Burner	141,026	2.04
T-100	306,166	4.44
E-106	329,300	4.77
P-101	6600	0.10
E-102	215,662	3.13
V-100	25,600	0.37
T-101	984,990	14.28
V-101	39,800	0.58
E-103	175,000	2.54
E-104	403,622	5.85
K-100	1,151,402	16.69
E-101	169,047	2.45
PEME	911,000	13.21
E-105	58,300	0.85
Total = 9528880 $		

3.3.2. *Environmental modeling*

In this study, the environmental performance of the proposed system is evaluated by calculating the CO_2 footprint of system. The specific CO_2 emission parameter (ω_{CO_2}) is used to quantify the footprint (i.e. the environmental impact) of the system [61]:

Table 15
Detailed CAPEX-related calculations for the integrated quad-generation system.

Parameter	Equation [87]	Value ($)
CAPEX		
Direct Costs (DC)		
Total purchased equipment cost (TPEC)	100%	9,528,880
Purchased equipment installation	40%	3,811,552
Instrumentation and controls	20%	1,905,776
Piping	15%	1,429,332
Electrical systems	15%	1,429,332
Buildings (including services)	30%	2,858,664
Yard improvements	10%	952,888
Service facilities (waste treatment, receiving, shipping, packaging, storage, offices, etc.)	20%	1,905,776
Total direct cost		**23,822,200**
Indirect Costs (IC)		
Engineering and supervision	25%	2,382,220
Contingency	30%	2,858,664
Legal and contractors' fees	10%	952,888
Startup/construction	10%	952,888
Total indirect cost		**7,146,660**
Additional investment		
Working capital (WC)	15% of FCI	4,645,329
Fixed capital investment (FCI)	FCI = DC + IC	30,968,860
Total capital investment (TCI)	**TCI = FCI + WC**	**35,614,189**

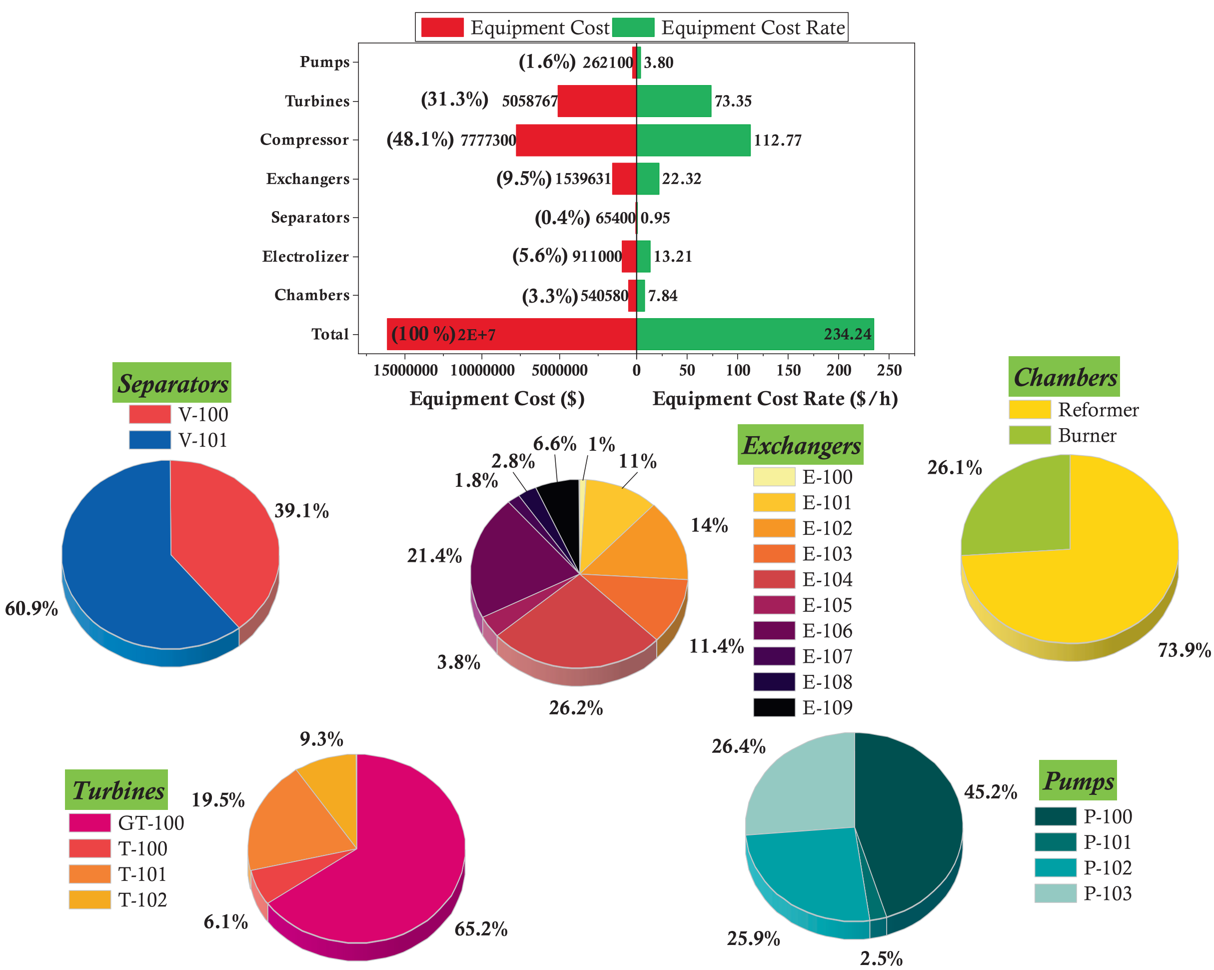

Fig. 8. The comparison of each component cost and their share in overall cost.

Table 16
Detailed OPEX-related estimations for the proposed quad-generation system.

Parameter	Equation [93]	Value ($)
Raw material	LNG 5 $/GJ	3,353,015
Utilities (electricity, fuel, stream, water, air, refrigeration and cool agent)	10% of total product cost	3,268,054
Operating and maintenance		
Operating labor	46 labors/shift, 3 shifts/day, 60,000 $/labor/year	8,280,000
Supervision	20% of operating labor	1,656,000
Maintenance and repairs	6% of fixed capital investment	1,858,132
Maintenance supplies	15% of maintenance and repairs	278,720
Laboratory charges	15% of operating labor	1,242,000
Patents and royalties (indirect cost)	1% of total product cost	326,805
Depreciation	Recovery period 20 years, salvage value 5%	1,471,021
Local taxes and insurance	3% of fixed capital investment	929,066
Plant overhead costs	60% of (3.1 + 3.2 + 3.3)	7,076,479
General expenses		
Administration	5% of production cost	1,634,027
Marketing	5% of total production cost	1,634,027
Research and development (R&D)	4% total production cost	1,307,222
Total product cost (TPC)	1 + 2 + 3 + 4 + 6 + 7 + 8	32,680,540

$$\omega_{CO_2} = \frac{\dot{m}_{CO_2}}{\text{energy rate of the resultant products}} = \frac{\dot{m}_{CO_2}}{\dot{W}_{net}^{MG} + \dot{Q}_{heating} + \dot{Q}_{cooling} + \dot{E}n_{H2}} \quad (46)$$

where $\dot{m}_{CO_2}$ refers to the total emission rate of CO_2 in the flue gas, which is determined to be 4892 kg/h based on the simulation results. The denominator represents the total useful energy output of the MG system, including the net electrical power ($\dot{W}_{net}^{MG}$), useful cooling load ($\dot{Q}_{cooling}$), useful heating load ($\dot{Q}_{heating}$), and the energy associated with the produced hydrogen ($\dot{E}n_{H2}$) calculated based on its lower heating value. This formulation expresses the CO_2 emission intensity relative to the overall useful energy products of the system [62].

On the other hand, this study calculates the Sustainability index (SI) parameter to assess the sustainability of the system by considering input and output exergy, and exergo-environmental impact improvement (EII) parameter to indicate the level of enhancement in exergy-related environmental effect using Eqs. (47) and (48) [63,64]:

$$SI = \frac{\dot{E}x_F}{\dot{E}x_F - \dot{E}x_P} \quad (47)$$

$$EII = \frac{\dot{E}x_F - \dot{E}x_P}{\dot{E}x_F} \quad (48)$$

In addition, in order to comprehensively evaluate the environmental performance of the proposed system, a gate-to-gate boundary for the life cycle assessment (LCA) is established [65]. This approach encompasses both indirect emissions associated with the operational utilities and direct emissions in terms of the combustion process. The total global warming potential (GWP_{total}) has been calculated via the following expression [66]:

$$GWP_{total}\left(kgCO_{2-eq}FU^{-1}\right) = \sum GWP_{direct} + \sum GWP_{indirect} - Captured_{CO2} \quad (49)$$

where GWP_{direct} represents the CO_2 and CO emissions directly released from the flue gas [67], and $GWP_{indirect}$ shows the environmental impact of utility streams, specifically steam (0.18302 $kg_{CO2\text{-}eq}/kg_{steam}$) and the electricity required for cooling water pumping (0.61365 $kg_{CO2\text{-}eq}$/kWh). The GWP values for key utilities, including steam and cooling water, are provided in Table 8 based on established literature data.

3.3.3. Economic modeling

In this study, an economic evaluation of the proposed system is done using the exergo-economic and thermo-economic costs of the system. The following equations are used to calculate the exergo-economic cost using total unit cost of product (TUCP) [70], which is based on total cost rate (TCR) [71]:

$$TUCP\ (\$/GJ) = \frac{TCR}{\sum \dot{E}x_P} \quad (50)$$

$$TCR = \sum \dot{Z}_i^{CI+OM} + \dot{C}_F \quad (51)$$

The economic performance of the proposed system is further evaluated using the total annual cost (TAC), which is defined as the sum of the annualized capital expenditure ($CAPEX_{annual}$) and the annual operating expenses (OPEX). The $CAPEX_{annual}$ is determined by multiplying the total capital investment (TCI) by the capital recovery factor (CRF) [72]. Additionally, the levelized cost of energy (LCOE) is calculated as the ratio of the TAC to the total annual energy production, providing a standardized measure of the unit cost of energy generated [3].

$$TAC = CAPEX_{annual} + OPEX \quad (52)$$

$$CAPEX_{annual} = CRF \times TCI \quad (53)$$

$$LCOE = \frac{TAC}{\text{annual product of energy}} \quad (54)$$

The LNG fuel cost rate is indicated by $\dot{C}_F$ and is computed using following equation [3]:

$$\dot{C}_F = c_F \times \dot{E}x_F \quad (55)$$

in which the $\dot{E}x_F$ parameter refers to exergy rate of input fuel, while c_F represents the cost factor for LNG fuel, which is considered equal to 5 $/GJ [3].

The $\dot{Z}_i^{CI+OM}$ is composed of capital investment cost ($\dot{Z}_i^{CI}$) and operation and maintenance cost ($\dot{Z}_i^{OM}$) for each i-th component. The $\dot{Z}_i^{CI}$ and $\dot{Z}_i^{OM}$ is calculated using following equations [73]:

$$\dot{Z}_i^{CI} = \frac{1.06 \times CRF \times Z_i}{t_y} \quad (56)$$

$$\dot{Z}_i^{OM} = 1.5\% \dot{Z}_i^{CI} \quad (57)$$

where t_y is the annual working hours, which is considered equal to 7,446 h [74]. The Z_i refers to the capital cost of i-th component using the equations in Table 9. CRF is computed using the following equation [75]:

$$CRF = \frac{q \times (q+1)^n}{(q+1)^n - 1} \quad (58)$$

in which q refers to rate of interest and n represents the lifetime of the system, which are 8% and 20 years [76].

Based on following calculation, the profit for the system is computed using Eq. (59) [85]:

$$Profit = \sum_{1}^{n=20} \frac{AS}{(1+q)^n} - FC \quad (59)$$

$$AS = AI - \dot{C}_F - \sum \dot{Z}_i^{OM} \quad (60)$$

in which AS and AI refers to the annual saving and income, which is calculated on the basis of heating price ($P_{heating}$) of 0.018 $/kWh, power price ($P_{ele}$) of 0.07 $/kWh [86], cooling price ($P_{cooling}$) of 0.08 $/kWh, and hydrogen price (P_{H2}) of 4 $/kg [85]. FC is the fixed cost, which

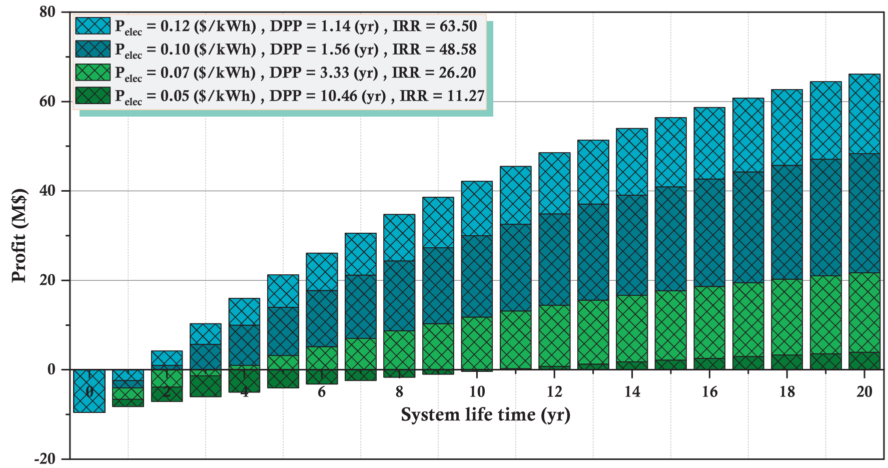

(a)

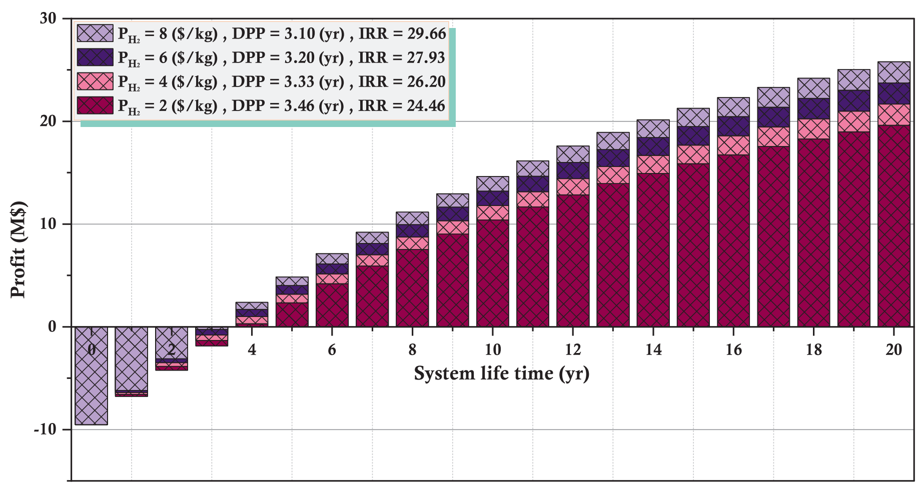

(b)

Fig. 9. The comparison of the system profit under various product prices including **(a)** electricity, **(b)** hydrogen, **(c)** cooling, **(d)** heating, and **(e)** LNG fuel costs.

includes the direct and indirect costs [85].

The dynamic payback period (DPP) takes into account the time value of money and calculates the investment return time using the following equation [85]:

$$DPP = \min\{n : \text{Profit}(n) > 0\} \tag{61}$$

The internal return rate (IRR) is computed as below [87]:

$$0 = \frac{AS}{6.32^* \sum \dot{Z}_i^{CI}}\left(1 - \frac{1}{(1 + IRR)^n}\right) \tag{62}$$

3.4. System optimization

In the complex energy system with intricate processes and several performance goals, the utilization of optimization techniques is essential for improving energy systems' quality, cost-effectiveness, and environmental performance [88]. In this study, the optimization process starts by methodically simulating the system and creating a dataset that illustrates the connection between decision variables and performance outcomes. A sum of dataset of 1200 samples is produced from detailed process simulations covering the feasible operating region. The dataset is divided into 900 samples (75%) for training and validation and 300 samples (25%) for testing. The design space is defined by several key decision variables, including the LNG flow rate at stream 1, hydrogen production rate at stream 45, water flow rate at stream 8, GT–100 outlet pressure (P_{21}), T–102 outlet pressure (P_{35}), air-to-burner temperature (T_{19}), and air-to-burner flow rate. The operating bounds of these variables are presented in Table 10.

This study uses an integrated framework that combines multi-dimensional optimization algorithm ability with an MLP model to capture the behavior of the system under various operating conditions. The MLP model refers to a feedforward neural network composing an input layer, several hidden layers with non-linear activating functions, and an output layer that approximates the relationship between design variables and system performance indicators. The generated simulation dataset is used to train the MLP model using Python software. To improve model generalization and prevent overfitting, a five–fold cross–validation procedure is applied during the training process. In addition, Grid Search Cross–Validation (Grid Search CV) is employed to determine the optimal hyperparameters of the MLP model. The detailed hyperparameter search ranges and selected values are presented in Table 11. The predictive performance of the trained network is evaluated using several statistical metrics including root mean square error

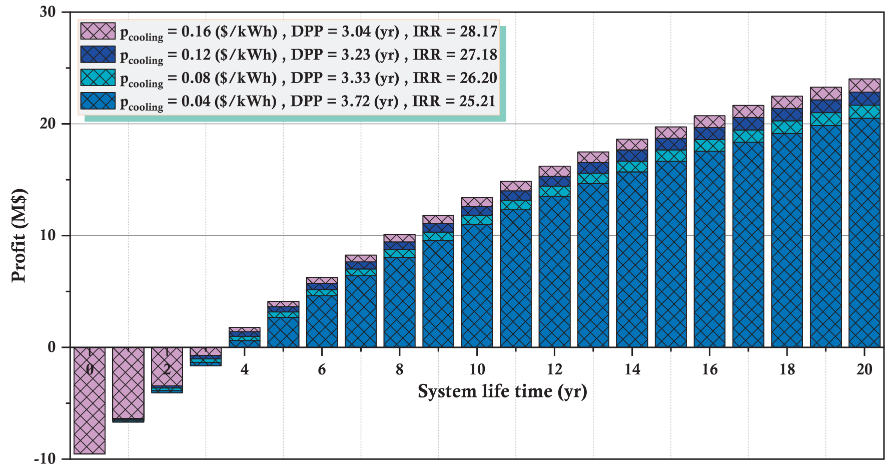

(c)

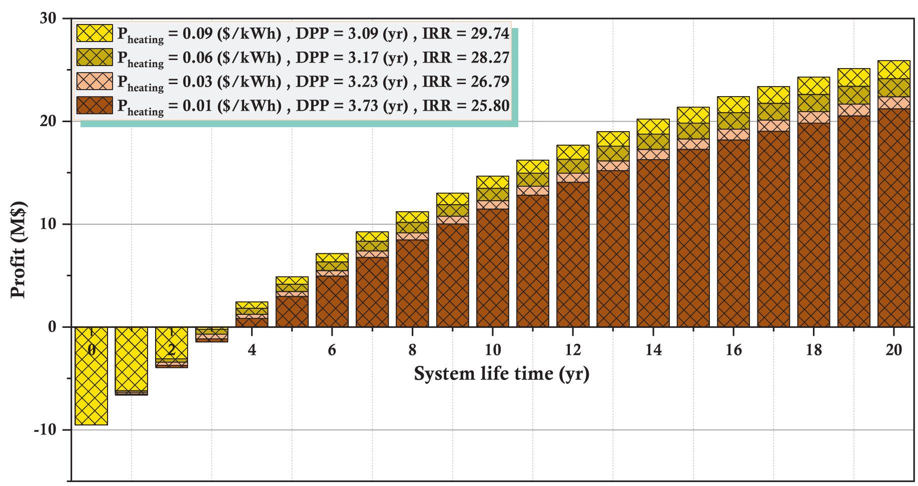

(d)

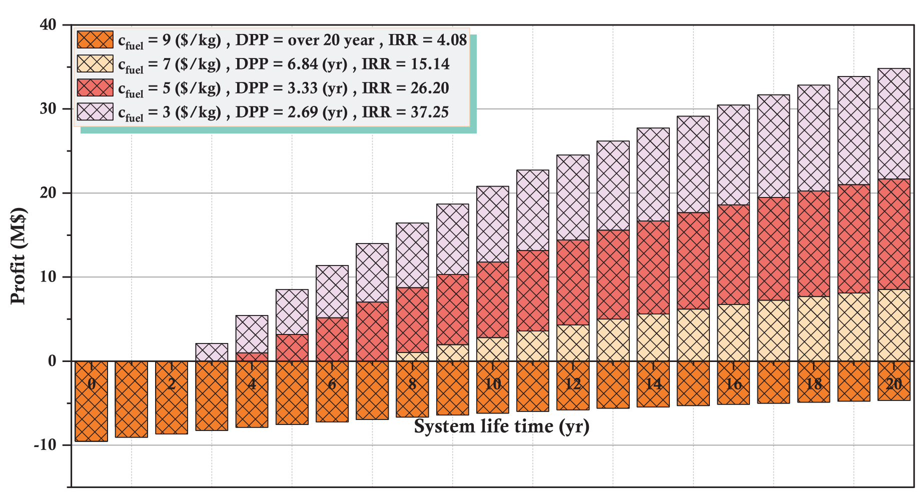

(e)

Fig. 9. (*continued*).

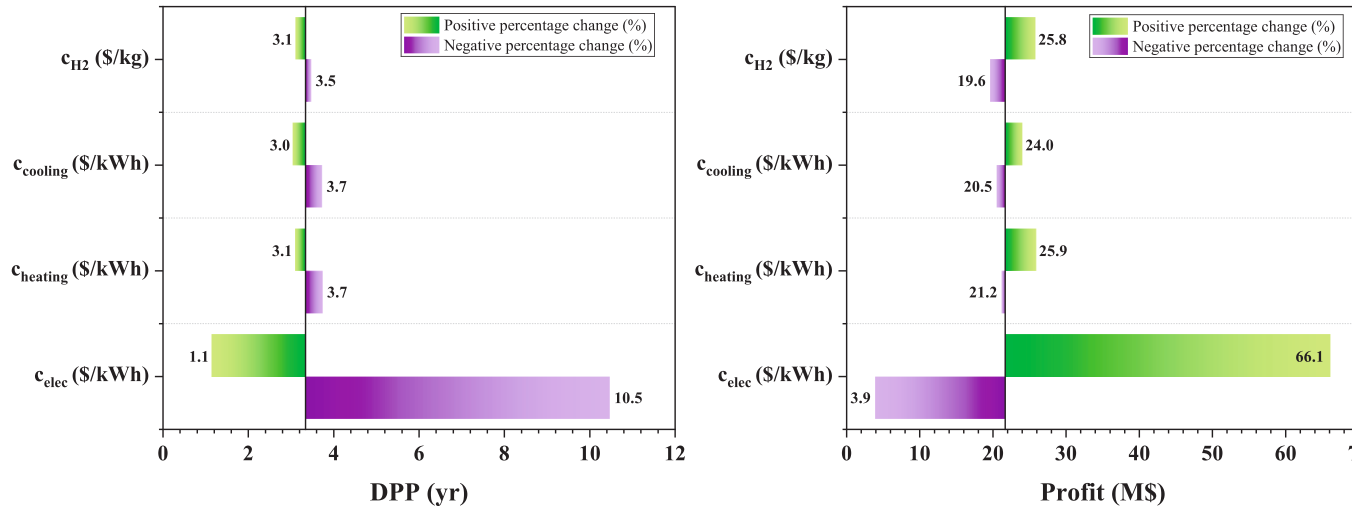

Fig. 10. Sensitivity analysis of the Profit and DPP to selling-buying prices.

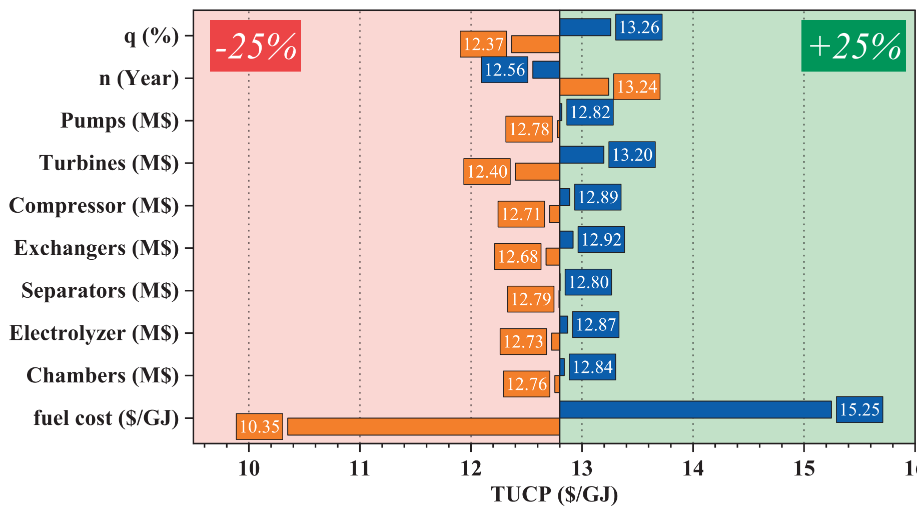

Fig. 11. Tornado diagram for the one-way sensitivity analysis of the TUCP in terms of a ± 25% variation in major economic parameters.

Table 17
LCA results showing the contribution of direct emissions and utility-related indirect emissions to the total GWP of the system.

Parameter	Value
Direct GWP ($kg_{CO2\text{-}eq}$/h)	4892
Steam GWP ($kg_{CO2\text{-}eq}$/h)	963
Cooling water pumping GWP ($kg_{CO2\text{-}eq}$/h)	5903
CO GWP ($kg_{CO2\text{-}eq}$/h)	49
Indirect GWP ($kg_{CO2\text{-}eq}$/h)	6915
Total GWP ($kg_{CO2\text{-}eq}$/h)	11,807
Total GWP per produced energy ($kg_{CO2\text{-}eq}$/kWh)	0.8536

(RMSE), mean absolute error (MAE), mean absolute percentage error (MAPE), and coefficient of determination (R^2) [89,90].

This trained MLP model drastically cuts down on computational costs by replacing direct simulations during optimization stage. Subsequently, the Cuckoo Search algorithm is used to effectively explore the optimization landscape. This nature-inspired metaheuristic algorithm is based on the brood parasitism behavior of cuckoo birds, which lay eggs in other species' nests. The algorithm employs Lévy flight random walks to generate new candidate solutions and improve exploration of the search space [91]. The main update mechanism of the algorithm is expressed as:

$$x^{(t+1)}{}_i = x^{(t)}{}_i + \alpha \times \text{Levy}(\lambda) \tag{63}$$

where Levy(λ) indicates a random step taken from a Lévy distribution and α is the step size, allowing a balance between local exploitation and global exploration of the solution space. The complete parameter settings are summarized in Table 11.

The Cuckoo Search algorithm iteratively eliminates less-fitting solutions and keeps those with higher fitness values, ultimately creating a Pareto front of non-dominated solutions that represent the best possible trade-offs between competing objectives. Fig. 4 illustrates the convergence behavior of the proposed multi-objective optimization algorithm across three different scenarios. All scenarios exhibit a rapid initial increase in the Hypervolume (HV) metric, indicating a fast exploration and improvement of the Pareto front. Scenarios 1 and 2 achieve stability within the first 50–75 generations, while Scenario 3 reaches a steady state by approximately generation 150. The plateauing of all curves confirms that the Cuckoo Search algorithm successfully converged to a set of optimal non-dominated solutions within the predefined 300 generations.

Finally, the Linear Programming Technique for Multidimensional Analysis of Preference (LINMAP) method is applied to determine the most desirable operating point from the obtained Pareto front. This

Table 18
The main outcomes of the 4E analysis in terms of the proposed quad-generation system.

Parameters	Value
LNG energy inlet (kW)	25,017
LNG exergy inlet (kW)	26,070
LNG LHV (kJ/kg)	50,030
Hydrogen rate (kg/h)	14.11
Net power out (kW)	12,160
Heating power load (kW)	803
Cooling capacity (kW)	401
Syngas generated LHV (kJ/kg)	31,750
Gas turbine power out (kW)	12,760
Steam cycle turbine power out (kW)	743
Kalina cycle turbine power out (kW)	6976
Steam cycle vapor generator heat load (kW)	3088
K-100 power in (kW)	3088
Kalina cycle vapor generator heat load (kW)	5620
LNG rate (kg/s)	0.5
E-104 heat load (kW)	7120
E-101 heat load (kW)	1411
Methane conversion (%)	30.48
System energy efficiency (%)	55.29
System exergy efficiency (%)	48.99
System electricity efficiency (%)	48.59
Primary energy saving ratio (%)	34.43
Specific CO_2 emission (kg_{CO2}/kWh)	0.3537
Sustainability index (−)	1.96
Exergo-environmental impact improvement (−)	1.04
Total investment cost rate ($/h)	138.164
Fuel cost rate ($/h)	450.311
Total cost rate ($/h)	588.475
Total unit cost of product ($/GJ)	12.798
$CAPEX_{annual}$ ($)	3,627,384
OPEX ($)	32,680,540
Total annual cost ($)	36,307,924
Levelized cost of energy ($/kWh)	0.3525
Profit (M$)	21.68
Dynamic payback period (year)	3.34
Internal return rate (−)	0.26

method evaluates each solution by calculating its Euclidean distance from an ideal point, assuming equal weighting for all objectives, and selects the solution with the minimum distance as the optimal compromise solution [92].

4. Results and discussion

4.1. Pinch-point analysis and T-Q diagrams

To quantitatively evaluate the thermal integration performance, Table 12 presents the thermodynamic analysis of the heat-exchanger network, identifying E-102 and E-104 as the primary thermal drivers which manage the highest heat duties at 8534.96 kW and 7120.18 kW, respectively. High heat recovery efficiency is achieved in units E-103 and E-107, where minimum approach temperatures are minimized to 3.63°C and 6.38°C. In contrast, E-104 operates under extreme thermal gradients with a logarithmic mean temperature difference (LMTD) of 623.44°C. The distribution of pinch temperatures, spanning from 5°C in E-100 to 1314.86°C in E-104, establishes the thermodynamic boundaries and confirms the effective thermal coupling of streams across the process's operational spectrum.

The composite curves in Fig. 5 illustrate the heat transfer behavior and thermal integration within the proposed system, where the red lines represent the hot composite streams (heat sources) and the blue lines denote the cold composite streams (heat sinks). The global profile in Fig. 5(a) depicts the overall enthalpy-temperature relationship, showing the total heat integration potential and the thermal driving forces across the cycle. The individual diagrams in Fig. 5(b) provide a detailed analysis of the heat exchange localized within components E-101 through E-107; notably, E-103 exhibits a plateau indicating phase-change behavior, while units like E-104 show large temperature gaps consistent with high-grade heat transfer. These profiles confirm the thermodynamic feasibility of the network by demonstrating that the hot and cold streams maintain the required temperature approach without crossover, thereby validating the pinch-point analysis.

Fig. 6 provides a structural visualization of the heat exchanger network, mapping the precise thermal coupling between the hot streams (red) and cold streams (blue). This diagram details the sequential heat recovery across components E-100 through E-109, showcasing the energy cascade from high-temperature sources—starting with E-104 at 1314.9°C —down to the lower-temperature sinks. By defining the intersection points and thermal loads for each exchanger, the grid validates the physical configuration of the system's integration, ensuring that the enthalpy exchange between process streams is optimized according to the established pinch-point constraints.

Building on the thermodynamic insights from the pinch analysis, the

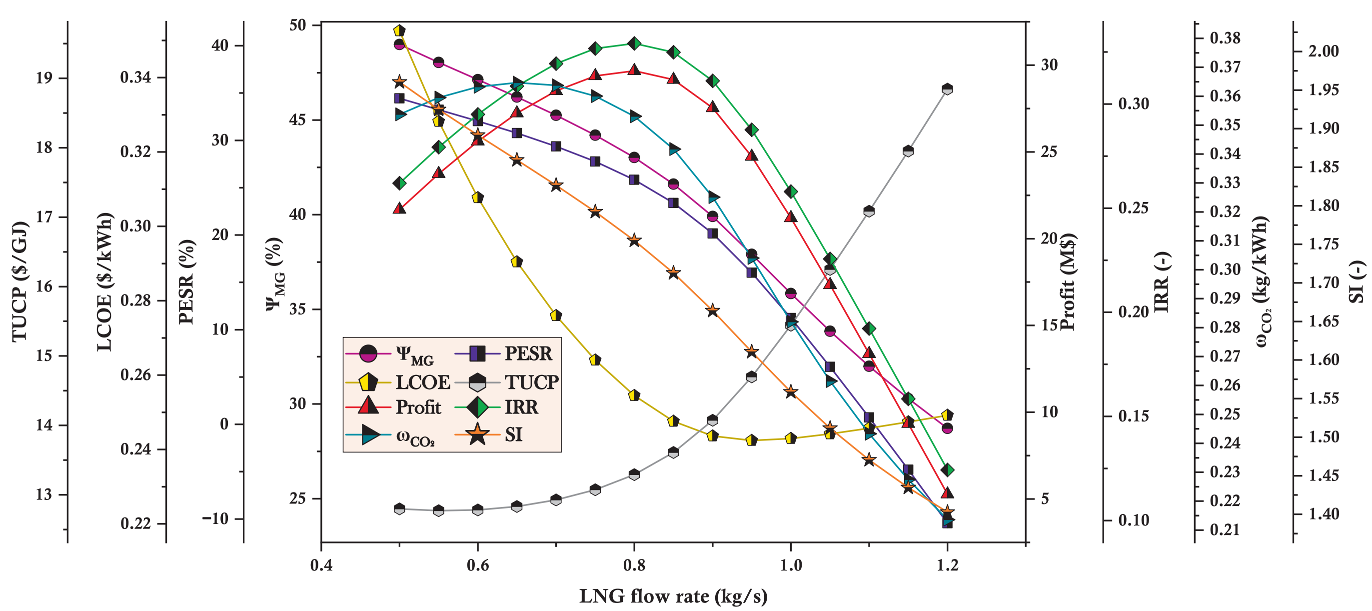

Fig. 12. The system's ψ_{MG}, PESR, LCOE, TUCP, Profit, IRR, ω_{CO_2}, and SI at higher LNG flow rate operating conditions.

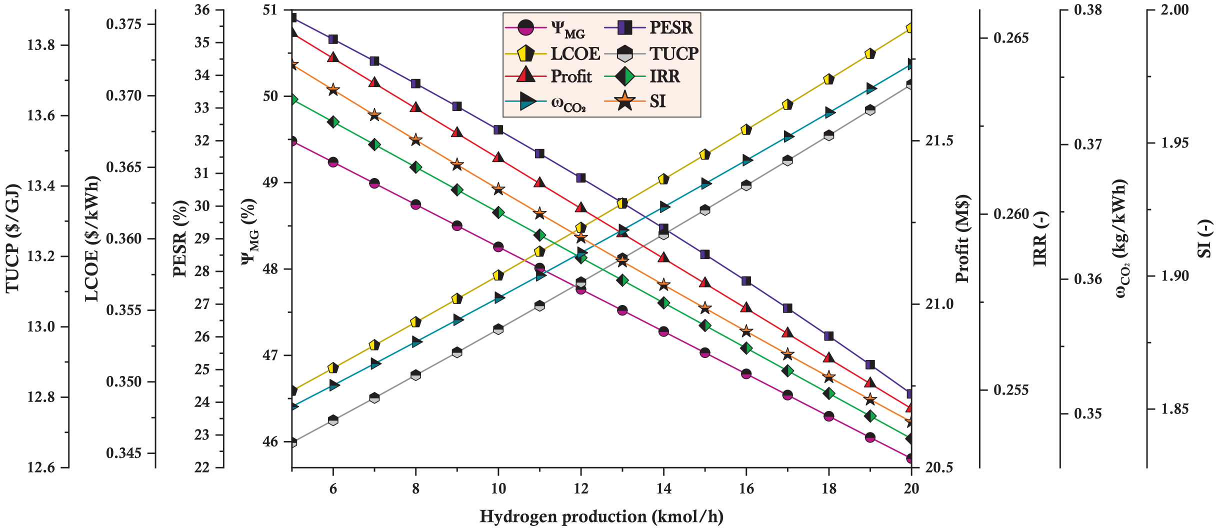

Fig. 13. The system's ψ_{MG}, PESR, LCOE, TUCP, Profit, IRR, ω_{CO_2}, and SI at higher hydrogen production rate operating conditions.

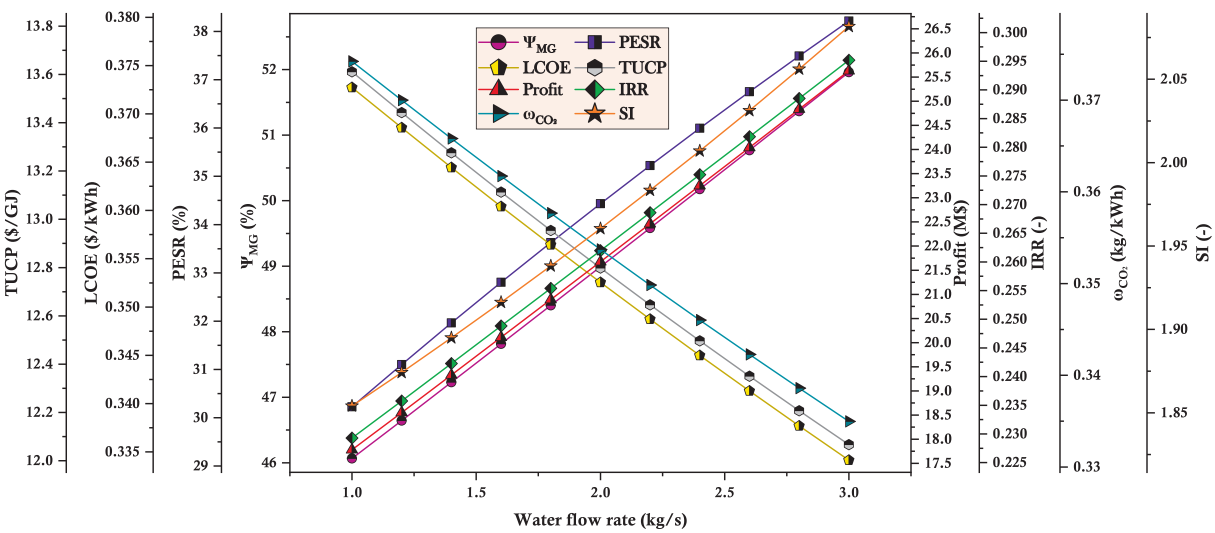

Fig. 14. The system's ψ_{MG}, PESR, LCOE, TUCP, Profit, IRR, ω_{CO_2}, and SI at higher water flow rate operating conditions.

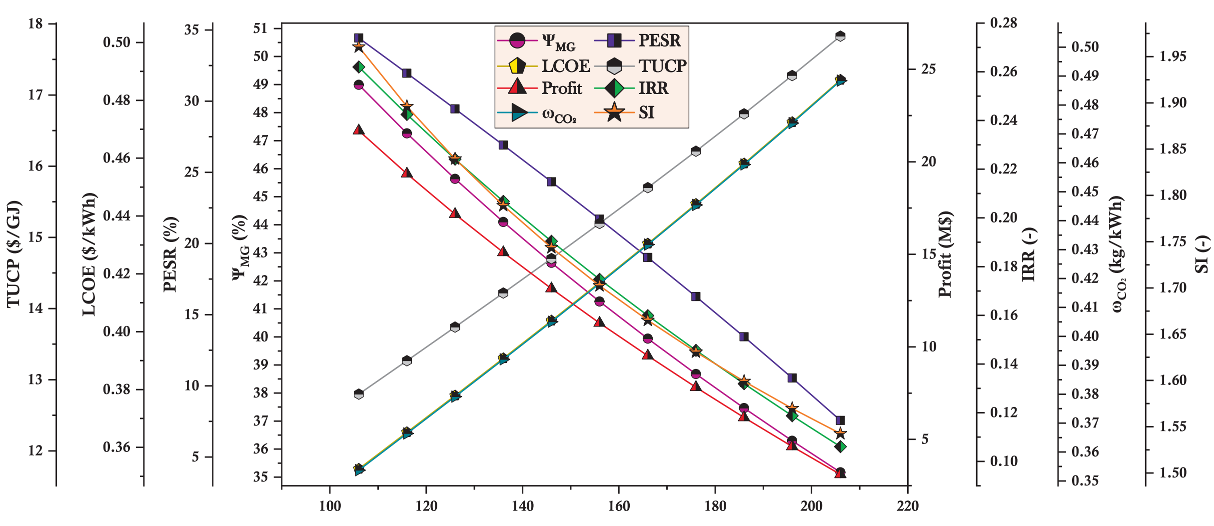

Fig. 15. The system's ψ_{MG}, PESR, LCOE, TUCP, Profit, IRR, ω_{CO_2}, and SI at higher stream 21 pressure operating conditions.

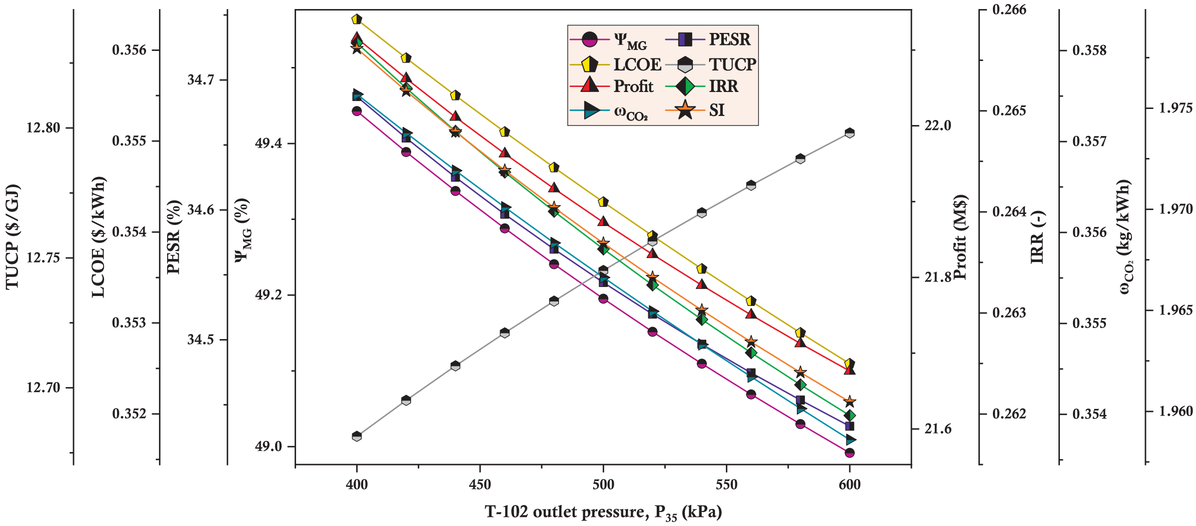

Fig. 16. The system's ψ_{MG}, PESR, LCOE, TUCP, Profit, IRR, ω_{CO_2}, and SI at higher stream 35 pressure operating conditions.

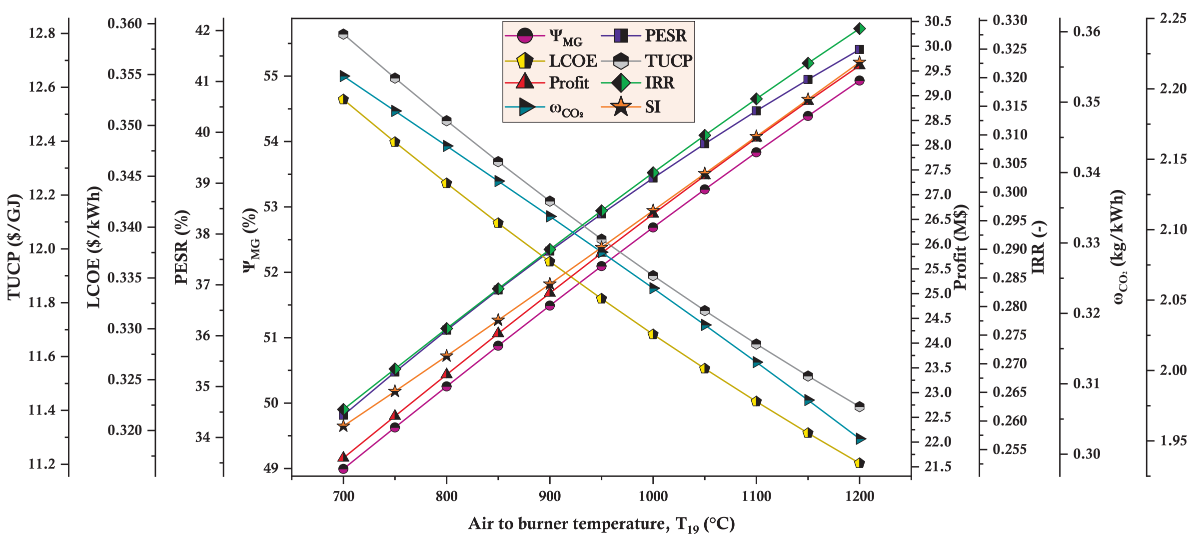

Fig. 17. The system's ψ_{MG}, PESR, LCOE, TUCP, Profit, IRR, ω_{CO_2}, and SI at higher stream 19 temperature operating conditions.

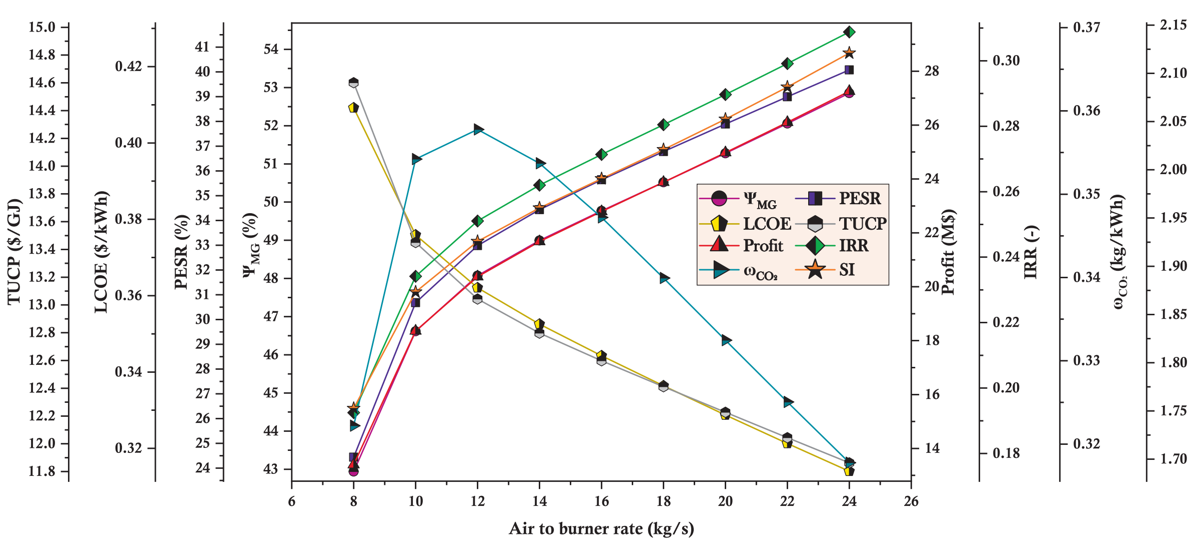

Fig. 18. The system's ψ_{MG}, PESR, LCOE, TUCP, Profit, IRR, ω_{CO_2}, and SI at higher air-to-burner flow rate operating conditions.

Table 19
Predictive accuracy of the MLP surrogate model for all target outputs based on the evaluated metrics for train-test datasets.

Target	Sample	RMSE	MAE	R^2	MAPE
System energy efficiency (%)	Train	0.405	0.043	0.992	0.086
System exergy efficiency (%)	Train	0.366	0.039	0.991	0.089
Net power out (kW)	Train	94.511	10.057	0.995	0.092
Levelized cost of energy ($/kWh)	Train	0.004	0.001	0.988	0.155
Total unit cost of product ($/GJ)	Train	0.133	0.012	0.985	0.087
Profit (M$)	Train	0.491	0.045	0.989	0.591
Internal return rate (−)	Train	0.004	0.001	0.988	0.297
Specific CO_2 emission	Train	0.004	0.001	0.986	0.157
Sustainability index (−)	Train	0.011	0.002	0.994	0.086
Exergo-environmental impact improvement (−)	Train	0.021	0.002	0.988	0.181
Target		**RMSE**	**MAE**	$\mathbf{R^2}$	**MAPE**
System energy efficiency (%)	Test	0.162	0.077	0.999	0.155
System exergy efficiency (%)	Test	0.151	0.070	0.999	0.159
Net power out (kW)	Test	41.309	18.861	0.999	0.156
Levelized cost of energy ($/kWh)	Test	0.001	0.001	0.998	0.193
Total unit cost of product ($/GJ)	Test	0.045	0.020	0.999	0.143
Profit (M$)	Test	0.203	0.081	0.998	0.516
Internal return rate (−)	Test	0.002	0.001	0.998	0.373
Specific CO_2 emission	Test	0.001	0.001	0.998	0.205
Sustainability index (−)	Test	0.004	0.002	0.999	0.124
Exergo-environmental impact improvement (−)	Test	0.009	0.004	0.998	0.287

overall 4E performance of the system is evaluated next.

4.2. 4E analysis outcomes

4.2.1. Exergy and energy outcome

The system's overall exergy destruction, as determined by an analysis of the energy-related parameters in Table 13, is equal to 12,442 kW, which represents the amount of lost input exergy as a result of irreversibility and inefficiencies across different components. Fig. 7(a) depicts each system component's contribution to the overall exergy destruction, along with the amount of exergy destroyed by each component. This figure draws attention to the fact that a considerable amount of the system overall exergy losses is owing to specific parts, including the burner with the contribution of 39.2%, and heat exchangers of E-102, and E-104 with contributions of 19% and 11.4%. Given the high irreversibility of combustion processes, the burner stands out as the primary source of the destructed exergy in the system with value of 4876. Additionally, large temperature differentials and thermal inefficiencies cause significant destruction of exergy approximately 2,359 kW and 1,415 kW in heat exchangers such as E-102 and E-104. In contrast, a large number of other parts, such as a number of pumps and vessels, exhibit comparatively low exergy destruction, suggesting effective operation. The main areas where thermodynamic advancements could be focused to increase overall system efficiency and lower exergy waste are improvements in the components operation with the highest losses.

Given that the burner is responsible for the largest share of exergy destruction (39.2%, corresponding to 4876 kW), this high contribution is mainly attributed to the intrinsic irreversibility of the combustion process, including high-temperature chemical reactions, fuel–air mixing, and large temperature gradients between the reacting gases and the surroundings. In the present system, the use of hydrogen-rich syngas and elevated combustion temperatures further intensifies entropy generation within the burner. Nevertheless, several strategies can mitigate this exergy destruction. These include optimizing the air-to-fuel ratio to approach more ideal combustion conditions, improving air preheating through the existing heat recovery network (e.g., heat exchanger E–104) to reduce temperature gradients, and enhancing the recovery of thermal energy from exhaust gases. Implementing such measures can decrease entropy generation in the combustion chamber and consequently improve the overall thermodynamic performance of the system.

Fig. 7(b) contrasts the exergy efficiency of different system components, emphasizing that the PEME for hydrogen generation and E-100 for cooling generation have comparatively lower efficiencies around 50%. This lower exergy efficiencies of components are due to their higher contribution in destruction of system exergy.

4.2.2. Economic outcome

Economically, the detailed costs and associated hourly cost rates in terms of different components of the presented system are listed in Table 14, where the overall equipment cost amounts to 9,528,880 $. Fig. 8 depicts the contribution of component in the overall cost, highlighting the high share of turbines in the overall cost and their substantial share of the capital investment. Among the turbines, the GT-100 is the most expensive unit, accounting for the share of 65.2% and cost of 3,296,411 $. The K-100 compressor, with a cost of 1,151,402 $, is another major cost contributor.

According to Table 15, the CAPEX estimation utilizes the total purchased equipment cost (TPEC) as the baseline (9528880 $), applying specific factors for direct and indirect costs. The fixed capital investment (FCI) is calculated at 30,968,860 $ after accounting for installation, instrumentation, and contingency fees. By incorporating a 15% working capital, the total capital investment (TCI) for the integrated system is estimated at 35,614,189 $, providing a transparent and standardized investment profile for the project.

Plus, based on Table 16, the OPEX analysis reveals a total product cost (TPC) of 32,680,540 $ per year. The breakdown highlights that operating labor and plant overhead represent the most significant operational expenditures. Unlike simplified models, this assessment accounts for variable factors such as raw materials (LNG), maintenance supplies (15% of repairs), and general expenses (marketing and R&D), ensuring the economic results reflect the complexities of a large-scale integrated energy system.

Fig. 9 compares the profit of the system under various product prices—including electricity (Fig. 9(a)), hydrogen (Fig. 9(b)), cooling (Fig. 9(c)), heating (Fig. 9(d)) and LNG fuel costs (Fig. 9(e)). As shown in Eq. (59), the fuel costs have an inverse relationship with system profitability, while product prices have a direct impact on system profit. Higher product prices result higher annual income which increases profitability and shortens the dynamic payback period (DPP). On the other hand, when the cost of LNG fuel rises, the system's profitability decreases and the DPP lengthens. According to the presented figures, the system's profit is greatly increased and the DPP is shortened by raising the selling prices of electricity, hydrogen, cooling, and heating to about 0.12 $/kWh, 8 $/kg, 0.16 $/kWh, 0.09 $/kWh, respectively. On the other hand, when the price of LNG fuel is raised from 3 $/kg to 9 $/kg, the profitability drops from 35 M$ to 5 M$, and the DPP lengthens from 2.69 to over 20 years.

To further assess the economic sensitivity of the system, Fig. 10 illustrates that the economic performance of the system is most strongly influenced by the electricity price compared with the other selling-buying price parameters. An increase in the electricity selling price leads to a noticeable reduction in the DPP and a substantial increase in $Profit_{20}$, whereas a decrease in electricity price significantly worsens both indicators. In contrast, variations in heating, cooling, and hydrogen prices have much smaller effects on the DPP and only moderate impacts on $Profit_{20}$. Overall, the results indicate that the project profitability is primarily governed by electricity market conditions, while the other utility price parameters play a secondary economic role.

Moreover, the sensitivity results in Fig. 11 show that TUCP is most strongly affected by fuel cost, with the baseline value of 12.798 $/GJ varying between 10.35 and 15.25 $/GJ for a ± 25% change in fuel price. The interest rate (q) and system lifetime (n) costs also influence TUCP,

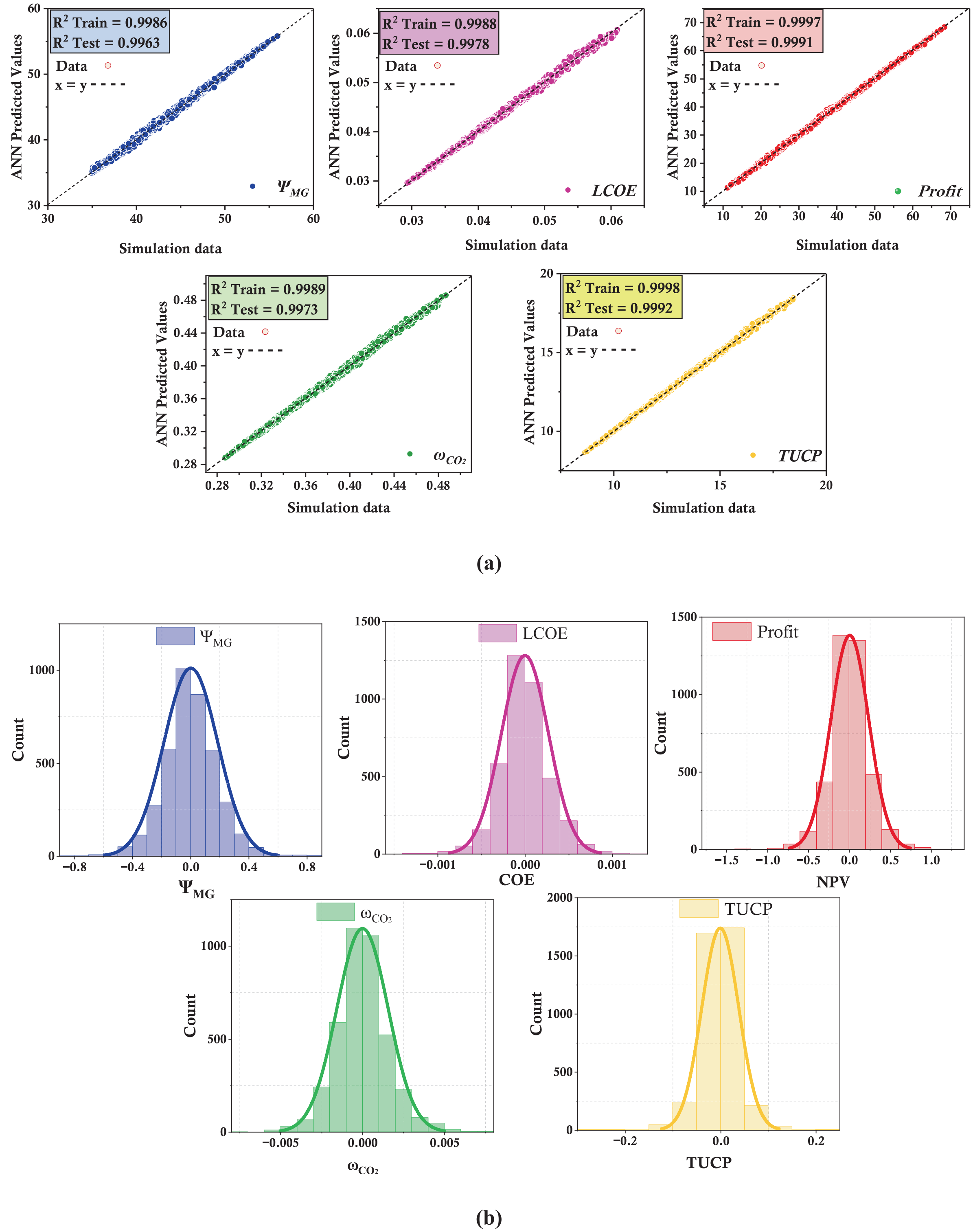

Fig. 19. **(a)** Agreement between the actual values and predicted ones, and **(b)** residual distribution in terms of ψ_{MG}, LCOE, Profit, ω_{CO_2}, TUCP predictions using MLP model.

but with much smaller magnitude. The effect of component cost escalation is also comparatively smaller. This confirms that LNG price volatility is the dominant economic uncertainty in the suggested MG system.

4.2.3. *Environmental outcome*

Form environmental perspective, based on Eq. (46), the specific CO_2 emission (ω_{CO_2}) of the system is estimated at 0.3537 kg_{CO2}/kWh, and the exergo-environmental calculation registers a sustainability index of 1.96, and an exergo-environmental impact improvement factor of 1.04. Furthermore, based on the simulation results of the LCA in Table 17, the total GWP for the system is determined to be 11,807 $kg_{CO2\text{-}eq}$/h. This correlates to a specific environmental impact of 0.8536 $kg_{CO2\text{-}eq}$/kWh of produced energy. The inclusion of utility-related impacts ensures that

Table 20
Optimal design parameters and performance indicators obtained from the multi–objective optimization of the proposed system using the MLP–Cuckoo Search algorithm for three optimization scenarios.

Design Parameters	Unit	Base	Scenario 1: ψ_{MG}-LCOE-ω_{CO_2}	Scenario 2: ψ_{MG}-TUCP-Profit	Scenario 3: ψ_{MG}- Profit $-\omega_{CO_2}$
LNG flow rate	kg/s	0.5	1.05	0.51	1.06
Hydrogen production rate	kmol/h	7	5.00	7.10	5.08
Water flow rate (steam to reformer rate)	kg/s	2	1.95	1.91	1.93
GT-100 outlet pressure, P_{21}	kPa	106	164.73	154.38	114.06
T-102 outlet pressure, P_{35}	kPa	600	572	402.79	518.58
Air-to-burner temperature, T_{19}	°C	700	777	1198	752
Air-to-burner flow rate	kg/s	14	23.92	13.92	13.90
Performance criteria					
$\dot{W}_{net}^{MG}$	kW	12,160	18,153	14,017	18,108
η_{MG}	%	55.29	56.99	63.34	52.22
ψ_{MG}	%	48.99	50.46	56.50	46.27
ω_{CO_2}	kg_{CO2}/kWh	0.353	0.270	0.297	0.260
SI	–	1.96	1.90	2.26	1.80
EII	–	1.04	1.27	0.75	1.34
TUCP	$/GJ	12.79	12.19	10.84	13.10
LCOE	$/kWh	0.352	0.237	0.307	0.237
Profit	M$	21.68	11.52	31.01	21.42
IRR	–	0.26	0.17	0.33	0.25

the assessment reflects the total operational footprint of the conceptual design, rather than just localized combustion emissions.

To further clarify the environmental accounting, the contribution of the main CO_2 emission sources has been quantified. The gas stream leaving the reformer (after water separation) contains 1389.07 kg/h CO_2, whereas the total CO_2 flow rate in the final stack gas is 4892.36 kg/h. Therefore, approximately 28.4% of the total CO_2 emissions are directly associated with the reforming section, while the remaining 71.6% arise from downstream combustion processes, mainly due to the oxidation of unconverted methane and other combustible species in the gas turbine combustor.

Collectively, the results in Table 18 provide the integrated 4E performance of the proposed system. The steady–state results indicate that the system produces 14.11 kg/h hydrogen, 12160 kW net electrical power, 803 kW useful heating, and 401 kW cooling capacity.

Within the SMR section, heat supplied through heat exchangers E–101 and E–102 raises the reformer temperature to approximately 522.3 °C, resulting in a methane conversion of 30.48%. It should be noted that this conversion level is a consequence of the selected operating strategy rather than a limitation of the reforming model. The reformer is integrated as an intermediate hydrogen–rich syngas generator within the presented system, and it is not optimized for maximum methane conversion. Due to the moderate operating temperature, controlled steam–to–carbon ratio, and limited recoverable heat within the integrated configuration, only a portion of methane is converted to H_2 and CO. The remaining unconverted methane is subsequently utilized as a combustible component in the gas turbine combustor, thereby contributing to downstream power production. Hence, the reported 30.48% conversion reflects a thermodynamic trade–off between hydrogen production, preservation of chemical energy for power generation, and overall system efficiency optimization.

Accordingly, the total energy and exergy efficiencies of the proposed system are calculated as 55.29% and 48.99%, respectively, with a primary energy saving ratio of 34.43%. Environmentally, the system demonstrates a specific CO_2 emission of 0.3537 kg_{CO2}/kWh, alongside a sustainability index of 1.96 and an exergo-environmental impact improvement factor of 1.04. Economically, the system achieves a total unit cost of product (TUCP) of 12.798 $/GJ and a competitive levelized cost of energy (LCOE) at 0.3525 $/kWh, resulting in a projected Profit of 21.68 M$ with a dynamic payback period (DPP) of 3.34 years. Overall, these results demonstrate the technical feasibility, environmental competitiveness, and economic viability of the proposed integrated quad-generation system.

4.3. Parametric study outcomes

To further understand system behavior, a parametric study is conducted. According to Fig. 12, the system at higher LNG flow rates at stream 1 reveals higher power generation and economic benefits but at a wastage of exergy efficiency and environmental sustainability. As the flow rate increases from 0.5 to 0.8 kg/s, the system exhibits decline in ψ_{MG} from 48.9% to 43%, due to higher irreversibility of E-100 at elevated flow rates. On the other hand, it results in enhancing electricity production capacity, leading to LCOE lowering from 0.35 to 0.25 $/kWh and TUCP increasing to around 13.5 $/GJ. Although PESR drops from 34.4% to 25.8% due to increased LNG rate as main heat source, the system Profit is improved from 22 to 30 M$, and IRR is increased to 0.33 due to lower unit costs. The environmental impact indicators show mixed behavior so that increasing the LNG rate up to 0.65 kg/s indicates higher ω_{CO_2} of 0.37 kg_{CO2}/kWh, while beyond this value ω_{CO_2} is declined. The higher irreversibility results in SI declining from 1.96 to 1.75.

Fig. 13 shows that the system with higher production of hydrogen rate at stream 45 results in lower power generation and efficiencies, which rises unit costs and environmental consequences. As the flow rate of hydrogen changes between 5 and 20 kmol/h, ψ_{MG} decreases to 45.8% from 49.5% because of a lower performance and a great irreversibility in the operation of PEME. At the same time, the decline in net electricity generation increases LCOE to an increased rate of 0.375 $/kWh and TUCP of 13.6 $/GJ. PESR decreases in response to a reduction in energy efficiency at high production levels to 24.2%. Economically, the system suffers from a loss in its Profit from 21.6 to 20.6 M$ and in IRR to 0.25 because of less annual income through power production. Moreover, the system footprint rises with a low overall energy output, increasing ω_{CO_2} from 0.35 to 0.37 kg_{CO2}/kWh that provides a minor decrease in SI from 1.96 to 1.85 due to higher destroyed exergy.

Fig. 14 shows that, by increasing water flow rates at stream 8, power output and efficiencies are increased while unit costs and environmental impacts are reduced. When the water flow rate is increased from 1 to 3 kg/s, ψ_{MG} in the system has improved to 51.9% compared to 46.0%, because the increased input steam into reformer enhances this unit efficiency and lower irreversibility. Moreover, an increase in the capacity of electricity production causes a reduction of LCOE to 0.334 $/kWh, and TUCP to 12.1 $/GJ. PESR rises up to 38.2% owing to the boosted efficiency of the system. On an economic basis, the system Profit increases to 25.5 M$ due to the higher energy production. Also, the footprint reduces by lowering ω_{CO_2} from 0.37 to 0.33 kg_{CO2}/kWh. A decrease in destruction of exergy leads to an increase in SI grows to 2.08.

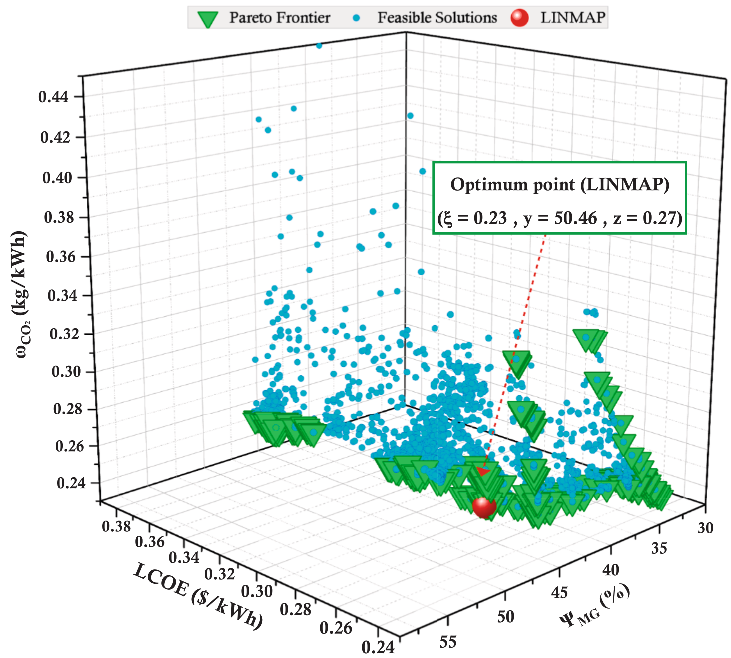

(a) Scenario 1

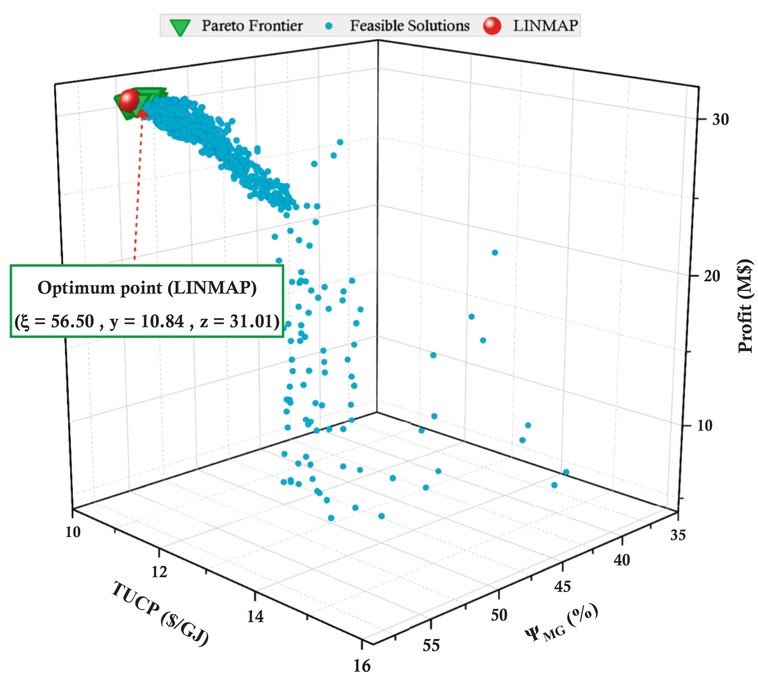

(b) Scenario 2

Fig. 20. The three-dimensional MLP–Cuckoo Search optimization in three different scenarios.

Fig. 15 demonstrates that running the system at elevated pressures of stream 21 reduces power generation and efficiencies, thus leading to higher unit costs and environmental outcomes. As the pressure increases up to from 106 to 206 kPa, the system is characterized with a drastic drop in ψ_{MG} to 35.5% from 48.5% mainly because of more irreversibility experienced in E −104. The less electricity production capacity culminates in the increment of LCOE to 0.48 $/kWh and TUCP to 17.5 $/GJ. The increased inefficiency leads to PESR reduction from 34.4 to 7%. Consequently, there is a sharp decline in Profit by of 22 to 3 M$ owing to the less generation of energy. In addition, the ω_{CO_2} indicator goes up from 0.36 to 0.49 kg_{CO2}/kWh bringing more environmental effects, while the increase in destruction of exergy results in the reduction of SI to 1.54.

Fig. 16 indicates that higher pressure at stream 35 contributes to slight lowering power generation with significant enhancement in heating capacity, leading to enhancement in energy-based metrics and

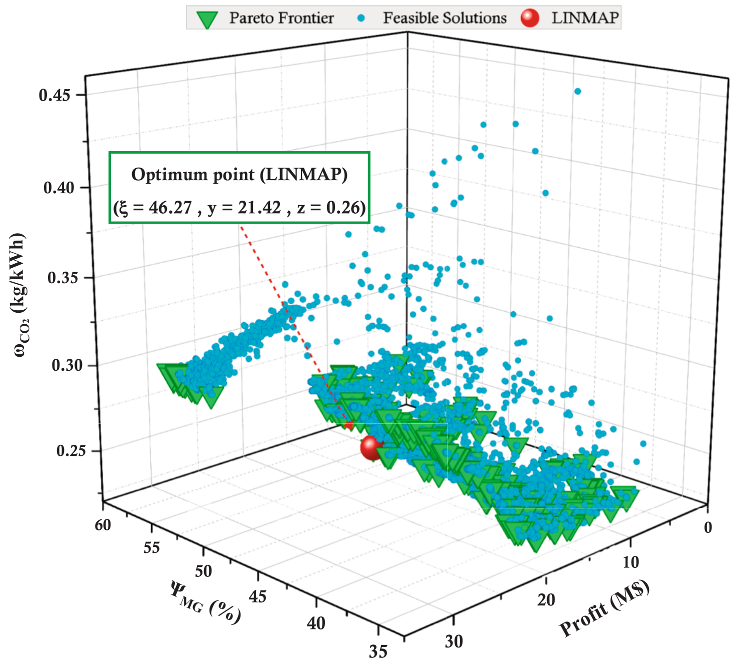

(c) Scenario 3

Fig. 20. (*continued*).

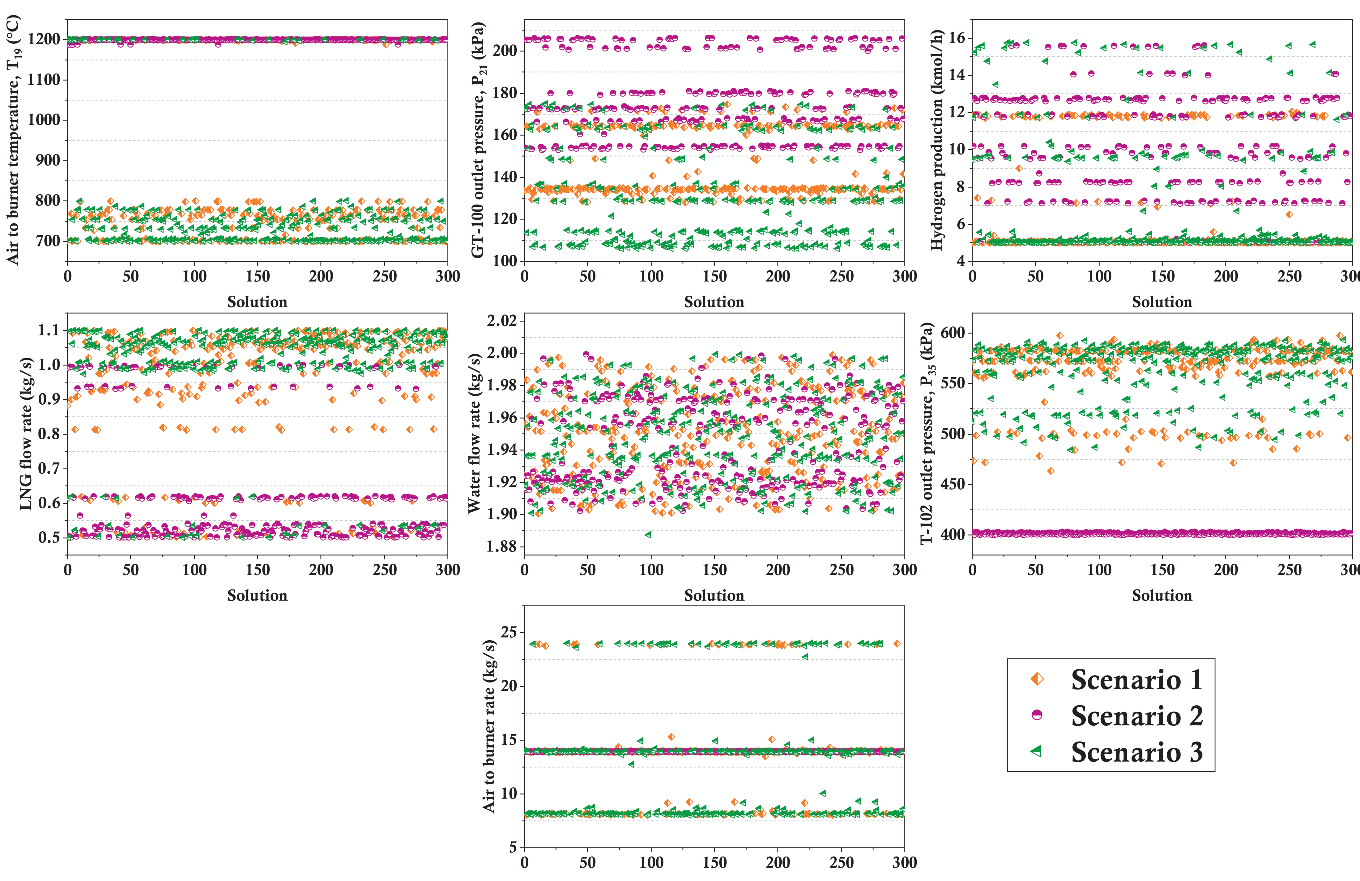

Fig. 21. The design variable distribution for Pareto front solutions obtained by Cuckoo Search optimization.

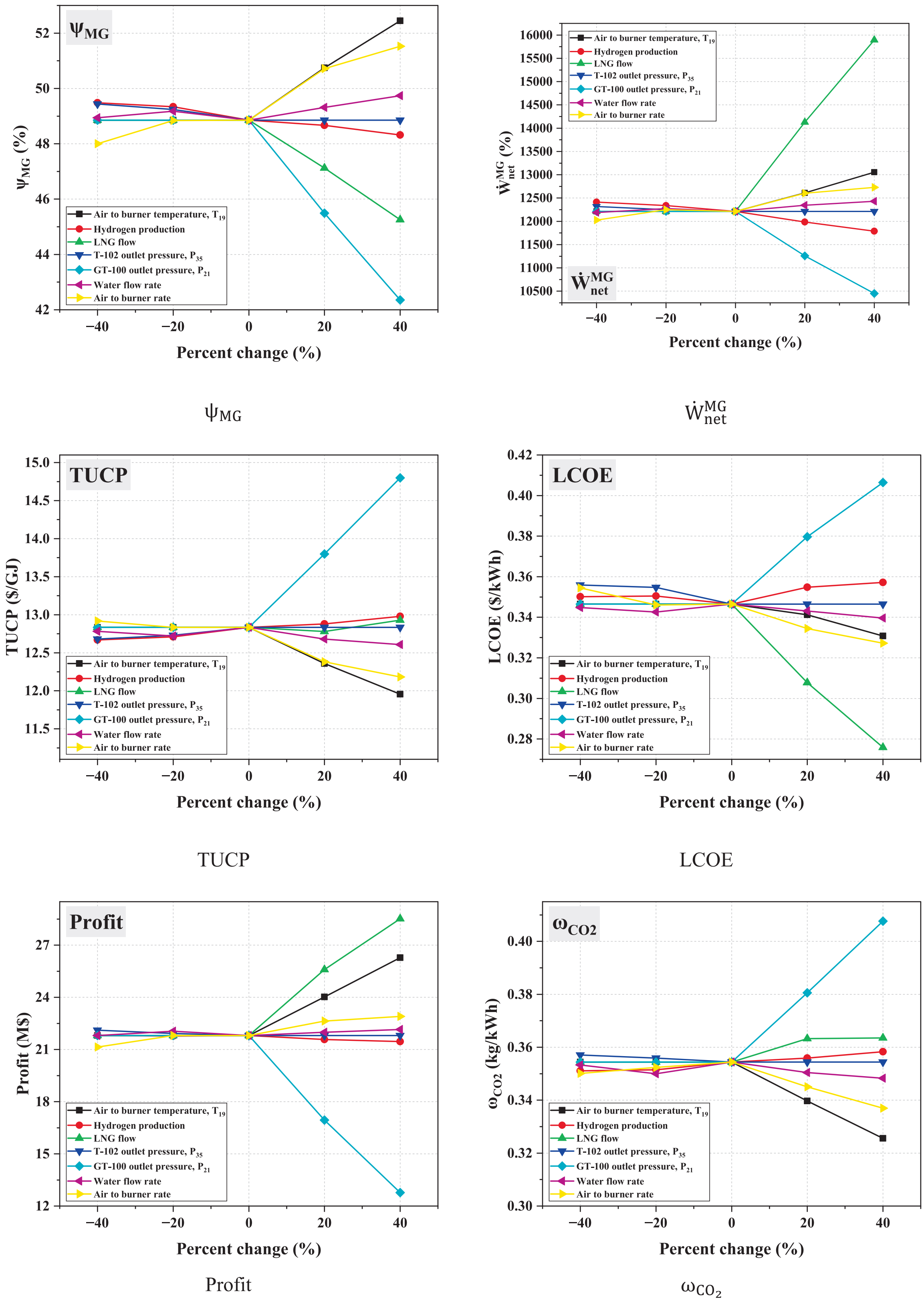

Fig. 22. One-way Monte Carlo sensitivity analysis illustrating the impact of each decision variable on the thermo-enviro-economic objective functions predicted by MLP–Cuckoo Search framework.

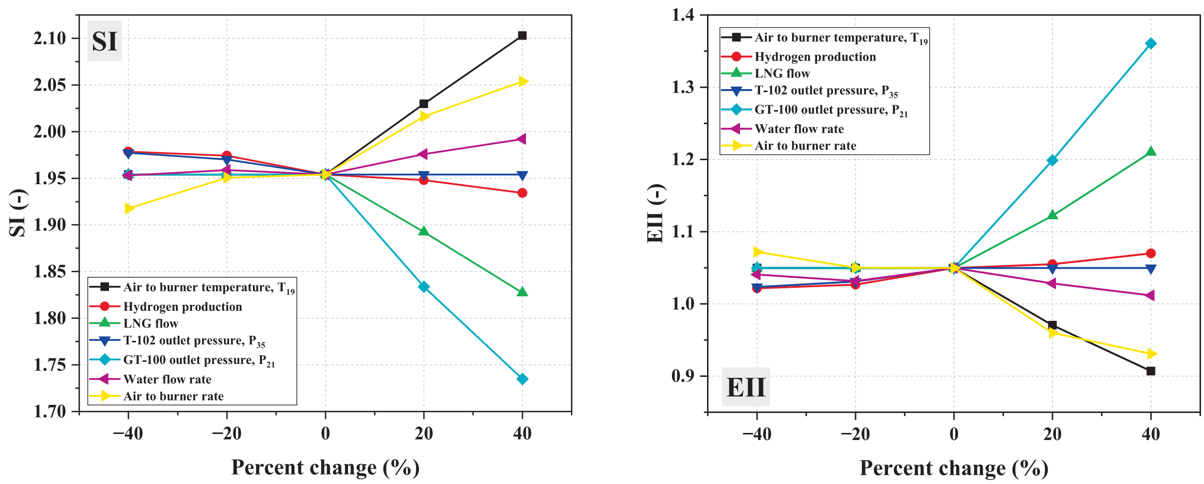

SI EII

Fig. 22. (*continued*).

degradation in exergy-based ones. As the pressure increases from 400 to 600 kPa, the system exhibits a modest decrease in ψ_{MG} from 49.4% to 49.0%, primarily due to higher irreversibility in the T-102. Conversely, the improvement in energy output leads to a slight reduction in LCOE down to 0.352 \$/kWh, while the decrease in exergy output results in an increase in TUCP to 12.79 \$/GJ. Consequently, the system's PESR drops to 34.4% and its profitability declines to 21.6 M\$ due to lower power generation and increased costs. The higher energy output causes a slight decrease of ω_{CO_2} to 0.35 kg_{CO2}/kWh, while higher destruction of exergy leads to SI deteriorating to 1.96.

Fig. 17 indicates that higher temperature at stream 19 improves the combustion efficiency in the burner, which significantly enhances the power generation, heating capacity, and economic and environmental advantages. With increasing the temperature from 700 to 1200 °C, there is an increase in the ψ_{MG} from 49% to 55% due to lesser irreversibility in the process. The achievements in the energy and exergy productions lead to a reduction in LCOE to 0.32 \$/kWh and TUCP to 11.4 \$/GJ. Moreover, the reduced irreversibility leads to the rise in PESR up to 41.6% from lower value of 34.4%. Consequently, the Profit of the system increases considerably up to 29.8 M\$, and ω_{CO_2} shows a reduction from 0.33 to 0.26 kg_{CO2}/kWh by an increase in the system outputs. Additionally, the decrease in exergy destruction leads to an enhancement in SI, which reaches a value of 2.22.

According to Fig. 18, the system at higher air–to–burner flow rates exhibits improved exergo-enviro-economic performance but at the expense of unit cost indicators. As the air–to–burner flow rate rises from 8 to 24 kg/s, the system shows an increase in ψ_{MG} from about 43% to nearly 52%, mainly due to the increase in irreversibilities within the combustion and heat–transfer units at elevated air flow rates. In contrast, the higher air supply enhances the power generation capability and thus strengthens the economic performance; LCOE decreases from roughly 0.41 to 0.32 \$/kWh, while TUCP decreases from about 14.5 to 13 \$/GJ. The system Profit rises from nearly 14 to 27 M\$, while IRR grows from around 0.19 to 0.31, confirming the economic attractiveness of operating at higher air–to–burner flow rates. However, the exergo–sustainability indicators exhibit the opposite tendency. PESR increases to 40% with increasing air–to–burner flow rate, while ω_{CO_2} first increases up to 0.36 kg_{CO2}/kWh (at air–to–burner flow rate of 12 kg/s) then decreases to 0.315 kg_{CO2}/kWh. Consequently, SI slightly increases from about 1.75 to 2.12, reflecting the trade–off between exergo-enviro-economic performances at higher air–to–burner flow rates.

4.4. MLP–Cuckoo Search optimization outcomes

Beyond parametric trends, multi-variable optimization is performed using the MLP–Cuckoo Search framework. The predictive performance of the trained MLP model is evaluated using several statistical metrics including RMSE, MAE, MAPE, and R^2. As presented in Table 19, the model exhibits excellent generalization performance, with test-set R^2 values above 0.998 for all outputs. The corresponding error metrics are consistently low. For thermodynamic indicators, RMSE/MAE values are 0.162/0.077 for energy efficiency and 0.151/0.070 for exergy efficiency. Net power output is predicted with an RMSE of 41.309 kW and an MAE of 18.861 kW. Economic outputs also show high precision, including 0.001/0.001 for LCOE, 0.045/0.020 for TUCP, 0.203/0.081 M\$ for Profit, and 0.002/0.001 for IRR. Environmental indicators are similarly accurate, with RMSE/MAE values of 0.001/0.001 (ω_{CO_2}), 0.004/0.002 (SI), and 0.009/0.004 (EII). These results confirm the robustness of the developed surrogate model.

In line with this table, the performance analysis of the MLP modeling in prediction of critical performance metrics, namely ψ_{MG}, LCOE, Profit, ω_{CO_2}, and TUCP, are shown in Fig. 19. Based on Fig. 19(a), it can be seen that the MLP model in the testing stage has outstanding forecasting power with incredibly high coefficients of determination (R^2), which are equal to 0.9963 for ψ_{MG}, 0.9978 for LCOE, 0.9991 for Profit, 0.9973 for ω_{CO_2}, and 0.9992 for TUCP. This high R^2 values signify a very good fit of the model to describe the complexity of the nonlinear forms of relations that existed between different operational and economic parameters within the suggested system.

Furthermore, analysis of the MLP error distribution plots in Fig. 19 (b) shows a general trend with low error between the actual and the predicted values of performance parameters. The analysis of residual errors shows that most of predictions errors with very little dispersion are set in narrow range approximately [-0.8, +0.8] for ψ_{MG}, [-0.001, +0.001] for LCOE, [-1.0, +1.0] for Profit, [-0.006, +0.006] for ω_{CO_2}, and [-0.2, +0.2] for TUCP. This figure indicates that most of errors are more concentrated around zero, especially in Profit parameter, which represents that there is no bias and a very good agreement. This high consistency and low error spread attests to the strength of the MLP model in mapping out complex and non-linear relationships and guarantees great certainty of its forecasting potential for performance evaluation and optimization of advanced energy systems.

The optimization results in Table 20 indicate different trade–offs among thermodynamic, economic, and environmental objectives. Scenario 1 significantly reduces LCOE (0.237 \$/kWh) and ω_{CO_2} (0.270

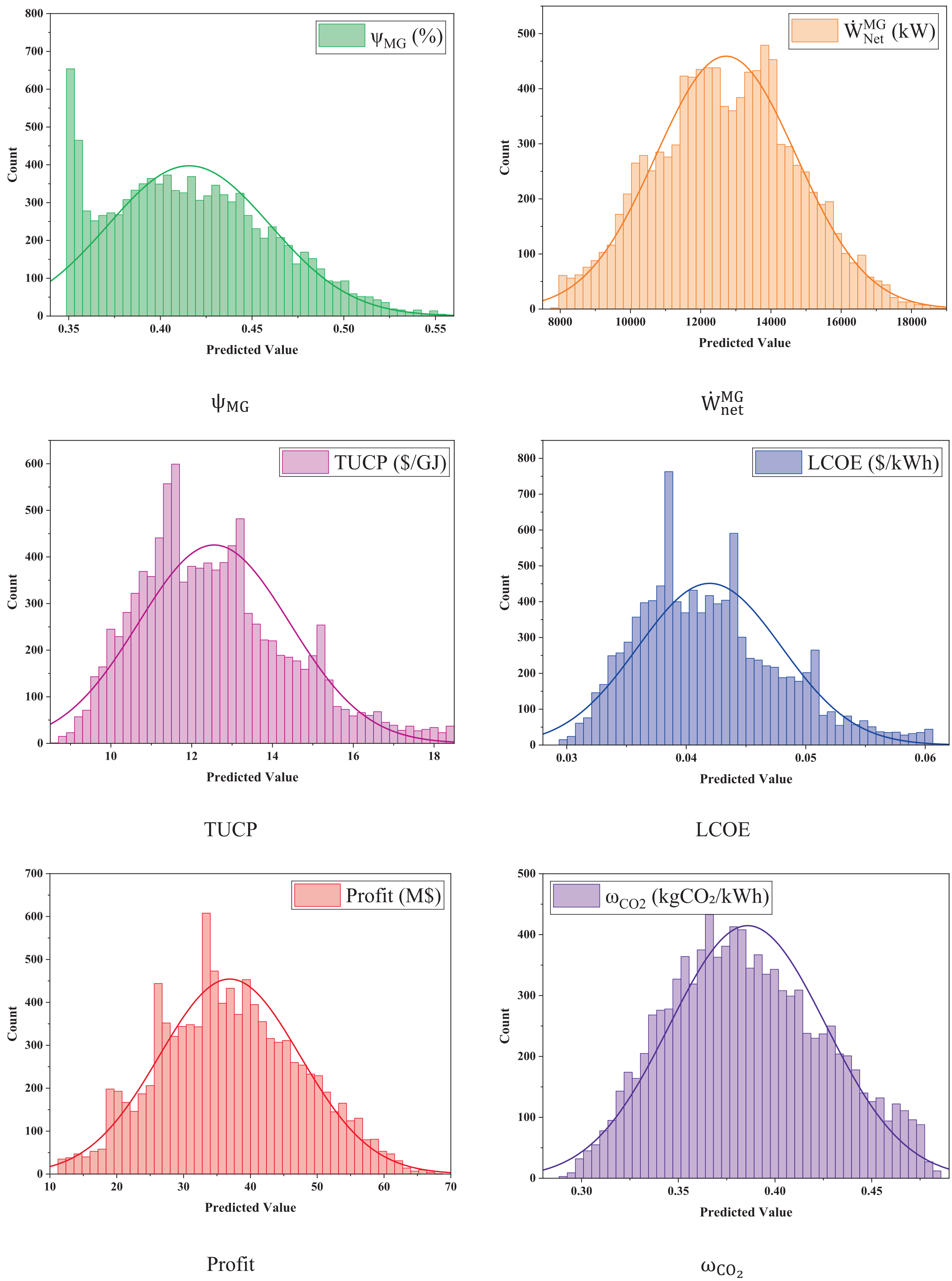

Fig. 23. Probability distributions of the objective functions obtained from Monte Carlo uncertainty propagation, showing the variability and clustering of system performance across the decision–variable design space.

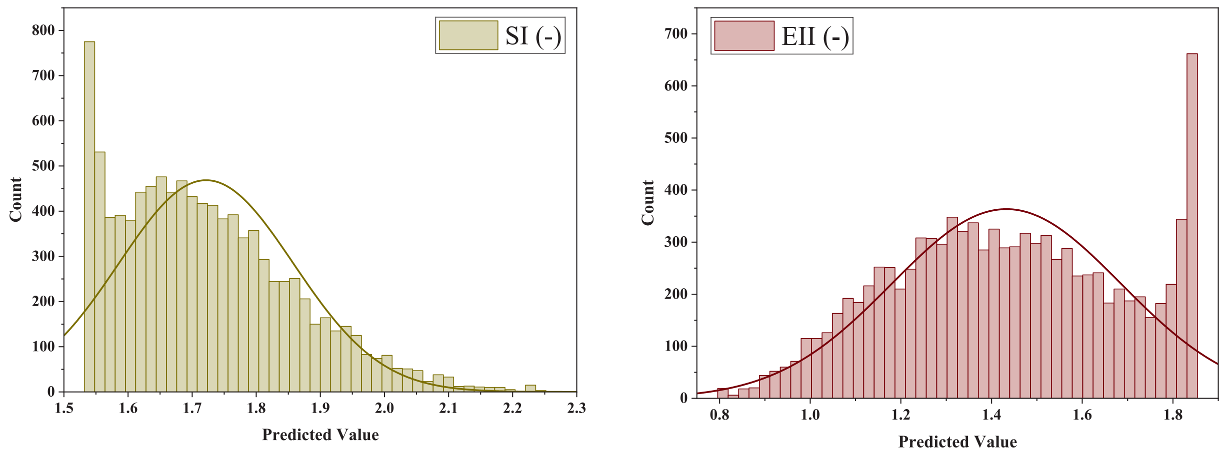

SI EII

Fig. 23. (*continued*).

kg_{CO2}/kWh) while moderately improving exergy efficiency (50.46%). Scenario 3 provides the lowest ω_{CO_2} (0.260 kg_{CO2}/kWh) with relatively lower exergy efficiency of 46.27% and Profit of 21.42 M$. Overall, Scenario 2 represents the most favorable balance between system efficiency and economic performance with the greatest exergy efficiency of 56.50%, the lowest TUCP of 10.84 $/GJ, and the best Profit of 31.01 M$.

Fig. 20 depicts the three-dimensional MLP–Cuckoo Search optimization in three different scenarios that each one analyses the tradeoffs among the major key performance indicators. In Scenario 1 (Fig. 20(a)), the LINMAP-selected optimum point based on the MLP–Cuckoo Search optimization achieves ψ_{MG} of 50.46%, and comparatively lower LCOE of 0.23 $/kWh and ω_{CO_2} of 0.27 kg_{CO2}/kWh, satisfying the cost-effectiveness and exergo-environmental benefit of the system. On the other hand, Scenario 2 (Fig. 20 (b)) registers the highest ψ_{MG} of 56.50%, which paired with the lowest TUCP of 10.84 $/GJ and the best Profit of 31.01 M$, suggesting potential exergo-economic advantages. Scenario 3 (Fig. 20 (c)) presents ψ_{MG} at 46.27% and Profit of 21.42 M$ with the lowest ω_{CO_2} of 0.26 kg_{CO2}/kWh. This scenario-base optimization underscores the capability of the Cuckoo Search algorithm to navigate complex multi-dimensional objectives, balancing exergy performance, environmental impact, and economic returns.

Fig. 21 illustrates the distribution of seven key design variables across the Pareto front solutions obtained via Cuckoo Search optimization. The plots reveal distinct operational ranges and clustering patterns for each scenario, demonstrating how the algorithm explores the decision space to satisfy conflicting objective functions. Notably, the air–to–burner temperature (T_{19}) shows a binary preference, with solutions heavily concentrated at approximately 700 °C and 1200 °C. Hydrogen production rates display a clear preference for lower values, clustering primarily between 5 and 7 kmol/h, suggesting that lower hydrogen output is prioritized across the current configurations. LNG flow rates exhibit a broad distribution, ranging from 0.5 to 1.1 kg/s, while water flow rates remain constrained within a narrow band of 1.90 to 2.00 kg/s. Furthermore, the GT–100 outlet pressure (P_{21}) and T–102 outlet pressure (P_{35}) show significant dispersion, with P_{21} values largely distributed between 105 and 205 kPa and P_{35} between 400 and 590 kPa. Finally, the air–to–burner flow rate shows clear stratification, with solutions clustered at three distinct levels—approximately 8, 14, and 24 kg/s—reflecting the algorithm's strategic navigation of the system's performance boundaries.

4.5. Sensitivity, feature-importance, and uncertainty analyses

Following the identification of the optimal operating scenarios, a sensitivity and uncertainty analysis is performed on the MLP–Cuckoo Search optimization framework to evaluate the influence of the selected decision variables on the considered objective functions and to examine the robustness of the predicted responses. In this regard, a Monte Carlo-based one-way sensitivity analysis is conducted by perturbing each decision variable within its admissible range while monitoring the variation in the thermo-enviro-economic objective functions.

One-way sensitivity analyses in Fig. 22 show the system's thermo-enviro-economic performance is predominantly driven by the LNG flow rate, GT-100 outlet pressure (P_{21}), air-to-burner temperature (T_{19}), and air-to-burner flow rate, while remaining relatively robust against variations in the steam-to-reformer rate (water flow rate), hydrogen production, and T-102 outlet pressure (P_{35}). Specifically, while P_{21} negatively impacts ψ_{MG}, $\dot{W}_{net}^{MG}$, Profit, and SI, it significantly increases TUCP, LCOE, ω_{CO_2}, and EII. On the other hand, LNG flow rate acts as a critical economic driver, significantly enhancing $\dot{W}_{net}^{MG}$, Profit and EII, while reducing ψ_{MG}, LCOE, and SI. Consequently, the system's performance volatility is primarily concentrated in the air and fuel supply streams as well as GT-100 outlet pressure, identifying these as the key parameters for future operational optimization and control strategy development.

To further assess the robustness of the surrogate-based predictions, the uncertainty analysis shown in Fig. 23 was also carried out using Monte Carlo sampling of the selected decision variables. The obtained probability distributions prove that while the integrated system exhibits stable performance across a broad operational range, the probability distributions of the predicted outcomes demonstrate a clear gravitation toward specific performance regimes. While metrics such as $\dot{W}_{net}^{MG}$ and ω_{CO_2} follow near-normal distributions, indicators like ψ_{MG}, SI, and EII display skewed or multi-modal profiles, with high-frequency clustering at their operational bounds. Furthermore, the presence of distinct peaks in economic indicators such as TUCP and LCOE highlights that the system's performance is sensitive to particular parameter combinations, which favor specific economic clusters rather than a uniform distribution of results. Taken together, these findings underscore that the MLP–Cuckoo Search framework not only captures the nonlinear relationships between the decision variables and objective functions, but also reliably identifies robust and distinct optimal operating regions.

4.6. Quantitative benchmarking with literature

Finally, the proposed system is benchmarked against recent MG studies in the literature, as summarized in Table 21. In terms of energy

Table 21
Comparison of η_{MG}, ψ_{MG}, ω_{CO_2}, LCOE, and TUCP indicators between the proposed system and relevant literature.

Studies	Source	Configuration	η_{MG}(%)
[20]	Natural gas	SE–SMR, Ca–looping carbon capture, H_2 gas turbine, and absorption chiller	61.00
[24]	Natural gas / methanol	Gas turbine, MSR, CO_2 recondensation, desalination, and absorption chiller	53.35
[25]	Natural gas	Gas turbine, SMR thermochemical recuperator, cooling, and desalination	60.48
[28]	Biogas	Biogas steam reforming, purification, and MG system	31.51
[94]	Biomass, LNG	Hybrid biomass-LNG-based MG system combining a coffee husk combustor with LNG cold energy, electrolyzer, desalination, and organic-ammonia Rankine cycles	29.90
This study	LNG	LNG regasification, SMR, gas turbine, steam Rankine cycle, Kalina cycle, hot water boiler, and PEME	**Base: 55.29** **Opt.: 63.34**
			ψ_{MG}(%)
[25]	Natural gas	Gas turbine, SMR thermochemical recuperator, cooling, and desalination	32.55
[27]	Methanol	Reformed methanol HT–PEMFC fuel cell and absorption refrigeration (CCHP)	43.12
[28]	Biogas	Biogas steam reforming, purification, and MG system	31.14
[94]	Biomass, LNG	Hybrid biomass-LNG-based MG system combining a coffee husk combustor with LNG cold energy, electrolyzer, desalination, and organic-ammonia Rankine cycles	14.38
[95]	BFG, LNG	Gas turbine, LNG utilization, seawater desalination unit, modified Kalina cycle, and PEME	36.61
This study	LNG	LNG regasification, SMR, gas turbine, steam Rankine cycle, Kalina cycle, hot water boiler, and PEME	**Base: 48.99** **Opt.: 56.50**
			ω_{CO_2} (kg_{CO2}/kWh)
[27]	Methanol	Reformed methanol HT–PEMFC fuel cell and absorption refrigeration (CCHP)	0.510
[94]	Biomass, LNG	Hybrid biomass-LNG-based MG system combining a coffee husk combustor with LNG cold energy, electrolyzer, desalination, and organic-ammonia Rankine cycles	0.600
[95]	BFG, LNG	Gas turbine, LNG utilization, seawater desalination unit, modified Kalina cycle, and PEME	0.410
This study	LNG	LNG regasification, SMR, gas turbine, steam Rankine cycle, Kalina cycle, hot water boiler, and PEME	**Base: 0.353** **Opt.: 0.297**
			LCOE ($/kWh)
[95]	BFG, LNG	Gas turbine, LNG utilization, seawater desalination unit, modified Kalina cycle, and PEME	0.480
This study	LNG	LNG regasification, SMR, gas turbine, steam Rankine cycle, Kalina cycle, hot water boiler, and PEME	**Base: 0.352** **Opt.: 0.307**
			TUCP ($/GJ)
[28]	Biogas	Biogas steam reforming, purification, and MG system	16.23
[94]	Biomass, LNG	Hybrid biomass-LNG-based MG system combining a coffee husk combustor with LNG cold energy, electrolyzer, desalination, and organic-ammonia Rankine cycles	15.59
[95]	BFG, LNG	Gas turbine, LNG utilization, seawater desalination unit, modified Kalina cycle, and PEME	47.23
This study	LNG	LNG regasification, SMR, gas turbine, steam Rankine cycle, Kalina cycle, hot water boiler, and PEME	**Base: 12.79** **Opt.: 10.84**

efficiency (η_{MG}), the optimized configuration achieves 63.34%, exceeding comparable natural gas-centered systems (53.35–61%) and substantially outperforming biomass- and biogas-based configurations (29.90–31.51%). The exergy efficiency (ψ_{MG}) reaches 56.50% (optimized), which is significantly higher than previously reported values ranging from 14.38% to 43.12% for hybrid LNG, biomass, methanol, and blast furnace gas (BFG)-based systems. Environmentally, the optimized system reduces the ω_{CO_2} rate to 0.297 kg_{CO2}/kWh, compared to literature values of 0.410–0.600 kg_{CO2}/kWh. From an economic perspective, the system shows competitive performance with an optimized LCOE of 0.307 $/kWh, lower than the reported 0.4805 $/kWh, and an optimized TUCP of 10.84 $/GJ, which is markedly below the 15.59–47.23 $/GJ range in comparable studies. Therefore, these outcomes confirm the simultaneous thermo–enviro–economic superiority of the proposed configuration.

5. Conclusion

The present project presented a new thermodynamically integrated LNG-based quad-generation system designed for the concurrently production of electricity, cooling, heating, and hydrogen. By effectively cascading LNG cold energy recovery with steam methane reforming, a gas turbine, a steam Rankine cycle, a Kalina cycle, and a PEME, the system achieved a baseline energy efficiency of 55.29% and an exergy efficiency of 48.99%, alongside competitive specific CO_2 emissions of 0.3537 kg_{CO2}/kWh. To address the computational complexity of the integrated model, a surrogate-assisted multi-objective optimization framework—utilizing a Multi-Layer Perceptron model coupled with the Cuckoo Search algorithm—was successfully implemented. The optimization revealed distinct trade-offs between objectives, with the LINMAP-selected Scenario 2 offering a superior compromise, yielding an optimized exergy efficiency of 56.50%, a Profit of 31.01 M$, and a total unit cost of product of 10.84 $/GJ. Comprehensive sensitivity and uncertainty analyses identified LNG flow rate and GT-100 outlet pressure as the primary drivers of system performance, while benchmarking confirmed that the proposed configuration outperforms recent literature in energy utilization and exergo-economic-environmental viability.

Practical Implications: The proposed quad-generation framework provides a highly efficient pathway for decarbonizing hydrogen production while maximizing resource utilization through effective cold and thermal energy recovery. The high profitability and competitive LCOE values suggest that this system is technically and economically mature for deployment in industrial settings requiring multi-utility outputs.

Limitations and Future Directions: While this study provides a robust steady-state analysis, it relies on the simplification of LNG as pure methane, which may necessitate further refinement through multi-component fluid analysis to enhance precision for real-world feedstocks. Future research should prioritize dynamic modeling to evaluate system response to transient load fluctuations and renewable energy integration, as well as the implementation of advanced control strategies to maintain optimal operating zones under variable market and operational conditions.

CRediT authorship contribution statement

Yonghui Li: Project administration, Investigation, Funding acquisition, Formal analysis. **Ali Basem:** Formal analysis, Data curation. **Hyder H. Abed Balla:** Supervision, Investigation. **Mohamed Arbi Khlifi:** Writing – original draft, Formal analysis. **Haibo Zhang:** Supervision, Resources, Formal analysis. **Saleh Alhumaid:** Validation, Conceptualization. **Nasser Alsharif:** Validation, Data curation. **Sherzod Abdullaev:** Writing – review & editing, Writing – original draft. **Yasser Fouad:** Supervision, Methodology, Funding acquisition, Conceptualization. **Ibrahim Mahariq:** Writing – review & editing, Supervision, Formal analysis.

Declaration of competing interest

The authors declare that they have no known competing financial interests or personal relationships that could have appeared to influence the work reported in this paper.

Acknowledgement

Ongoing Research Funding program, (ORF-2026-698), King Saud University, Riyadh, Saudi Arabia. This work was financially supported by the Key Project of Philosophy and Social Sciences in Yunnan Province: “Research on Rule Coordination and Governance Innovation in China-Myanmar Cross-Border Data Flow (ZD202525)”; the National Social Science foundation project of China (23BJL088).

Appendix A. Supplementary data

Supplementary data to this article can be found online at https://doi.org/10.1016/j.fuel.2026.140372.

Data availability

The authors do not have permission to share data.

References

[1] Kalan AS, Khuyinrud MB, Jahangiri F, Ahmadi R, Mahboubi A, Lü X, et al. Thermodynamic analysis and performance enhancement of an integrated solar–geothermal polygeneration system using grey wolf optimization and LSTM-based forecasting with monte carlo uncertainty analysis: a case study on tenerife island. Appl Energy 2025;401:126640.
[2] Slimene MB, Basem A, Osman H, Soliman NF, Khlifi MA, Elkhaleefa AM, Safarova L, Jumanazarov D, Khudoynazarov E. A novel heat integration in a hybrid geothermal–biomass energy system for sustainable production of electricity, methanol, and desalinated water: exergoeconomic assessment and data-driven optimization. Process Saf Environ Prot 2025;108348.
[3] Zhao T, Ahmad SF, Agrawal MK, Ahmad AYAB, Ghfar AA, Valsalan P, et al. Design and thermo-enviro-economic analyses of a novel thermal design process for a CCHP-desalination application using LNG regasification integrated with a gas turbine power plant. Energy 2024;295:131003.
[4] Li M, Yang J, Mehrpooya M, Guo Z, He T. Off-grid green hydrogen production and liquefaction system driven by renewable energy and LNG cold energy: a comprehensive 4E analysis and optimization. Appl Energy 2025;392:125882.
[5] Ebrahimnejad M, Mehrpooya M, Bid-hendi GN. Introducing and performance evaluation of a novel multi-generation process for producing power, fresh water, oxygen and nitrogen integrated with liquefied natural gas regasification and carbon dioxide removal process. Appl Therm Eng 2024;248:123241.
[6] Machfudiyanto RA, Humang WP, Kamil I, Latief Y, Wahjuningsih N, Putra YYA. Enhancing small-scale LNG supply chains: risk mitigation strategies and frameworks for archipelagic distribution. Cleaner Logist Supply Chain 2025;16:100249.
[7] Yousef MS, Santana D. Thermo-economic assessment and optimization of an innovative tri-generation system using supercritical CO2 power system and LNG cold energy recovery. Energy Convers Manage: X 2024;21:100516.
[8] Zonfrilli M, Facchino M, Serinelli R, Chesti M, De Falco M, Capocelli M. Thermodynamic analysis of cold energy recovery from LNG regasification. J Clean Prod 2023;420:138443.
[9] Noor Akashah MH, Mohammad Rozali NE, Mahadzir S, Liew PY. Utilization of cold energy from LNG regasification process: a review of current trends. Processes 2023;11:517.
[10] Fioriti D, Baccioli A, Pasini G, Bischi A, Migliarini F, Poli D, et al. LNG regasification and electricity production for port energy communities: economic profitability and thermodynamic performance. Energy Convers Manag 2021;238:114128.
[11] Hsu C, Basem A, Le LT, Singh PK, Rusho MA, Abdullaeva B, et al. Evaluation of a novel environmentally friendly cascade combined cooling and power system integrated with LNG regasification and desalination unit. Therm Sci Eng Prog 2025;104113.
[12] Slimene MB, Basem A, Hasan MA, Le LT, Khlifi MA, Islam S, Atamuratova Z, Sabirov S, Mukhitdinov O, Mahariq I. Exergoeconomic analysis and optimization of a thermal–thermochemical system integrating biomass gasification and geothermal energy for power, methanol, and liquefied hydrogen. Appl Therm Eng 2025;129438.
[13] Liang Z, Liang Y, Luo X, Wang H, Wu W, Chen J, et al. Integration and optimization of methanol-reforming proton exchange membrane fuel cell system for distributed generation with combined cooling, heating and power. J Clean Prod 2023;411:137342.
[14] Boujelbene M, Basem A, Sawwan H, Samad S, Hamida MB, Amari A, Makharov K, Safarova L, Mahariq I. Multi-Objective optimization of a biogas-fueled multigeneration system with a supercritical CO2-based power and multi-level cooling cycle: a hybrid ANN-MOPSO approach. Fuel 2026;405:136687.
[15] Yang J-H, Yoon Y, Ryu M, An S-K, Shin J, Lee C-J. Integrated hydrogen liquefaction process with steam methane reforming by using liquefied natural gas cooling system. Appl Energy 2019;255:113840.
[16] Achomo MA, Kumar A, Peela NR, Muthukumar P. Hydrogen production from steam reforming of methanol: a comprehensive review on thermodynamics, catalysts, reactors, and kinetic studies. Int J Hydrogen Energy 2024;58:1640–72.
[17] Sornumpol R, Nimmanterdwong PP. Comprehensive energy exergy economic and environmental assessment of an integrated organic rankine cycle solid oxide fuel cell and absorption chiller system fueled by steam reformed natural gas. Proceedings of the International Petroleum Technology Conference. 2024.
[18] Tang X, Wu Y, Fang Z, Dong X, Du Z, Deng B, et al. Syntheses, catalytic performances and DFT investigations: a recent review of copper-based catalysts of methanol steam reforming for hydrogen production. Energy 2024;295:131091.
[19] Abbas AHM, Cheralathan KK, Porpatham E, Arumugam SK. Hydrogen generation using methanol steam reforming–catalysts, reactors, and thermo-chemical recuperation. Renew Sustain Energy Rev 2024;191:114147.
[20] Yan L, Jia Z, Liu Y, Geng C, He B. Thermodynamic and economic analyses of a novel cooling, heating and power tri-generation system with carbon capture. Atmosphere (Basel) 2024;15:836.
[21] Hu Y, Han C, Li W, Hu Q, Wu H, Li Q. Investigation of methanol steam reforming reformer heated by catalyst combustion for KW-scale fuel cell. Therm Sci Eng Prog 2023;45:102114.
[22] Su Z, Su Y, Majdi HS, Shawabkeh A, Abbas SZ, Eldin SM, et al. 4E analyses of a novel multi-generation system based on methanol-steam reforming integrated with scramjet multi cooling cycle and ammonia synthesis. Process Saf Environ Prot 2023;171:578–90.
[23] Chen Z, Yin B, Wei Z, Dong F. Coupling of high-temperature proton exchange membrane fuel cells with methanol steam reforming: modeling and simulation for an integrated coupled for power generation system. Energy Convers Manag 2024;301:118044.
[24] Abed AM, Shawabkeh A, Jhala R, Ramachandran T, Shankhyan A, Mann VS, et al. Exergoeconomic investigation of a multi-generation system based on gas turbine, carbon dioxide recondensation, multi effect desalination and methanol-steam reforming. Therm Sci Eng Prog 2025;58:103170.
[25] Dai Z, Yin X. Investigating the performance of a gas turbine system combined with steam methane reforming as a thermochemical recuperator in a power, cooling, freshwater, and hydrogen production multigeneration system. Energy 2024;311:133346.
[26] Soltanimehr S, Rahimpour MR, Shariati A. Development of a green process based on a novel tri-reforming reactor to produce syngas for methanol synthesis: process design, modeling and multi objective optimization. J Clean Prod 2023;418:138167.
[27] Zhong Z, Gao X, Zhu J, Zhao W, Li N, Araya SS, et al. Multi-objective optimization of a combined cooling, heating and power system integrated with reformed methanol high-temperature proton exchange membrane fuel cell. Energy Sources Part A 2025;47:3674–91.
[28] He J, Han N, Xia M, Sun T, Ghaebi H. Multi-objective optimization and exergoeconomic analysis of a multi-generation system based on biogas-steam reforming. Int J Hydrogen Energy 2023;48:21161–75.
[29] Abedinia O, Shakibi H, Shokri A, Sobhani B, Sobhani B, Yari M, et al. Optimization of a syngas-fueled SOFC-based multigeneration system: enhanced performance with biomass and gasification agent selection. Renew Sustain Energy Rev 2024;199:114460.
[30] Junjie J, Yongqi Z, Zhou X, AL-Bukhaiti K, Anping W, Cheng X, Ji X. Enhanced YOLO-IASE for robust safety inspection in complex substation environments. Signal Image Video Process 2025;19:686.
[31] Junjie J, Yongqi Z, Anping W, AL-Bukhaiti K, Huang J, Cheng X. Multi-target detection for safety monitoring in complex substation environments using YOLO-DySE. Signal Image Video Process 2025;19:804.
[32] Ansarinasab H, Mehrpooya M, Pouriman M. Advanced exergoeconomic evaluation of a new cryogenic helium recovery process from natural gas based on the flash separation–APCI modified process. Appl Therm Eng 2018;132:368–80.
[33] Lopez-Echeverry JS, Reif-Acherman S, Araujo-Lopez E. Peng-robinson equation of state: 40 years through cubics. Fluid Phase Equilib 2017;447:39–71.

[34] Ji L, Basem A, Balla HHA, Li Y, Alkhatib OJ, Ayadi M, et al. Thermo-economic decision-making and intelligent optimization of a sustainable biogas-driven system with integrated peak demand management. Biomass Bioenergy 2026;207:108785.
[35] Kong D, Tian X, Li G, Liu C, Niu X, Isaev SA, et al. Numerical study of particle deposition and heat transfer characteristics in an S-shaped miniature cooling channel of a gas turbine blade. Powder Technol 2026;468:121612. https://doi.org/10.1016/j.powtec.2025.121612.
[36] Shakibi H, Assareh E, Chitsaz A, Keykhah S, Behrang M, Golshanzadeh M, et al. Exergoeconomic and optimization study of a solar and wind-driven plant employing machine learning approaches; a case study of Las Vegas city. J Clean Prod 2023;385:135529.
[37] Bian Y, Pan J, Liu Y, Zhang F, Yang Y, Arima H. Performance analysis of a combined power and refrigeration cycle. Energy Convers Manag 2019;185:259–70.
[38] Azizi S, Shakibi H, Shokri A, Chitsaz A, Yari M. Multi-aspect analysis and RSM-based optimization of a novel dual-source electricity and cooling cogeneration system. Appl Energy 2023;332:120487.
[39] Chehade AMEH, Daher EA, Assaf JC, Riachi B, Hamd W. Simulation and optimization of hydrogen production by steam reforming of natural gas for refining and petrochemical demands in Lebanon. Int J Hydrogen Energy 2020;45:33235–47.
[40] Zhang X, Zeng R, Du T, He Y, Tian H, Mu K, et al. Conventional and energy level based exergoeconomic analysis of biomass and natural gas fired polygeneration system integrated with ground source heat pump and PEM electrolyzer. Energy Convers Manag 2019;195:313–27.
[41] Habibollahzade A, Gholamian E, Ahmadi P, Behzadi A. Multi-criteria optimization of an integrated energy system with thermoelectric generator, parabolic trough solar collector and electrolysis for hydrogen production. Int J Hydrogen Energy 2018;43:14140–57.
[42] Ni M, Leung MKH, Leung DYC. Energy and Exergy analysis of hydrogen production by a proton exchange membrane (PEM) electrolyzer plant. Energy Convers Manag 2008;49:2748–56.
[43] Tijani AS, Rahim AHA. Numerical modeling the effect of operating variables on faraday efficiency in PEM electrolyzer. Procedia Technol 2016;26:419–27.
[44] Tijani AS, Kamarudin NAB, Mazlan FAB. Investigation of the effect of charge transfer coefficient (CTC) on the operating voltage of polymer electrolyte membrane (PEM) electrolyzer. Int J Hydrogen Energy 2018;43:9119–32.
[45] Nieminen J, Dincer I, Naterer G. Comparative performance analysis of PEM and solid oxide steam electrolysers. Int J Hydrogen Energy 2010;35:10842–50.
[46] El-Emam RS, Dincer I. Development and assessment of a novel solar heliostat-based multigeneration system. Int J Hydrogen Energy 2018;43:2610–20.
[47] Mehrenjani JR, Gharehghani A, Ahmadi S, Powell KM. Dynamic simulation of a triple-mode multi-generation system assisted by heat recovery and solar energy storage modules: techno-economic optimization using machine learning approaches. Appl Energy 2023;348:121592.
[48] Mokarram NH, Mosaffa AH. A comparative study and optimization of enhanced integrated geothermal flash and kalina cycles: a thermoeconomic assessment. Energy 2018;162:111–25.
[49] Ioroi T, Yasuda K, Siroma Z, Fujiwara N, Miyazaki Y. Thin film electrocatalyst layer for unitized regenerative polymer electrolyte fuel cells. J Power Sources 2002;112:583–7.
[50] Hou S, Zhou Y, Yu L, Zhang F, Cao S, Wu Y. Optimization of a novel cogeneration system including a gas turbine, a supercritical CO2 recompression cycle, a steam power cycle and an organic rankine cycle. Energy Convers Manag 2018;172:457–71.
[51] Habibollahzade A, Rosen MA. Syngas-fueled solid oxide fuel cell functionality improvement through appropriate feedstock selection and multi-criteria optimization using air/O2-enriched-air gasification agents. Appl Energy 2021;286:116497.
[52] Zemin D, Yueming L, Zhicheng Y, Youhong Y, Yongbao L. Coordinated control strategy of engine-grid-load-storage for shipboard micro gas turbine DC power generation system: a review. J Energy Storage 2025;134:118205.
[53] Wen D, Wei X, Bruneau A, Maroonian A, Maréchal F. Techno-economic analysis of ammonia to hydrogen and power pathways considering the emerging hydrogen purification and fuel cell technologies. Appl Energy 2025;390:125871.
[54] Feili M, Nourani P, Haghghi MA, Bahman AM. Machine learning optimization of integrating an advanced thermal-electrochemical plant with an oxy-biogas fuel plant employing a CO2 capture process. Energy Convers Manag 2025;335:119871.
[55] Chen L, Xiao K, Hu F, Li Y. Performance evaluation and optimization design of integrated energy system based on thermodynamic, exergoeconomic, and exergoenvironmental analyses. Appl Energy 2022;326:119987.
[56] Wang X, Ye L, Li W, Zheng T, Liang X, Liu C. Film cooling effectiveness in the presence of internal hole random roughness: a comprehensive analysis. Int Commun Heat Mass Transfer 2025;165:108990.
[57] Ye L, She H, Sun C, Wang X, Liu C, Shi C. A mass-flux-vector-based design for self-angled slot arrangements enhancing leading edge showerhead cooling. Int Commun Heat Mass Transfer 2026;172:110305.
[58] Li S, Zhu L, He Y, Fan J, Lv L. Thermodynamic evaluation of CCHP system based on biomass gasification by exploring the feasibility of using CO2 as gasification agent. Sustainable Energy Technol Assess 2020;42:100867.
[59] Wang J, Zhai ZJ, Jing Y, Zhang C. Particle swarm optimization for redundant building cooling heating and power system. Appl Energy 2010;87:3668–79.
[60] Li H, Zhang J, Zhou J, Zang J, Shi G, Cai X. An active-soft-switching DC transformer with auxiliary converter for DC offshore wind turbine. IEEE Trans Ind Electron 2026.
[61] Pan C, Hu X, Goyal V, Alsenani TR, Alkhalaf S, Alkhalifah T, et al. An innovative process design of seawater desalination toward hydrogen liquefaction applied to a ship's engine: an economic analysis and intelligent data-driven learning study/optimization. Desalination 2024;571:117105.
[62] Haorong L, Huixin Z, Xinlong W, Xiaojuan N, Wenpeng H, Haoran L. Enhanced vapor condensation in bidirectional solar stills using copper foam with multiple nucleation sites. Sci China Technol Sci.
[63] Sinha AA, Choudhary T, Ansari MZ. Estimation of exergy-based sustainability index and performance evaluation of a novel intercooled hybrid gas turbine system. Int J Hydrogen Energy 2023;48:8629–44.
[64] Yang K, He Y, Du N, Yan P, Zhu N, Chen Y, et al. Exergy, exergoeconomic, and exergoenvironmental analyses of novel solar-and biomass-driven trigeneration system integrated with organic rankine cycle. Energy 2024;301:131605.
[65] He D, Li H, Gao R, Li Y, Fan L, Long X, et al. A fission response function based low-cost adaptive reactor physics code for high-fidelity simulation. Nucl Sci Eng 2025:1–19.
[66] Wang Y, Mu Q, Bai Z, Elmasry Y, Balla HHA, Alkhayyat A, et al. Life cycle assessment, techno-economic and environmental analysis of an innovative integration air power cycle with LNG cold energy utilization in a biomass-fueled multi-generation plant: soft computing technique and multi-objective optimization approaches. Energy 2025;139182.
[67] Ooi JB, Kau CC, Manoharan DN, Wang X, Tran M-V, Hung YM. Effects of multi-walled carbon nanotubes on the combustion, performance, and emission characteristics of a single-cylinder diesel engine fueled with palm-oil biodiesel-diesel blend. Energy 2023;281:128350.
[68] Iordan C, Lausselet C, Cherubini F. Life-cycle assessment of a biogas power plant with application of different climate metrics and inclusion of near-term climate forcers. J Environ Manage 2016;184:517–27.
[69] Jo S-J, Kang T-H, Shin B-J, Mun J-H, Devkota S, Cha J-Y, et al. Internal carbon loop strategy for methanol production from natural gas: multi-objective optimization and process evaluation. J Clean Prod 2023;418:138140.
[70] Fang Z, Shang L, Pan Z, Yao X, Ma G, Zhang Z. Exergoeconomic analysis and optimization of a combined cooling, heating and power system based on organic rankine and kalina cycles using liquified natural gas cold energy. Energy Convers Manag 2021;238:114148.
[71] Behzadi A, Duwig C, Ploskic A, Holmberg S, Sadrizadeh S. Application to novel smart techniques for decarbonization of commercial building heating and cooling through optimal energy management. Appl Energy 2024;376:124224.
[72] Devkota S, Cha J-Y, Shin B-J, Mun J-H, Yoon HC, Mazari SA, et al. Techno-economic and environmental assessment of hydrogen production through ammonia decomposition. Appl Energy 2024;358:122605.
[73] Feili M, Ghaebi H, Haghghi MA. Data-driven optimization of an innovative environmentally friendly power-methanol co-production system utilizing biogas-driven S-graz cycle, biogas steam reforming, and CO2 capture-hydrogenation process. Renew Energy 2025;123835.
[74] Abdolalipouradl M, Khalilarya S, Jafarmadar S. Exergoeconomic analysis of a novel integrated transcritical CO2 and kalina 11 cycles from sabalan geothermal power plant. Energy Convers Manag 2019;195:420–35.
[75] Asgari N, Saray RK, Mirmasoumi S. Seasonal exergoeconomic assessment and optimization of a dual-fuel trigeneration system of power, cooling, heating, and domestic hot water, proposed for Tabriz Iran. Renew Energy 2023;206:192–213.
[76] Sohrabi A, Asgari N, Imran M, Shahzad MW. Comparative energy, exergy, economic, and environmental (4E) analysis and optimization of two high-temperature kalina cycles integrated with thermoelectric generators for waste heat recovery from a diesel engine. Energy Convers Manag 2023;291:117320.
[77] Karim SHT, Tofiq TA, Shariati M, Rad HN, Ghasemi A. 4E analyses and multi-objective optimization of a solar-based combined cooling, heating, and power system for residential applications. Energy Rep 2021;7:1780–97.
[78] Lin F, Wang J, Nutakki TUK, Ayadi M, Ahmad SF, Muhammad T, et al. Proposal, process development, and multi-aspect investigation of a novel environmentally friendly multigeneration process in arrangement with a sea water desalination unit. J Environ Chem Eng 2023;11:111392.
[79] Liu S, Hai T, Chauhan BS, Asadollahzadeh M, Oreijah M, Guedri K, et al. Multi-aspect study of an innovative glycerol-fed polygeneration model involving combined power cycles, chilled water unit, desalination, and methanol synthesis. Desalination 2023;564:116795.
[80] Zhu P, Wu Z, Guo L, Yao J, Dai M, Ren J, et al. Achieving high-efficiency conversion and poly-generation of cooling, heating, and power based on biomass-fueled SOFC hybrid system: performance assessment and multi-objective optimization. Energy Convers Manag 2021;240:114245.
[81] Cao Y, Dhahad HA, Togun H, Hussen HM, Anqi AE, Farouk N, et al. Thermodynamic and economic assessments and multi-criteria optimization of a novel poly-generation plant using geothermal energy and multi heat recovery technique. Int J Hydrogen Energy 2021;46:27851–73.
[82] Sadat SMS, Ghaebi H, Lavasani AM. 4E analyses of an innovative polygeneration system based on SOFC. Renew Energy 2020;156:986–1007.
[83] Faramarzi S, Nainiyan SMM, Mafi M, Ghasemiasl R. A novel hydrogen liquefaction process based on LNG cold energy and mixed refrigerant cycle. Int J Refrig 2021;131:263–74.
[84] Zhang M, Timoshin A, Al-Ammar EA, Sillanpaa M, Zhang G. Power, cooling, freshwater, and hydrogen production system from a new integrated system working with the zeotropic mixture using a flash-binary geothermal system. Energy 2023;263:125959.
[85] Ata S. Comprehensive evaluation of a gas turbine-based multi-generation system for power, heating, cooling, freshwater, hydrogen and ammonia: 4E assessment and multi-objective optimization with RSM desirability approach. Renew Energy 2025;246:122900.

[86] Haghghi MA, Jafarmadar S, Kaveh M. Modified-route chemical-to-power conversion via biomass gasification–HSOFC with waste-to-power/freshwater integration: 4E analysis for biomass selection and LS-boosting-based optimization. Int J Hydrogen Energy 2026;245:155717.
[87] Kansha Y, Abbas A, Manaf NA. Unlocking the techno-economic potential of biomass gasification for power generation: comparative analysis across diverse plant capacities. Waste Manag 2024;189:219–29.
[88] Ooi JB, Chan XL, Jaliliantabar F, Tan BT, Wang X, Song CP, et al. Experimental study of quaternary blends with diesel/palm-oil biodiesel/ethanol/diethyl ether for optimum performance and emissions in a light-duty diesel engine using response surface methodology. Energy 2024;301:131782.
[89] Zhang B, Xue Y, Zhang Y, Su K. A self-calibrating digital twin for space thermionic nuclear reactors under fault conditions. Reliab Eng Syst Saf 2026;268:111995. https://doi.org/10.1016/j.ress.2025.111995.
[90] Wan A, Xiong Z, Khalil A-B, Yin R, Yuan J, Cheng X, et al. An integrated TCN-ECA-BiLSTM and TD3 framework for high-accuracy forecasting and optimal load allocation in combined heat and power systems. Energy 2026;140670.
[91] Vo N, Tang H, Lee J. A multi-objective grey wolf–cuckoo search algorithm applied to spatial truss design optimization. Appl Soft Comput 2024;155:111435.
[92] Salari A, Shakibi H, Soltani S, Kazemian A, Ma T. Optimization assessment and performance analysis of an ingenious hybrid parabolic trough collector: a machine learning approach. Appl Energy 2024;353:122062.
[93] Zhang Z, Delcroix B, Rezazgui O, Mangin P. Simulation and techno-economic assessment of bio-methanol production from pine biomass, biochar and pyrolysis oil. Sustainable Energy Technol Assess 2021;44:101002.
[94] Alamri S, Sadeq AM, Agrawal MK, Chauhdary ST, Ahmed MA, Ayadi M, et al. Ben hybrid biomass-LNG powered multigeneration multi-effect desalination system for sustainable freshwater, energy and hydrogen production: design and optimization using 4E analysis and machine learning-based evaluation. Desalination 2025; 119785.
[95] Ayadi M, Alamri S, Becheikh N, Ghachem K, Kolsi L, Chauhdary ST, et al. Data-driven multi-objective optimization of a novel waste-fueled polygeneration system for simultaneous production of hydrogen, freshwater, hot water, chilled water, cooling power, and electricity. Appl Therm Eng 2026;130553.